UNIVERSITE DE NEUCHATEL INSTITUT DE PHYSIQUE
Groupe de physique corpusculaire Professeur Jean – Luc VUILLEUMIER

STUDY OF NUCLEAR EFFECTS IN CALCIUM, CARBON AND LITHIUM WITH A 90 GeV MUON BEAM

THÈSE

présentée à la Faculté des Sciences

de l'Université de Neuchâtel

pour l'obtention du grade de docteur ès Sciences,

mention physique

par

Carlo BROGGINI

physicien diplomé de l'Université de Milano

24 février 1989

IMPRIMATUR POUR LA THÈSE

Study of Nuclear Effects in Calcium, Carbon and Lithium with a 90 GeV/c Muon Beam

de Monsieur Carlo Broggini

UNIVERSITÉ DE NEUCHATEL

FACULTÉ DES SCIENCES

La Faculté des sciences de l'Université de Neuchâtel,
sur le rapport des membres du jury,

Messieurs J.-L. Vuilleumier, L.D. Fluri,
J.-F. Germond, R. Voss (Genève) et
D. von Harrach (Heidelberg)

autorise l'impression de la présente thèse.

Neuchâtel, le 6 mars 1989

Le doyen:

F. Persoz

Table of contents

Acknowledgements iii

INTRODUCTION iv

Chapter 1: THE DEEP INELASTIC SCATTERING 1

Chapter 2: THE EMC EFFECT 10

2.1 The low x region 12
2.2 The EMC effect in the region x > 0.1 14

Chapter 3: THE BEAM AND THE DETECTOR 18

3.1 The beam 18
3.1.1 Front end 18
3.1.2 Decay channel 20
3.1.3 Hadron absorber 20
3.1.4 Back end 20
3.1.5 Flux 21
3.1.6 Dispersion 21
3.1.7 Halo 21
3.2 The detector 23
3.2.1 General overview 23
3.2.2 Hodoscopes in the beam 23
3.2.3 Beam Momentum Station 25
3.2.4 Beam Hodoscopes 26
3.2.5 H_5 26

3.2.6 Veto 26
3.2.7 The forward spectrometer magnet (FSM) 27
3.2.8 Trigger hodoscopes 28
3.2.9 The calorimeter H_2 29
3.2.10 Proportional and drift chambers 31
3.2.11 P_0s 32
3.2.12 PV_1 and PV_2 32
3.2.13 P_{123} 32
3.2.14 P_{45} 33
3.2.15 Drift chambers 33
3.2.16 The target 33

Chapter 4: TRIGGERS AND DATA ACQUISITION 38

4.1 The triggers 38
4.1.1 T_1 38
4.1.2 T_2 39
4.1.3 T_5 : the beam trigger 41
4.1.4 T_6 : the alignment trigger 41
4.1.5 T_7: the near halo trigger 41
4.1.6 T_8 : the far halo trigger 41
4.1.7 T_9 42
4.1.8 T_{11} : the halo trigger 42
4.1.9 The normalization triggers T_{34} and T_{10} 42
4.2 The data acquisition 44

Chapter 5: THE SOFTWARE PRODUCTION CHAIN 45

5.1 Phoenix 46
5.2 Geometry 48
5.3 Snomux 49
5.4 Snomin 49
5.5 The Monte Carlo 50

Chapter 6: DATA ANALYSIS **52**

6.1 The radiative corrections 52
6.2 The geometrical method 55
6.3 The target thickness 57
6.4 The cuts on the data 58
6.5 The systematic errors 61
6.6 The results 62
6.7 The Q^2 dependence of r 68
6.8 T_2 analysis 69
6.9 The A dependence of r 72
6.10 The momentum sum rule 77

Chapter 7: THE HADRON CUT AND THE LOW X REGION **79**

7.1 The hadron cut 79
7.2 Electron hadron discrimination 79
7.3 Possible bias 81
7.4 Events selection and results 84

CONCLUSIONS **88**

APPENDIX **90**

Bibliography **91**

List of figures

1.1 Analogies between α scattering and deep inelastic 1

1.2 The lowest order Feynman diagram for deep inelastic scattering 2

1.3 BCDMS, EMC and SLAC results for F_2 proton
.... 7

1.4 The ratio of the EMC to the BCDMS measurement of F_2 proton. 8

1.5 Values of F_2 neutron measured by EMC. 9

2.1 The ratio 11

2.2 A dependence of the EMC effect 12

3.1 The SPS Site at CERN 19

3.2 The Beam Layout 22

3.3 Experimental Setup 24

3.4 Beam Momentum Station 25

3.5 The veto counters 27

3.6 Trigger hodoscopes beam holes 29

3.7 The calorimeter H_2 30

3.8 The drift cell structure 34

3.9 The complementary target setup 36

4.1 T_1 logic 39

4.2 T_2 logic 40

5.1 The NMC software production chain 47

6.1 diagrams which contribute to the measured cross section. 53

6.2 size of the radiative corrections on T_1 65

6.3 The ratio Ca/Li 65

6.4 The ratio C/Li 66

6.5 The ratio Ca/C 66

6.6 The ratio Ca/Li from the upstream and the downstream targets 67

6.7 The ratio C/Li from the upstream and the downstream targets 67

6.8 The ratio Ca/C from the upstream and the downstream targets 68

6.9 $dr/d\ln Q^2$ as function of x for Ca/Li 69

6.10 $dr/d\ln Q^2$ as function of x for C/Li 70

6.11 $dr/d\ln Q^2$ as function of x for Ca/C 70

6.12 the ratio Ca/Li 73

6.13 the ratio C/Li 73

6.14 the ratio Ca/C 74

6.15 size of the radiative corrections on T_2 74

6.16 the ratio Ca/Li from $T_1 + T_2$ 75

6.17 the ratio C/Li from $T_1 + T_2$ 75

6.18 the ratio Ca/C from $T_1 + T_2$ 76

6.19 the parameter α 78

6.20 the parameter α from the data 78

7.1 emagf distribution 80

7.2 the invariant mass distribution of the pions pairs from Lithium. 82

7.3 the hadron multiplicity 83

7.4 the ratio Ca/Li, the errors shown are the total errors, ... 86

7.5 the ratio C/Li 86

7.6 the ratio Ca/C 87

1. the ratio Ca/C 89

2. the ratios Fe/N and Cu/C 89

List of tables

3.1 Main parameters of the chambers 35

3.2 The thickness of the targets (in gr×cm^{-2}) 37

5.1 Surviving T_1, T_2 and T_{10} in the 90 GeV Ca/C/Li data 50

6.1 the thickness increase and the used thickness (in gr/cm^2) 58

6.2 the number of events after the cuts 59

6.3 the mean Q^2 (GeV/c^2)^2 and ν (GeV) 60

6.4 the ratio Ca/Li 63

6.5 the ratio C/Li 63

6.6 the ratio Ca/C 64

6.7 the parameters of the fit to dr/dlnQ^2 69

6.8 the number of events after the cuts 71

6.9 the mean Q^2 (GeV/c^2)^2 and ν (GeV) 71

6.10 the parameters of the fit to the ratios 72

7.1 the number of events after the cuts 83

7.2 the mean Q^2 (GeV/c^2)^2 and ν (GeV) 84

Acknowledgements

I wish to thank Prof. Jean – Luc Vuilleumier, who gave me the opportunity to undertake this research, and Louis Fluri for his constant care and advice.

The data analyzed in the thesis are the synthesis of the efforts of a large number of people: I thank all them. In particular I would like to thank Jacques Beaufays, Dietrich von Harrach, Fritz Klein and Yoshi Mizuno for the frequent, long and always enlightening discussions.

I acknowledge the financial support of the FNSRS.

INTRODUCTION

The parton model describes the hadrons as "atoms" or "molecules" of quarks, which are experimentally seen by a high resolution probe as pointlike constituents inside the nucleon. Their behaviour in the nucleon was supposed to be independent on the nuclear environment. In 1983 the European Muon Collaboration (EMC) presented results which disproved this assumption. Such a discovery, known as the EMC effect, triggered a great deal of research work; in particular a collaboration of about 60 physicists, the New Muon Collaboration (NMC), was formed for a detailed study of the effect with the muon beam line of CERN and with an upgraded version of the EMC spectrometer. In this thesis I will analyze the data taken by the NMC during two weeks in 1986 with a 90 GeV beam on Calcium, Carbon and Lithium targets arranged in a particular setup to minimize the systematic error. The aim of this data is to study the low x region above 0.0125 with a small statistical error. A different method used to remove the radiative events allows us to go further down to $x=0.005$. The covered Q^2 range is between 0.55 (GeV/c^2)^2 and 14.35 (GeV/c^2)^2.

Results are presented on the EMC effect in Ca/Li, C/Li and Ca/C, on its Q^2 and A dependence and on the momentum sum rule.

The data analyzed in this thesis will be used in future to investigate the A dependence of $R=\frac{\sigma_l}{\sigma_t}$ together with the 200 GeV/c data taken with the same target setup.

The presentation is organized in the following way: the deep inelastic scattering and the models of the EMC effect are described in the first two chapters, whereas the muon beam line and the experimental setup are the subject of the third chapter. The different triggers, the data acquisition and the data processing are treated in the fourth and in the fifth chapters. Finally the details of the analysis and the results are discussed in the last two chapters.

Chapter 1

THE DEEP INELASTIC SCATTERING

The quark description of hadrons was established in high energy electron – nucleon scattering. In this reaction the scattering cross section on a nucleon was found to be large even at high momentum transferred. As in the Rutherford experiment this is the signature of pointlike scattering centers inside the target [Figure 1.1]

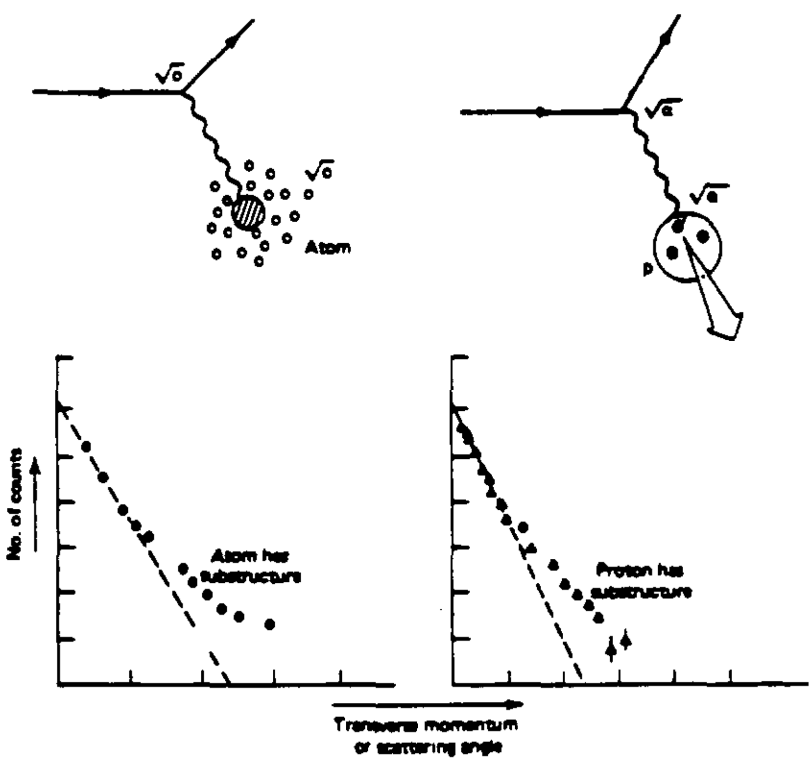

Figure 1.1: Analogies between α scattering and deep inelastic scattering experiments

When the transferred momentum is large, the elastic cross section vanishes and the probability of breaking the nucleon becomes high : this is the inelastic region.

In this experiment we are interested in the measurement of the inclusive cross section for the reaction $\mu + N \to \mu + X$ i.e., the cross section summed over all the possible hadronic final states. If we assume that the one photon exchange process dominates [Figure 1.2], then the cross section can be written as the product of a leptonic vertex tensor, well described by QED and a hadronic vertex tensor [1].

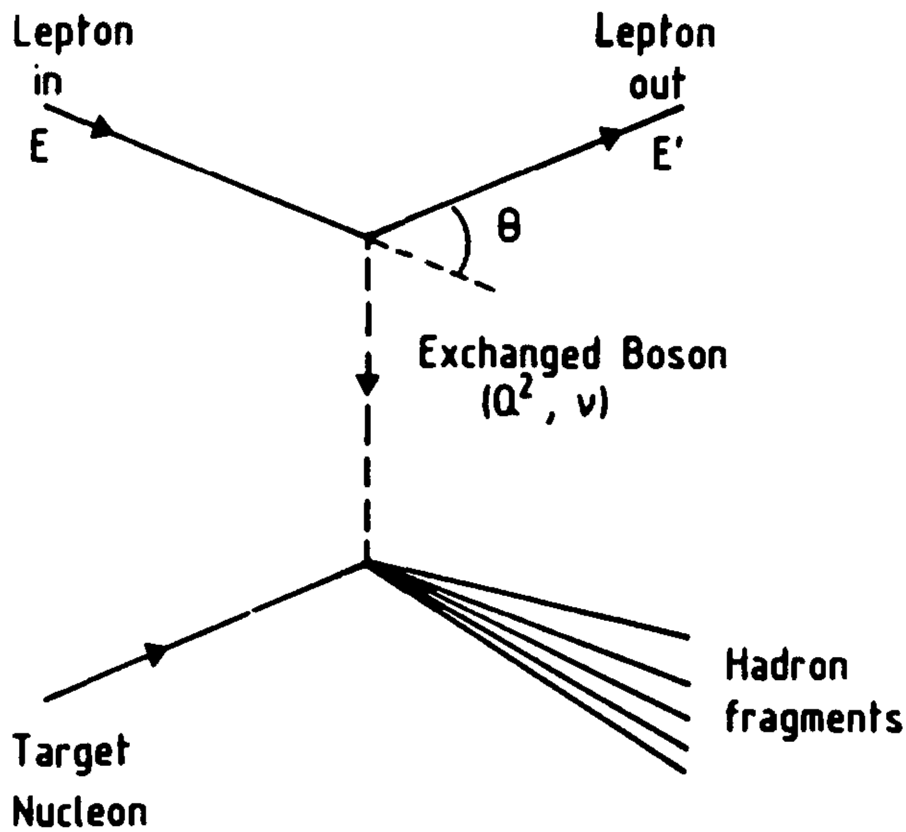

Figure 1.2: The lowest order Feynman diagram for deep inelastic scattering

Because of Lorentz invariance, electromagnetic current and parity conservation the cross section has the same structure as in elastic scattering but now the two form factors, which depend only on one variable, are replaced by two structure functions which depend on two variables. Let's define the variables in the following way : $\mathbf{k}, \mathbf{k}'$, $\mathbf{p}$ and $\mathbf{q}$ are the four-momenta in the laboratory system of the incident and scattered muon, of the target nucleon and of the virtual photon,respectively

$$\mathbf{k} = (E, \vec{k})$$

$$\mathbf{k}' = (E', \vec{k}')$$

$$\mathbf{p} = (M, \vec{0})$$

$$\mathbf{q} = \mathbf{k} - \mathbf{k}'$$

For convenience I will also use :

$$Q^2 = -q^2 \approx 4EE'\sin^2\frac{\theta}{2}$$

the positive invariant mass squared of the virtual photon,

$$\nu = E - E'$$

the transferred energy,

$$x = \frac{Q^2}{2M\nu}$$

$$y = \frac{\nu}{E}$$

the so called inelasticity and

$$W^2 = (p+q)^2$$

the invariant mass squared of the hadronic system. If the scattering is elastic than W is the proton mass and Q^2 is enough to describe the process, if it is inelastic W^2 is no more a constant and the cross section can be written as

$$\frac{\partial^2\sigma}{\partial\Omega\partial E'} = \sigma_M\left[W_2(\nu,Q^2) + 2W_1(\nu,Q^2)\tan^2\frac{\theta}{2}\right]$$

where σ_M is the Mott cross section. We expect the inelastic scattering to be a complicated process and the structure functions to reflect this. What is surprisingly found is that for $Q^2 \geq 1\ (GeV/c^2)^2$ the structure functions depend almost only on the ratio of Q^2 over ν, as predicted by Bjorken for $Q^2 \rightarrow \infty$ and $\nu \rightarrow \infty$ while their ratio stays finite. This was explained by Feynman in terms of elastic scattering off pointlike partons inside the nucleon, with the cross section of the deep inelastic scattering simply given by the incoherent sum of the elastic cross sections on the partons. Then x can be interpreted as the fraction of the nucleon momentum carried by the struck parton, in the nucleon infinite momentum frame where the nucleus is highly relativistic. The partons are most naturally identified with the quarks, previously introduced as the basis of the fundamental representation of SU(3) to classify the hadrons. In this simple model the structure functions scale in this way:

$$MW_1(\nu,Q^2)\to F_1(x)$$

$$\nu W_2(\nu,Q^2)\to F_2(x)=\sum_{i=1}^{n} x e_i^2[q_i(x)+\bar{q}_i(x)]$$

where n is the the number of quark flavours, e_i is the electric charge of the quark with flavour i, $q_i(x)$ is the probability for the quark i to carry a fraction x of the nucleon momentum . F_1 is related to F_2 through the ratio between the longitudinal and transversal photon cross sections :

$$R=\frac{\sigma_l}{\sigma_t}=\frac{[(1+\frac{4M^2x^2}{Q^2})F_2-2xF_1]}{2xF_1}$$

For spin 1/2 partons, $F_2(x)=2xF_1(x)$, a relation known as the Callan − Gross relation. For spin 0 partons $R\to\infty$.

The integral of F_2 gives the fraction of the nucleon momentum, weighted by the squared charges, carried by quarks and anti − quarks and it is measured to be $\sim\frac{1}{2}$. The missing fraction has thus to be carried by objects which cannot be seen by electromagnetic probes. These objects are identified with the gluons, that is the eight gauge bosons introduced to make local the SU (3) quark colour symetry and which mediate the strong force. The presence of the gluons has an observable consequence on the structure functions : the scaling, that is the Q^2 independence, is only approximately true because of gluon radiation by the quarks and because of quarks pair production by the gluons. The breakdown of the scaling is described by Perturbative QCD , which relates the probability densities of the quarks $q_i(x,Q^2)$ at any Q^2 with the gluon and quark densities at a certain point Q_0^2. The Q^2 evolution of the structure function is ruled by the Altarelli – Parisi equation [2] :

$$\frac{\partial q_i(x,Q^2)}{\partial \ln(Q^2)} = \frac{\alpha_s}{2\pi} \int_{z=x}^{1} [q_i(z,Q^2) P_{qq}(\frac{x}{z}) + g(z,Q^2) P_{qg}(\frac{x}{z})] dz$$

where $g(z,Q^2)$ is the probability of a gluon to carry a fraction z of the nucleon momentum and α_s is the strong coupling constant. This equation tells that a quark with a momentum fraction x could have come from a parent quark with a larger momentum fraction z which has radiated a gluon or could be the result of a $q\bar{q}$ pair creation by a parent gluon with momentum fraction z. $\alpha_s P_{qq}$ and $\alpha_s P_{qg}$ are the probabilities for the two different processes. As a consequence the number of partons and gluons which share the nucleon momentum increases with Q^2, therefore the probability of finding a parton increases at low x and decreases at high x .

Experimentally the different measurements of F_2 in Hydrogen and Deuterium available today are inconsistent and incomplete. To settle these problems is one of the two main goals of the NMC experiment [3] ; the other one,which will be treated in the next chapter, is the study of the influence of the nuclear environment on F_2.

High statistics measurements of F_2 (proton) have been made at SLAC [4] up to Q^2 = 20 (GeV/c²) ² , and at CERN by EMC [5] and BCDMS [6] up to 200 (GeV/c²)². Between the SLAC and CERN data there is almost no overlap. The scaling violation in BCDMS, SLAC [Figure 1.3] and EMC data are similar [Figure], but there is a strong disagreement in F_2 in function of x [Figure 1.4] . The discrepancy is three times that allowed by the quoted systematic errors and can be produced only by a serious error made in one of the measurements ; the neutrino experiments on hydrogen targets, because of the low statistic, are not able to resolve the disagreeement. In such a situation, the agreement in $\frac{\partial F_2(x,Q^2)}{\partial \ln Q^2}$, from which α_s can be extracted, " seems rather fortuitous and any comparison with PQCD almost without value " [7].

The function F_2^n is extracted from the difference between the measured deuteron and proton structure functions, with small corrections due to Fermi motion. The Q^2 dependence of F^n_2 seems to indicate a very small scale breaking [Figure 1.5], but there is an incomplete coverage of the Q^2 range [Figure 1.5].

With a high luminosity and simultaneous measurement on hydrogen and deuterium the NMC experiment will give F_2 of proton and neutron with small error. It will then be possible to make an accurate analysis of $F^p_2 - F^n_2$ and $\frac{F^p_2}{F^n_2}$.

The difference $F^p_2 - F^n_2$ is a purely flavour non singlet function independent of the shape of the gluon distribution, if the sea distribution is the same in proton and neutron. The PQCD fit to $F^p_2 - F^n_2$ will give a determination of α_s independent of the heavy quarks thresholds and also free from some higher−twist contributions. The aim of NMC is to obtain this difference with a statistical error of about 5% in most (Q^2 , x) bins, starting from x=0.005 in order to accurately check the Gottfried sum rule

$$\int_{x=0}^{1} \frac{(F^p_2 - F^n_2)}{x} dx = \frac{1}{3}$$

whose violation could indicate that the assumption of a flavour symmetric sea is wrong.

The ratio $\frac{F^n_2}{F^p_2}$. gives the relative proportion of u and d quarks in the nucleon. An accurate knowledge of this ratio is important to check the diquark model [11] and, in the context of $p\bar{p}$ experiments, to give a limit on the number of light neutrino families and on the mass of the top quark [12].

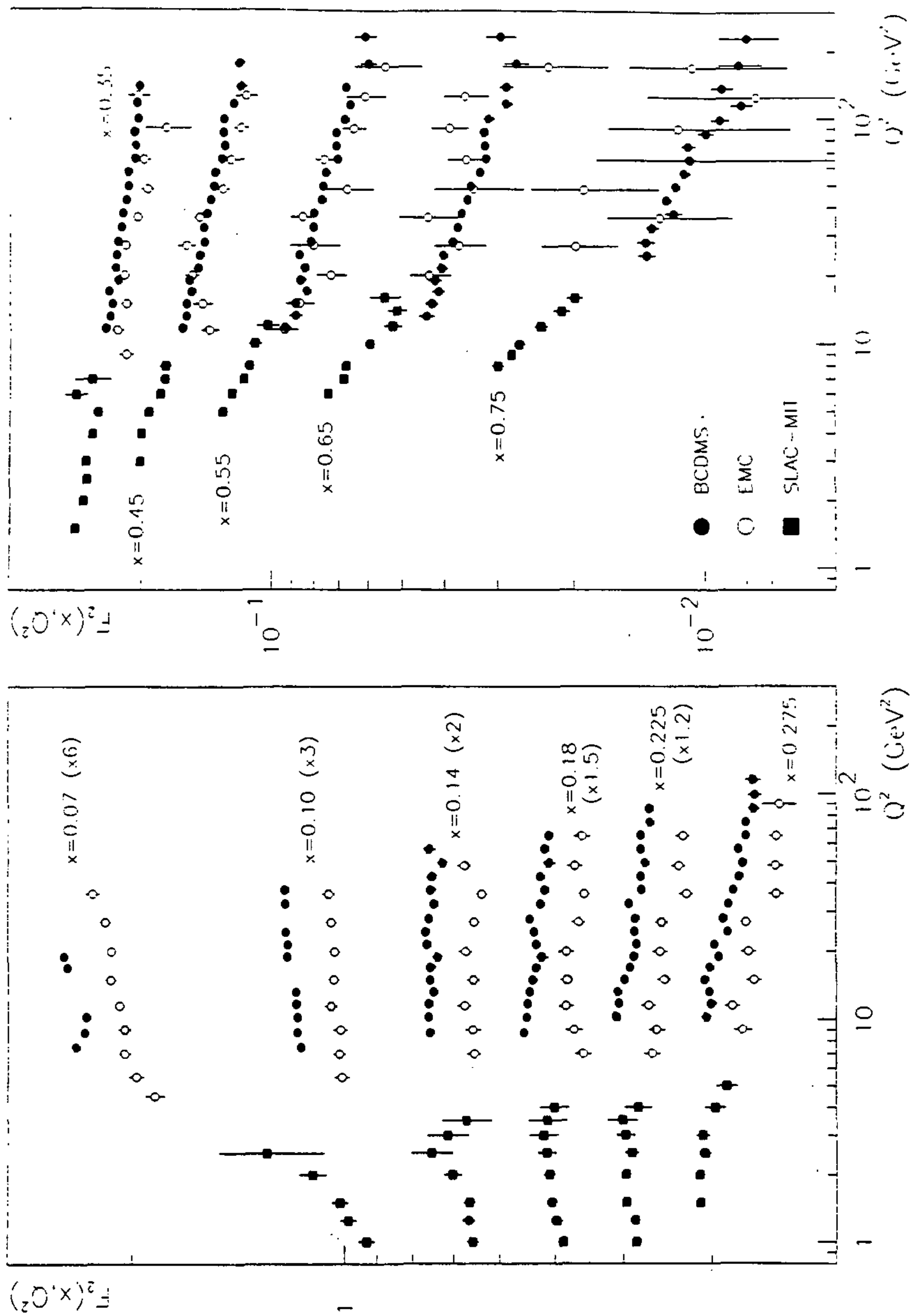

Figure 1.3: BCDMS, EMC and SLAC results for F_2 proton as a function of Q^2 in different bins of x.

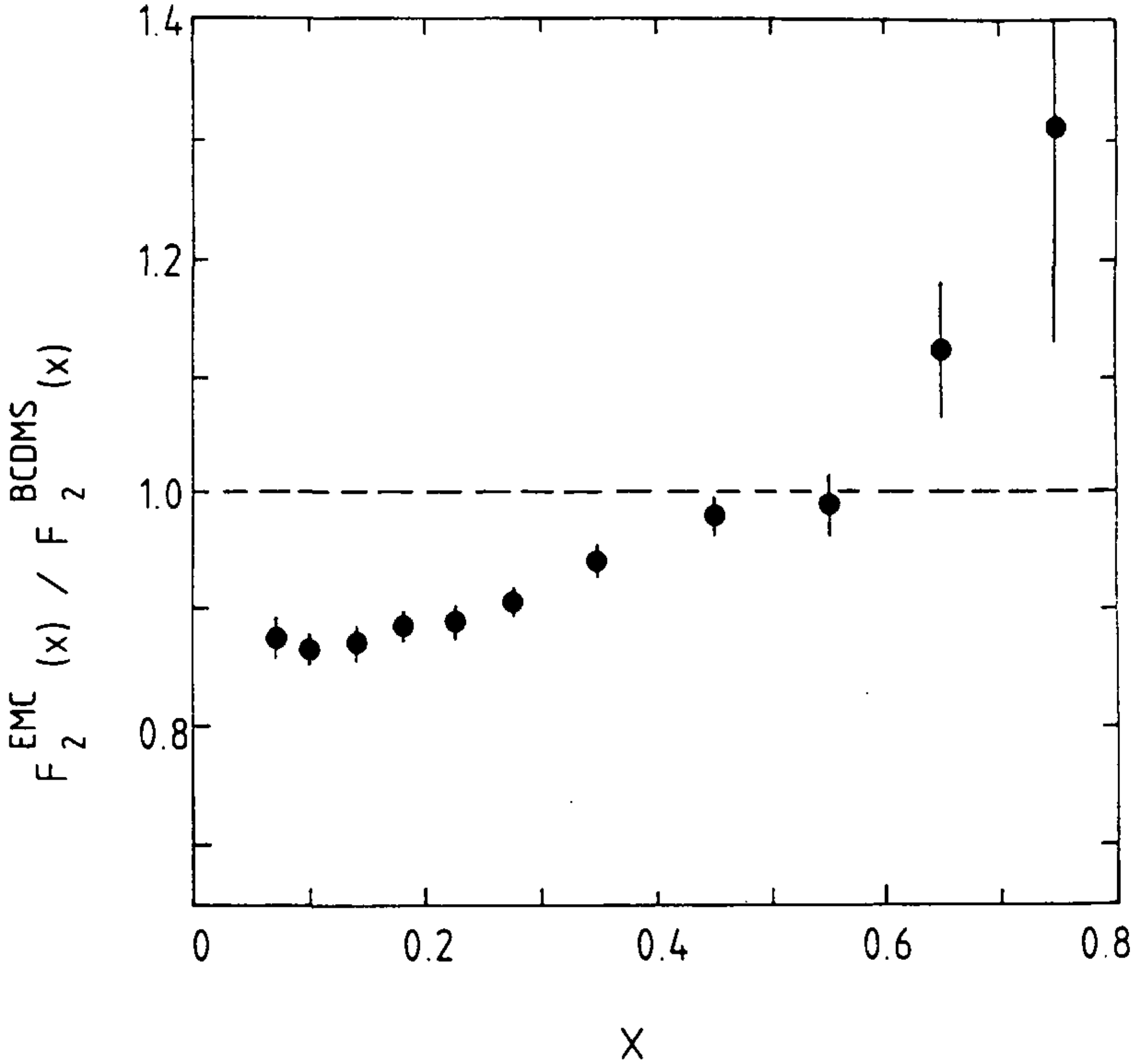

Figure 1.4: The ratio of the EMC to the BCDMS measurement of F_2 proton. Only statistical error are shown.

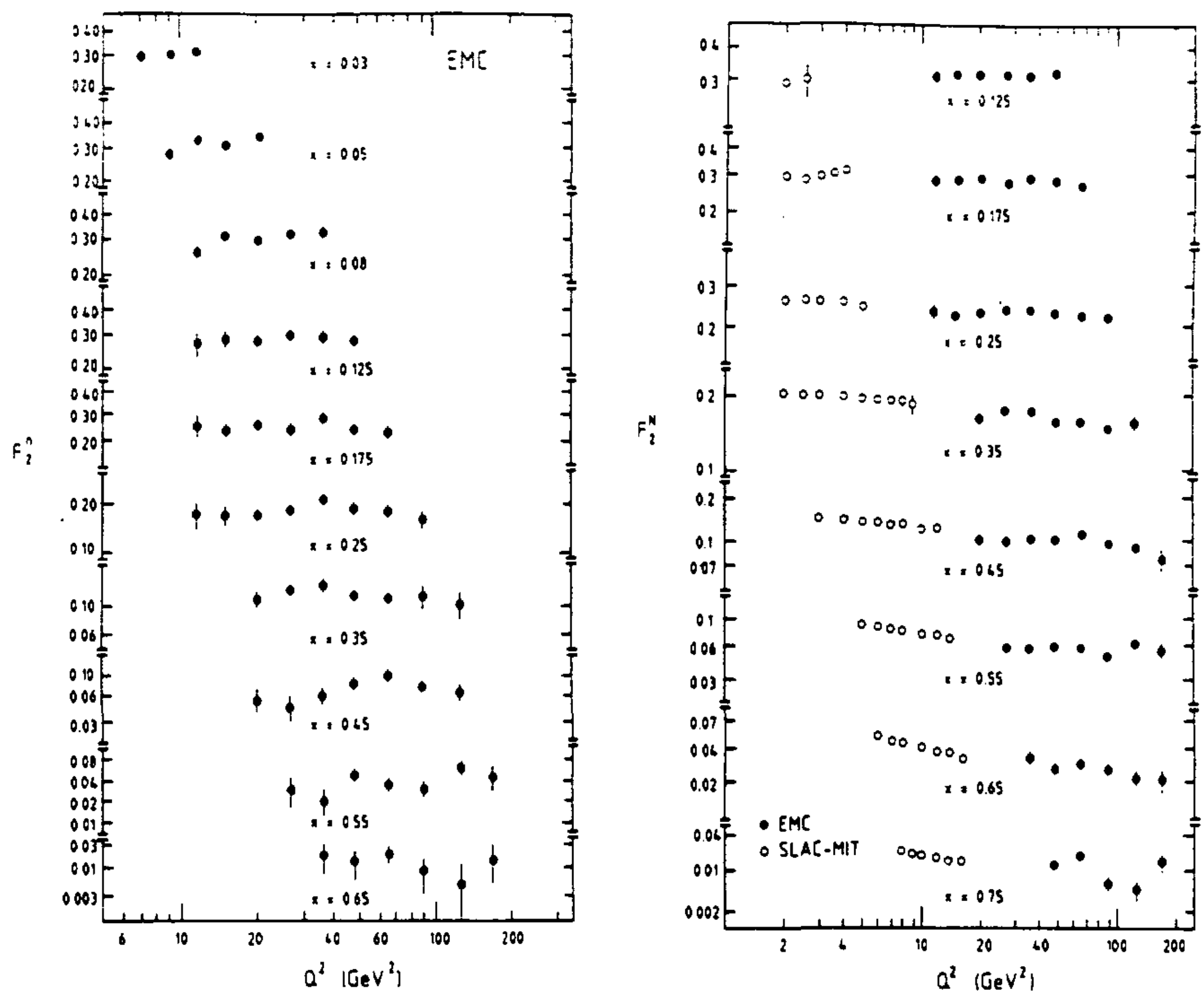

Figure 1.5: Values of F_2 neutron measured by EMC as a function of Q^2 in different bins of x [8]. Comparison of SLAC [9] and EMC [8] data on F_2 deuterium.

Chapter 2

THE EMC EFFECT

In 1983 the European Muon Collaboration published results [13] which showed that the quarks distribution in bound nuclei is different from the distribution in deuterium : this is the EMC effect. Before its discovery, the structure seen in deep inelastic scattering of the nucleon in the nucleus was assumed not to be affected by the surrounding nuclear matter because of the large difference between the energy transferred in the scattering and the nuclear binding energy. The structure function measurable on any nucleus was believed to be the incoherent sum of the individual nucleon structure function :

$$F_2^A(x) = \frac{1}{A}\{ZF_2^p(x) + [A-Z]F_2^n(x)\}$$

where A and Z are the mass and atomic numbers and x keeps always the same definition : $x = \frac{Q^2}{2m\nu}$, with m equal to the nucleon mass. The present pattern of the EMC effect is summarized in two figures: the ratio r_{EMC} between the structure function F_2 for a mean isoscalar nucleon $\frac{1}{2}$ (proton + neutron) in a nucleus and in deuterium is shown in Figure 2.1, whereas its increase with A is given in Figure 2.2. If $R = \frac{\sigma_l}{\sigma_t}$ doesn't depend on the mass number, then r_{EMC} is given by the ratio of the cross sections/nucleon. The only foreseen collective effect is due to the Fermi motion of the nucleon inside the nucleus, which predicts a rise of r_{EMC} at large x; therefore at its appearance the EMC effect was greeted as the possibility of testing the role of quarks and gluons in the nucleus.

Before discussing the different models it is useful to convince oneself that deep inelastic scattering can indeed probe nucleus wide volumes. Our probe is

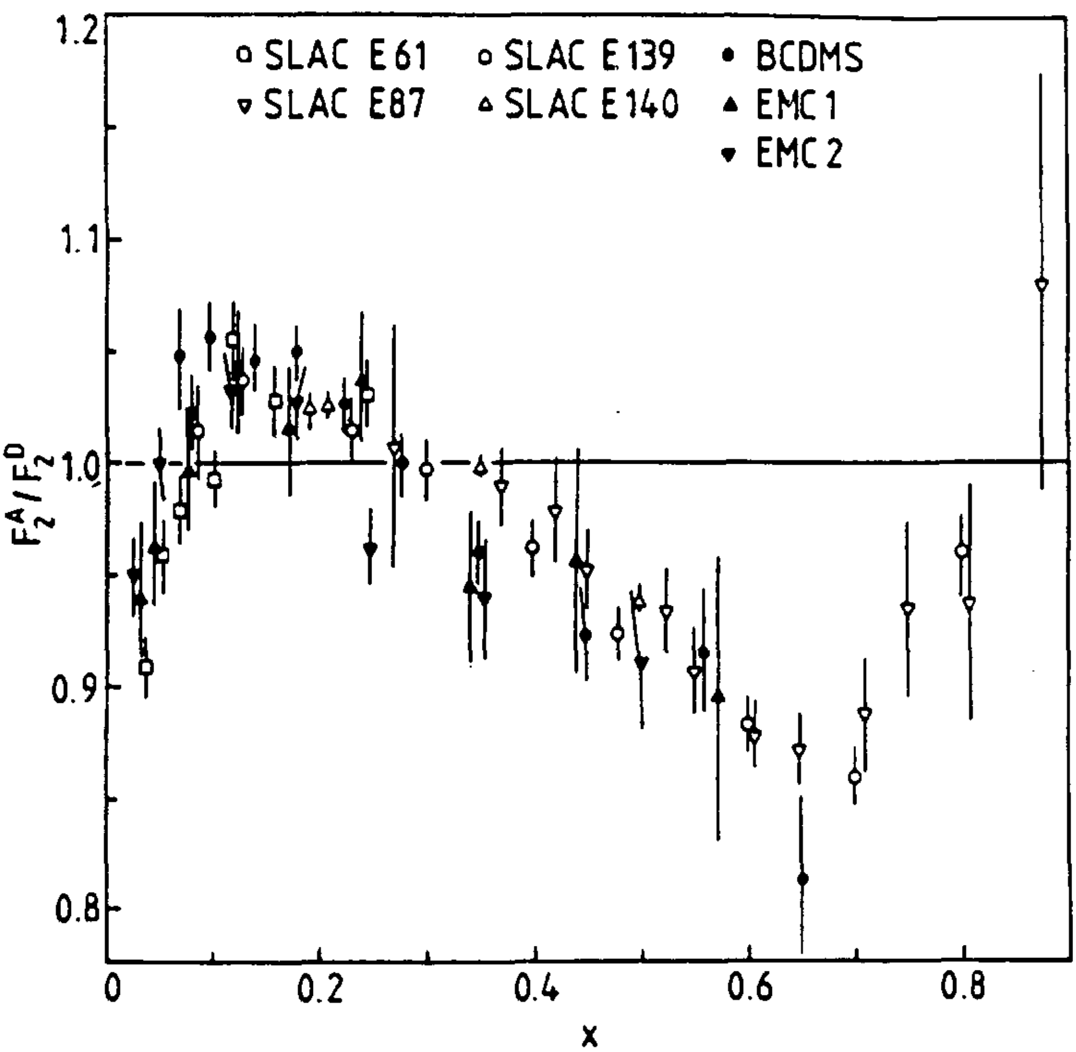

Figure 2.1: The ratio $\frac{F_2^A}{F_2^D}$ from different experiments (A = Cu, Fe).

the virtual photon which, in its rest frame, has a lifetime $\tau \sim \frac{1}{Q}$ according to the Heisenberg principle. In the laboratory frame this corresponds to a distance $\lambda \sim \tau \gamma \cdot \beta = \frac{\nu}{Q^2} \sim \frac{1}{mx}$, where γ is the Lorentz boost factor, i.e., $\frac{\nu}{Q}$, and β is close to 1. Therefore the virtual photon can probe in the laboratory a longitudinal extension $\sim \frac{1}{mx}$ which becomes very large at low x.

There is no model which describes the effect in the whole x range, therefore I will group the different models according to the region they describe.

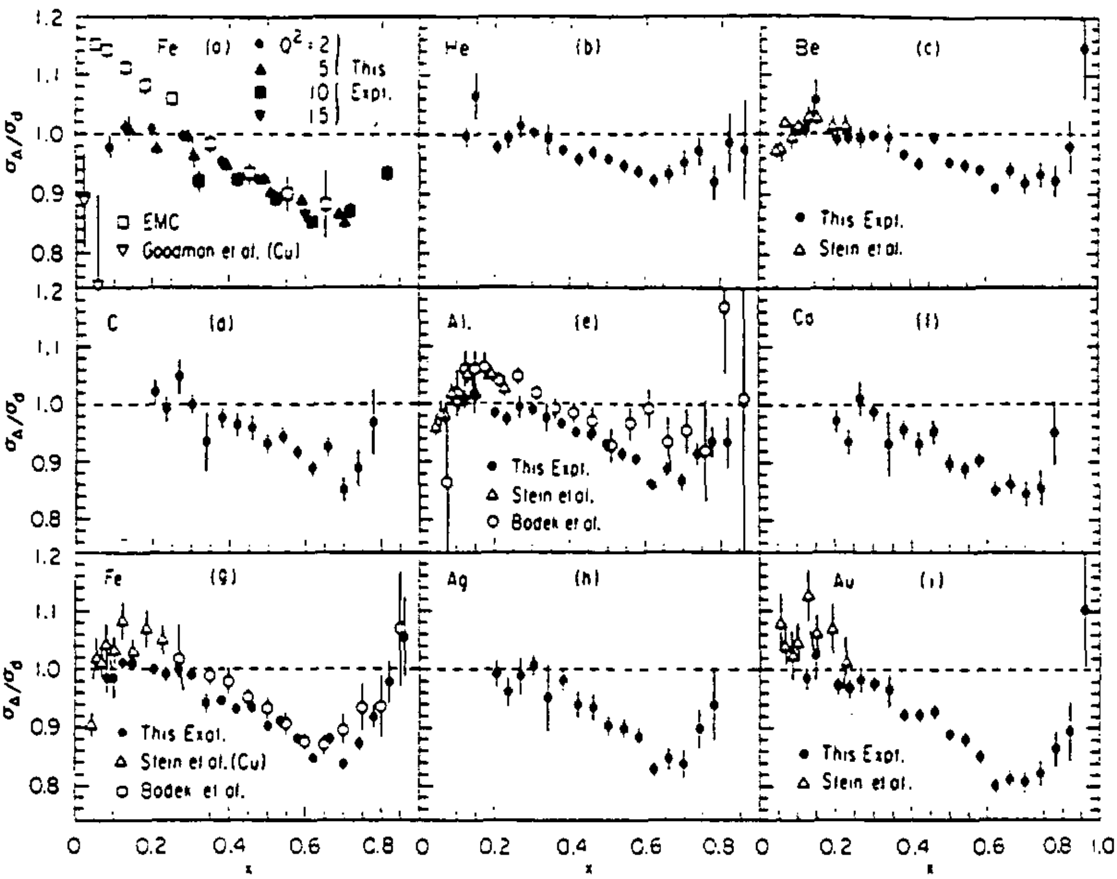

Figure 2.2: A dependence of the EMC effect [15].

2.1 The low x region

Two main models were introduced to explain the EMC effect at low x (x < 0.1), where the ratio of the structure functions drops below 1 : the Vector Meson Dominance and the Parton Fusion.

Real photons show much larger cross section for the production of hadrons than would be expected from electromagnetic interactions. This led to VMD model: a photon fluctuates back and forth between the bare photon state and some collection of hadronic states which strongly interact with the target. If we apply the same scheme to the virtual photon we see that, when the hadronic fluctuation travels a large distance and its nuclear mean free path is small, compared to the nuclear radius, the nucleons in the inner part of the nucleus are shielded, they are in the shadow of the outer nucleons. This argument was used [16] to explain why in the small x region the cross section of the deep inelastic scattering increases less rapidly than linearly with the mass number. The model doesn't explain the antishadowing which is seen in the region between 0.1 and 0.25 and it predicts the disappearance of shadowing at high Q^2 ,in strong contrast with the experimental result [17]. A generalized VMD model, which includes also the massive virtual states beyond the ρ, ω and ϕ, is in better agreement with the data in the shadowing region.

A different interpretation is given by a model proposed in 1975 [18]. The base of this approach is the assumption that at small x partons from different nucleons are in the same region of space and can interact with each other. The fusion of partons belonging to different nucleons doesn't change the total momentum carried by the partons but produces a redistribution of it : the recombination of two partons into one, which therefore carries a larger fraction of the nucleon momentum, generates a depletion in the probability density at very low x (shadowing) and an enhancement at larger x (antishadowing). Let's see in more detail one of these models [19]. In the infinite momentum frame the size of a nucleon and the size of the region occupied by a parton are : $\Delta z_n \sim \frac{2rm}{p}$ and $\Delta z_p \sim \frac{1}{xp}$ where r is the nucleon radius in the rest frame, m is its rest mass and p its momentum in the infinite momentum frame. The onset of shadowing starts at x_c which satisfies $\Delta z_p > \Delta z_n$, that is for $x_c = \frac{1}{2rm} \sim 0.1$. Shadowing becomes stronger as x decreases and it reaches a maximum where the longitudinal size of the region occupied by a parton and of the whole nucleus coincide : $x_A \sim \frac{1}{2mR_N}$, where R_N is the nuclear radius in the rest frame.

In this formulation the model doesn't predict any A dependence of x_c but it explains the very low Q^2 dependence of shadowing : the $\frac{1}{Q^2}$ factor which appears in the expression describing the parton fusion contribution is multiplied and compensated for by the densities of the two partons, which grow as x decreases. If we want to explain the A dependence of x_c ,which seems to increase with A [20], we have to introduce a length scale which decreases with A. The proposed mechanism is a surface versus volume effect. Let's take a nucleus of uniform density and radius R, and let r be the radius of the volume available per nucleon. We suppose that (A − N) nucleons are on the surface and N in the core. The average longitudinal distance between a parton of a nucleon on the surface and another parton of the nearest nucleon is $l_s \sim 2r$ whereas it is $l_c \sim r$ if the two nucleons are in the core. If we define an effective distance between two partons $l_{eff} = \frac{1}{A}[(A-N)l_s + Nl_c]$ we easily obtain $l_{eff} \sim r[2-(1-\frac{2}{A^{1/3}})^3]$: this shows that the distance at which partons begin to overlap decreases as A increases, therefore the point x_c where we have the onset of shadowing increases with A. The model is too qualitative to warrant a detailed comparison with the data.

2.2 The EMC effect in the region x > 0.1

Two families of models were proposed to explain the effect in this region : convolution and Q^2 rescaling models.

The common feature of the convolution models is the decomposition of the nuclear wave function into some conventional constituents : nucleons, nucleons + pions, + deltas, + multiquarks clusters and so on. The structure functions of the constituents are added incoherently to give the structure function for the nucleus :

$$F_2^A(x) = \Sigma_c \int_{y=x}^{A} f_c^A(y) F_2^c(\frac{x}{y}) dy$$

where $f_c^A(y)$ is the probability of finding a cluster c with nucleon momentum fraction y and $F_2^c(\frac{x}{y})$ is the probability of having a quark in it with momentum fraction $\frac{x}{y}$. These models leave the freedom of choosing the clusters, their probability distribution and the structure function of the quarks inside the cluster, so it is not a surprise if they fit well the experimental result, even if the assumption of incoherence at the cluster level is arguable. The simplest of these models is the ' binding + Fermi motion ' one [21]. In this case :

$$F_2^A(x)=\int_{y=x}^{A} f_N^A(y,\varepsilon)F_2^N(\frac{x}{y})dy$$

where ε is the negative average potential energy of the nucleon. It has been shown that there is a rescaling of the nucleon mass which produces a rescaling on x :

$x\rightarrow\frac{x}{1-\frac{|\varepsilon|}{m}}$ but the value of ε required to explain the effect is about a factor two larger than the one measured in electron scattering. Another ' conventional ' model introduced immediately after the discovery of the EMC effect is the pion model [22]. The nucleus is seen as a bound system of nucleons and pions and the EMC effect is due to an excess of pions which mediate the exchange force responsible for nuclear binding. These extra pions produce an enhancement at low x and, because of momentum conservation, a loss of momentum from the valence quarks. Different ingredients were later put into the nucleus, as multiquarks clusters [23]. The idea is that a cluster extends over a larger volume than a nucleon and, because of the Heisenberg principle, the momentum distribution is narrower around the mean value $x\sim\frac{1}{3}$.

The rescaling models are based on the observation that the EMC effect disappears, except in the very low x region, if F_2 obtained from a nuclear target at a certain value of Q^2 is compared with F_2 from deuterium at a larger value of Q^2. In QCD Q^2 is always scaled by a value , μ^2 , which can be regarded as the value of Q^2 for which the nucleon appears simply as three valence quarks confined into a bag of size λ , with $\lambda^2\sim\frac{1}{\mu^2}$ [14]. If the quarks confinement size in a nucleus, λ_A , is larger than in a free nucleon, then $\mu_A^2<\mu^2$ and $\frac{Q^2}{\mu^2}<\frac{Q^2}{\mu_A^2}$. This means that the effective Q^2 for a nucleus is larger than for a free nucleon and at any fixed Q^2 the nucleon in the nucleus appears more QCD evolved : we see more $q\bar{q}$ pairs and softer valence quarks. To reabsorb all the pairs it is necessary to devolve the bound nucleus further than the free one : this is what $\mu_A^2<\mu^2$ means. The rescaling relation $F_2^A(x,Q^2)=F_2^D(x,\xi Q^2)$ implies the EMC effect $F_2^A(x,Q^2)\neq F_2^D(x,Q^2)$. On dimensional grounds we would expect $\xi=\frac{\lambda_A^2}{\lambda^2}$, but we have to consider that the evolution of the structure functions is different in the large and in the small volume. If we require the moments of the structure functions to be equal we obtain : $\xi(Q^2)={\frac{\lambda_A^2}{\lambda^2}}^{\frac{\alpha(\mu^2)}{\alpha(Q^2)}}$, that is the expected value corrected by QCD. Within this model the EMC iron data can be explained by an increase of 15% in the confinement size of the quarks. This increase is fixed, it doesn't vary with Q^2 and it is ascribed to the packing of the nucleons inside the nucleus : the more closely they are packed the more they overlap with each other and the more easily the quarks can leak outside the confinement volume. A relation of the EMC effect with the average nuclear density can be established and an A dependence, with saturation, predicted. It was noticed [24] that there is a duality between the QCD approach and the conventional model of nuclear binding : the essence of each is a single scale change : quarks confinement size in the former and nucleon potential energy in the nucleus in the latter. Both tell that there is a degradation of the energy of the valence quarks in a bound nucleon, in one case this energy is taken by the additional $q\bar{q}$ pairs generated by the evolution, in the other by the additional pions which are believed to be responsible for binding at the 1 Fermi length scale.

An extreme rescaling model has been proposed in [25]. The authors discussed the idea that in a nucleus viewed with high resolution probes the nucleonic structure becomes unimportant and quarks extending over the whole nuclear size are seen. If Q^2 increases the nucleon constituents seen by the virtual photon become ' smaller and smaller ' quarks with less and less longitudinal momentum which are not confined to the nucleon : a transition from colour insulation to colour conductivity is induced. The structure function in a nucleus A at a fixed x is function of $Q^2R_A^2$ and the following scaling is given in the comparison with deuterium at very high Q^2 : $F_2^A(x,Q^2)=F_2^D(x,\frac{R_A^2}{R_D^2}Q^2)$. Colour conductivity relates the EMC effect to a global property of the nucleus : its size; this has two consequences : the A dependence of the effect should not saturate and, since the effect depends on the nuclear radius transverse to the photon momentum, a difference should be seen between the scattering along the short and long axis of a cigar shaped nucleus as, for instance, Ho^{165}.

To my mind the review of models has been perfectly sumarized in [26] : "... no model has emerged yet that gives a satisfactory explanation of the available data and each model describes just facets of the nuclear effect which can only be part of the ultimate theory of the nucleus in terms of quarks and gluons ".

Of course this is also due to our limited experimental picture of the EMC effect . One of the main purposes of NMC is to make it more complete [3], looking at the Q^2 dependence of r_{EMC} at large and low x, at the A dependence of $R=\frac{\sigma_l}{\sigma_t}$ in the whole x region, and at the A dependence of r_{EMC} in the low x region . Part of this program will be covered in this thesis, in which I will discuss the cross section ratio between Calcium, Carbon and Lithium for 90 GeV incident muons. I will show their x dependence in the low x region, with a particular care of the radiative corrections, their Q^2 dependence and, finally, I will comment on the dependence on A.

Chapter 3

THE BEAM AND THE DETECTOR

3.1 The beam

The experiment uses the muon beam line M2 of the SPS of CERN [Figure 3.1] .
The layout of the beam [Figure 3.2] is divided into four parts : the front end, the decay channel, the hadron absorber and the back end [27].

3.1.1 Front end

This section selects parent pions and kaons produced in the 50 cm long beryllium target T6 by 400 GeV/c protons. Its main components are :

1. a serie of six quadupoles with which it is possible to collect secondary particles in a given momentum range,

2. a bending magnet (B1) which gives a horizontal deflection of 18 mrad for the central beam momentum. It is followed by a drift distance of 20 meters to remove the unused primary protons. It is possible to reach a momentum band ΔP for which $\Delta P/P < 10\%$,

3. a bending magnet (B2) which gives a vertical deflection of 9.6 mrad needed by the raising contours of the site, and

4. a last magnet (B3) which gives a 8 mrad horizontal deflection to compensate for the dispersion before entering the decay channel.

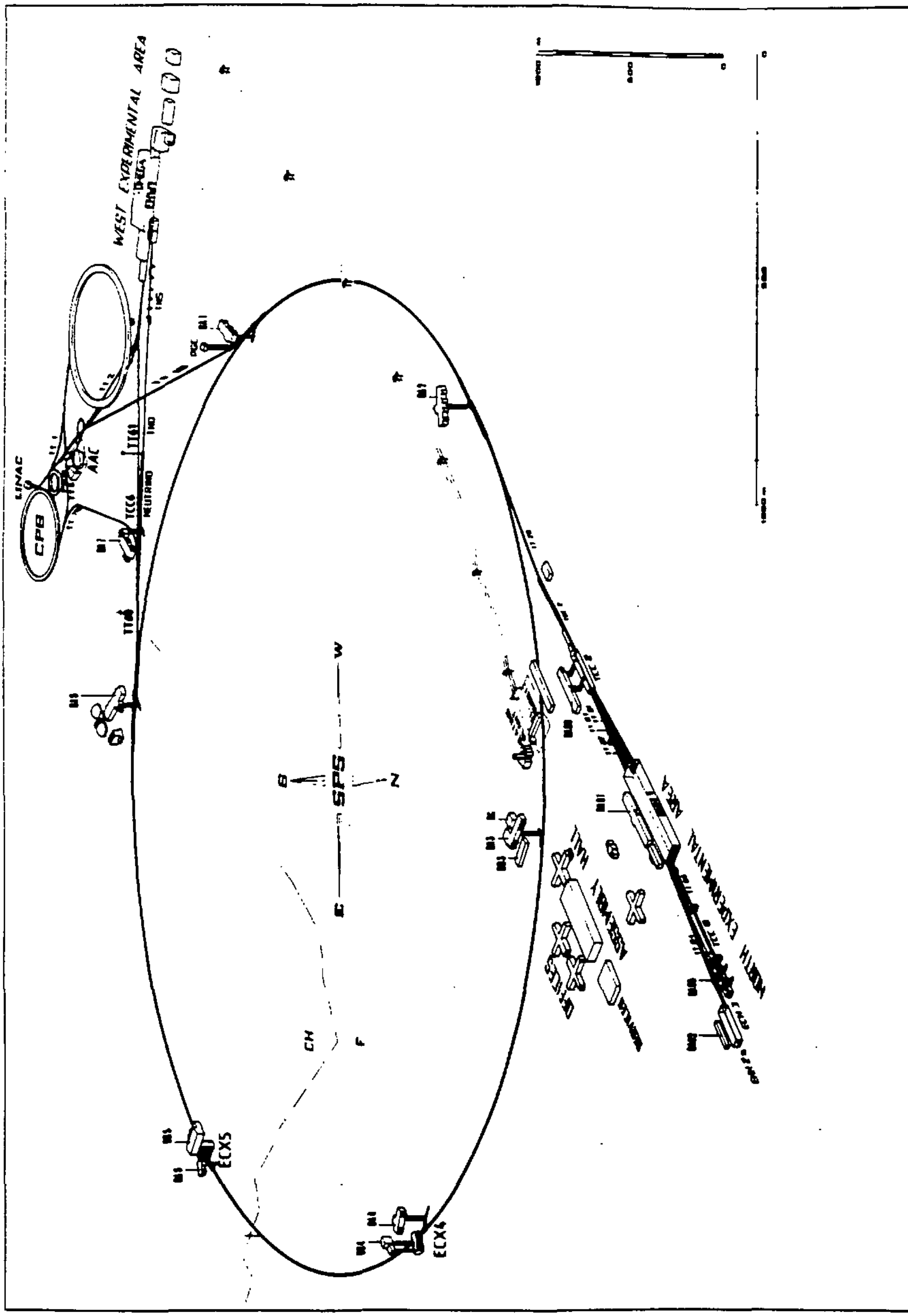

Figure 3.1: The SPS Site at CERN

3.1.2 Decay channel

It is 600 meters long and it is composed of a serie of large acceptance 20 cm diameter quadrupoles with alternating gradients. The action of the quadrupoles is optimized in order to achieve a minimum loss in the parent beam of pions with the central momentum P_0 and in the wide momentum band of the muons resulting from their decay ($0.57P_0(\pi) < P(\mu) < P_0(\pi)$).This allows the selection of muons with either polarization. The highest polarization which can be reached is 80% .

3.1.3 Hadron absorber

At the end of the decay channel only a fraction of the pions will have decayed (5% for $P_0(\pi) = 200$ GeV/c and 10% for $P_0(\pi) = 100$ GeV/c) and 25% of the produced muons are in the momentum band which can be selected and transported to the experiment. A π/μ contamination of the order of 10^{-6} can be reached with a 10 meters long hadron absorber. The multiple scattering of the muons is minimized by the choice of beryllium as absorber material. The absorber is located in the aperture of the momentum analysing magnets (B4+5) , to prevent muons of unwanted momentum to appear after the muon momentum selection stage.

3.1.4 Back end

It selects and transports the muons to the experiment. B4+5 are used to produce a vertical deflection of +24 mrad for the central momentum P_0 (μ) of the selected muons.The following quadrupoles are able to collect a momentum band $\Delta P/P_0(\mu)$ of $\pm 6\%$. A system of magnetic collimator, made of 5 meters long magnetised iron blocks with a 1.5 Tesla toroidal field and a field free gap for the beam, scrapes off the muons surrounding the beam and deflects them laterally away from the beam line. Each block cuts a bit into the beam, enabling to optimize the halo to beam ratio. A system of alternating gradient quadrupoles, similar to that used in the decay channel,transports then the beam over 312 meters to the system magnet B6 and B7, which produces a vertical deflection of −24 mrad. These magnets, together with the preceding and succeding quadrupole sections, form a focusing spectrometer with which a resolution $\Delta P/P_0(\mu) = \pm 0.3\%$ can be achieved. A final set of quadrupoles and bending magnets,giving a vertical deflection of −9.6 mrad , brings the beam in the experimental zone

EHN2.

The length of the different sections is the following : front end 112 m , decay channel 588 m , back end 396 m , for a total length of 1096 m .

3.1.5 Flux

One 400 GeV/c incident proton on the production target T6 gives roughly 3.8×10^{-5} , 1.4×10^{-5} and 1.8×10^{-5} positive muons with a mean momentum of 90 , 200 and 280 GeV/c respectively.For negative muons the fluxes are lower by a factor between 2.5 and 5 in the momentum range between 90 and 280 GeV/c. We worked with an intensity of about 10^7 μ per second.

3.1.6 Dispersion

The dispersion, measured in front of the detector, for momenta between 90 and 280 GeV/c,are the following : r.m.s. in the spatial distribution from 15 to 20 mm and r.m.s. angular divergences from 0.4 to 0.5 mrad vertically and from 0.2 to 0.4 mrad horizontally.Two pairs of wire chambers are available for the observation of the beam : at the entrance of EHN2 and at the far end of the apparatus 38 meters downstream.

3.1.7 Halo

The natural muons halo reaching the big veto wall of the experiment (V_3) is about 75% of the beam intensity , mainly coming from the absorber region.This large halo is reduced by means of the magnetic collimators (scrapers) to about 7%. The beam is tuned for every muon energy.The tuning is done in three successive steps : horizontal and vertical dipole steering , horizontal and vertical quadrupole focusing , halo optimization.

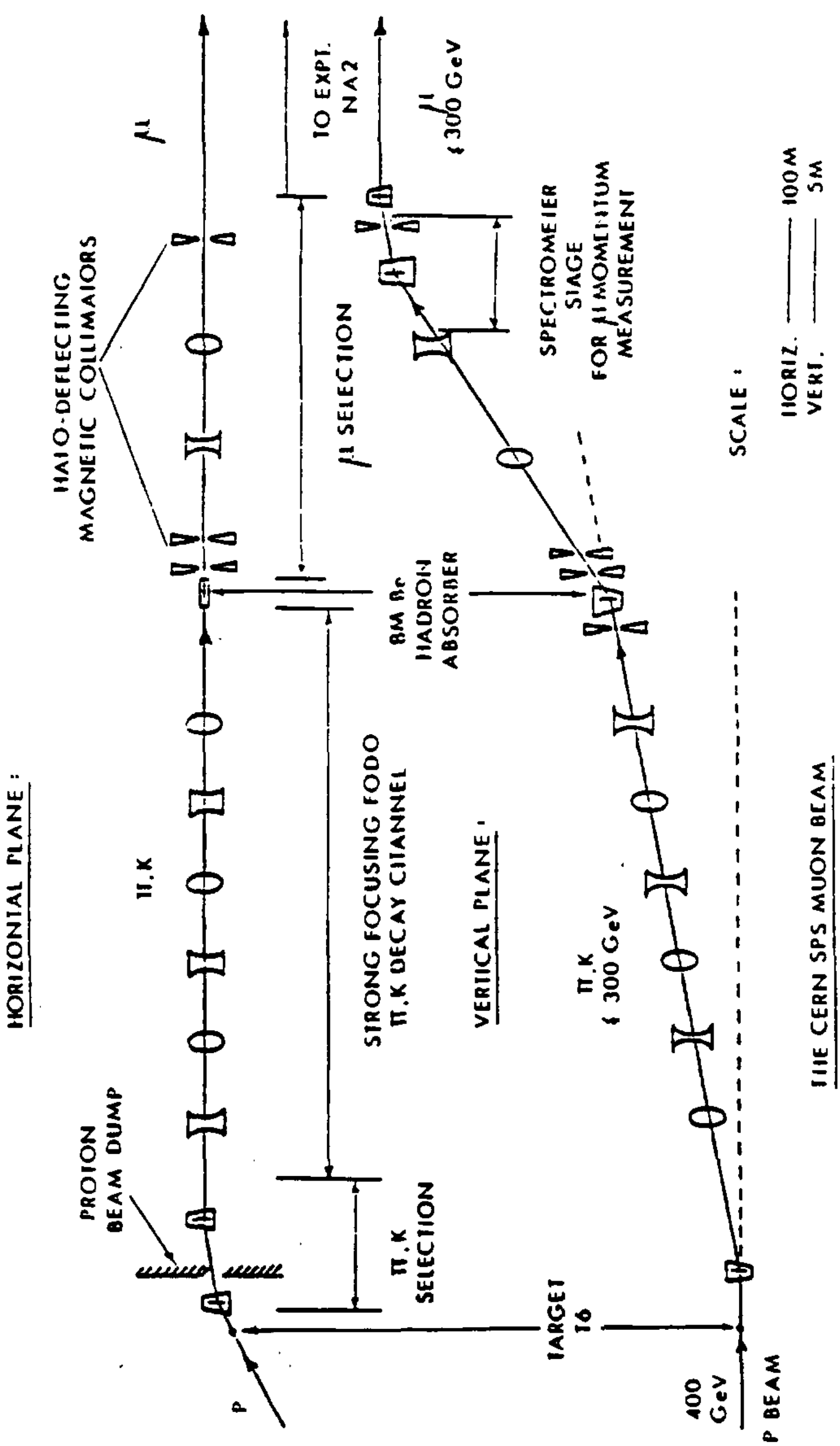

Figure 3.2: The Beam Layout

3.2 The detector

3.2.1 General overview

What we are interested in is the inclusive cross section of the deep inelastic μ scattering. For its determination we have to measure the angle between the incident and the scattered μ and their energies. In our set up [Figure 3.3], which is an upgraded version of the EMC spectrometer [28], the μ enter from the left, their energy is measured in the beam momentum station (BMS) located in the back end, their position and direction are determined in the beam hodoscopes (BHA and BHB).
If it interacts,the scattered μ is identified in the drift chambers W_6 and W_7 after a 2 meters thick iron absorber ; it is traced through many proportional and drift chambers back to the vertex in the target and its momentum is measured with a magnetic dipole (FSM). A calorimeter in front of the absorber (H_2) roughly measures the electromagnetic and hadronic components of the interaction products.

The center of the FSM magnet is defined as the origin of the NMC frame, a right handed system with the x axis along the beam direction and the z axis upward along the vertical direction.

Here are the performances of the detector : the momentum of each incident μ is determined with an accuracy of $\pm 0.3\%$, its track is reconstructed with an accuracy of 0.15 mrad in angle and better than 1 mm in position . The resolution on the scattered μ momentum is limited by the spatial resolution of the chambers. It has been found to be of the order of $\pm$ 1.3%. The accuracy in the angle of the reconstructed track is of $\pm$ 0.23 mrad and the vertex resolution along the x axis is $\pm$ 5 cm and $\pm$ 2 cm in the upstream and downstream part of the target respectively . The different elements of the detector are described in the following pages.

3.2.2 Hodoscopes in the beam

They are fast scintillation counters which measure the beam momentum (BMS), position (BHA and BHB) and intensity (H_5). They do not participate to the electronic trigger .

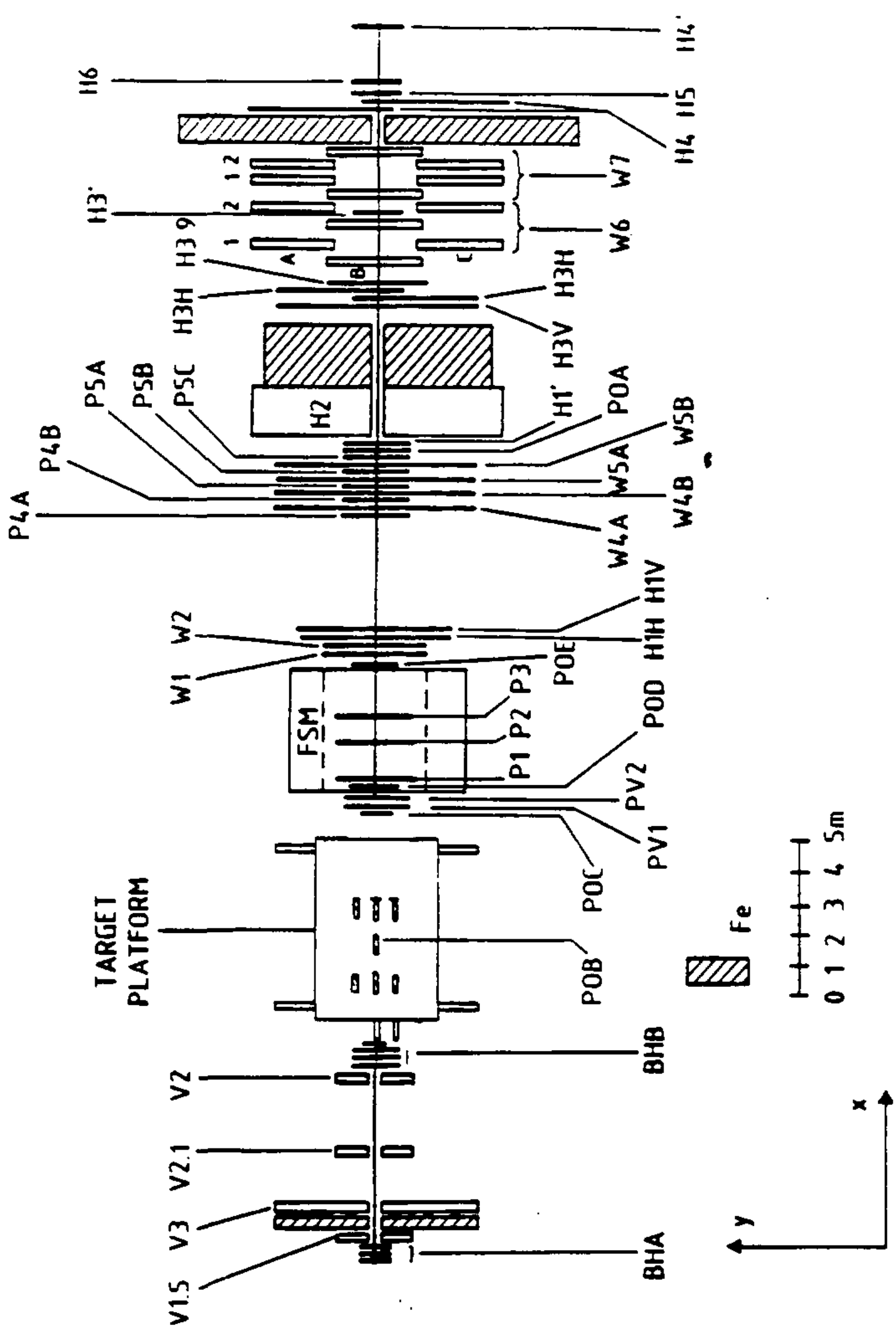

Figure 3.3: Experimental Setup

3.2.3 Beam Momentum Station

The last vertical dipole B6 , together with the quadrupole doublets on each side of it , is used as a focusing spectrometer [Figure 3.4] .

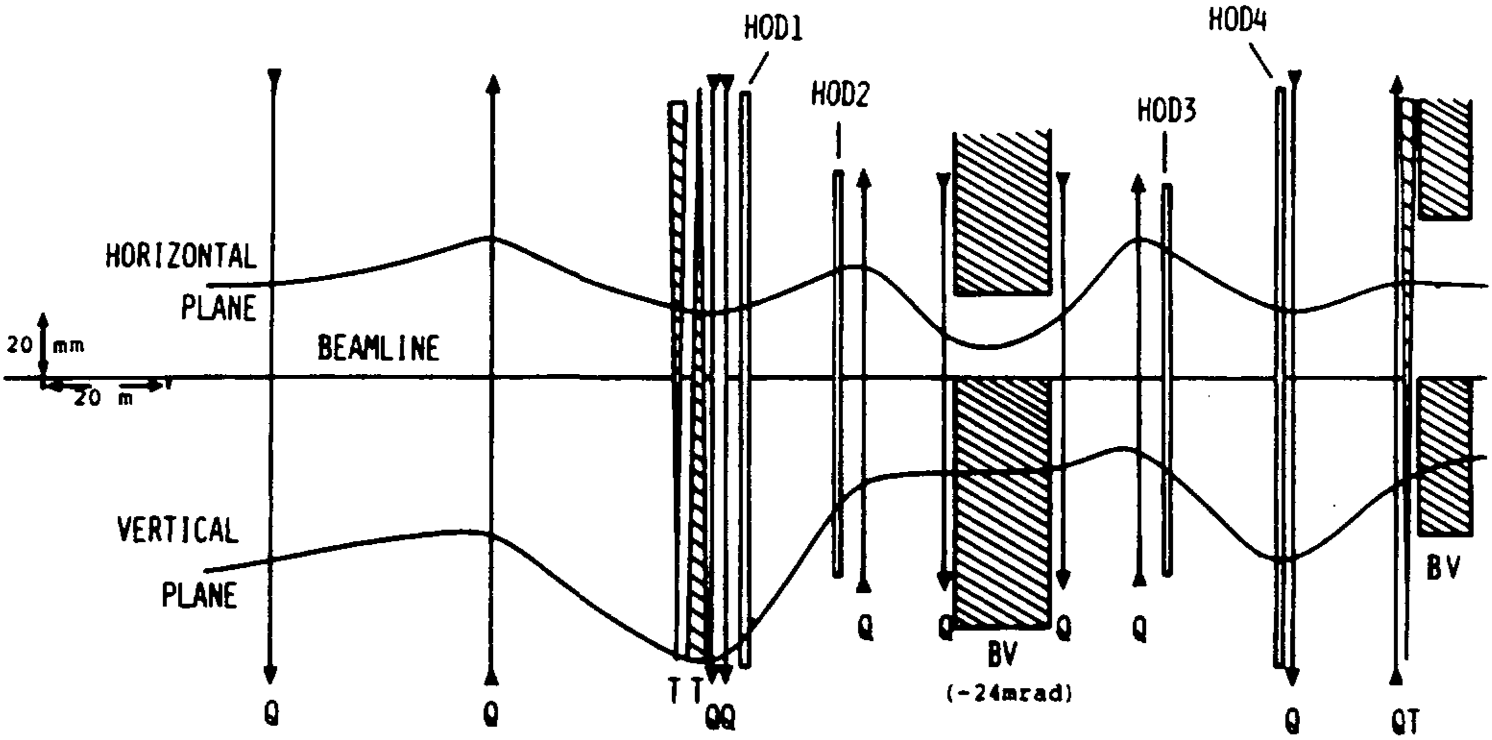

Figure 3.4: Beam Momentum Station

Four horizontal planes give the position of the μ . Each plane is made of 64 elements , 2 cm thick and 5 cm wide , with small overlap between adjacent elements to increase the efficiency .The elements which are in the central region of the planes have a different length in order to stand a rate $< 3\times10^{7}$ μ/s in any element. For the reconstruction of the track it is necessary to have a very accurate timing of the BMS elements and of the BMS relative to the detectors in the forward spectrometer . The first is checked on−line , using laser light piped to each element by fibre optics ; an accuracy of 100 ps is reached in the off−line analysis. The second is obtained by timing the BMS to an element in the forward spectrometer (H_3V), with an accuracy of 300 ps. A Monte Carlo simulation was made to obtain the relationship between the hits produced by a μ in the 4 planes and its momentum . The accuracy in the momentum determination is $\pm0.3\%$.

3.2.4 Beam Hodoscopes

The beam hodoscopes BHA and BHB are placed upstream of the target , with a separation of about 6 meters . Each hodoscope consists of 4 planes perpendicular to the beam direction and with a different orientation : $\theta \pm 30°$, z, y for BHA and and y, z, $\theta \pm 30°$ for BHB. Each plane is divided into two 8×8 cm subplanes made of 20 strips with a cross sectional area of 4×4 mm^2 and 8 cm long in the direction perpendicular to the beam . The two subplanes are shifted with respect to each other by 2 mm to improve the spatial resolution. The light from each strip is collected by a 19 diameter phototube through a plexiglas ligth guide . A time resolution of 200 ps and an accuracy of 700 ps in the BHod $-H_3V$ timing are achieved . The efficiency over a whole plane is better than 99% . The hardware is checked on $-$line by sending LED pulses to each scintillator strip outside the μ spill .

3.2.5 H_5

H_5 was introduced to measure the beam intensity up to rates of 4×10^7 μ/s . It consists of two 19×21 cm^2 planes of scintillators placed at the end of the detector . The two planes are divided in 4 and 5 elements , in order to have a rate on each element $< 10^7$ μ/s , and they have a thickness of 1 cm to achieve a good efficiency . Each element is seen by a photomultiplier ; the signals from one plane are mixed and , if in coincidence with the other plane , are counted by a scaler .

3.2.6 Veto

The veto system consists of five sets of counters : V1, V1.5, V2, V2.1, V3 [Figure 3.5] .
Their action is to define the part of the beam which we use to generate triggers. V1 , which is placed between B6 and B7 in the muon line , and V1.5 , downstream of BHA , are used to reject the small angle halo component close to the beam . V3 , downstream V1.5 , suppresses the large angle halo μ ; a 40 cm thick iron wall just in front of V3 is used as a support and to reduce the soft component of the beam . V2 and V2.1 , placed a few meters apart and with a central hole of 6 cm diameter , define a cylinder within which muons are directed towards the target material . V2 has 2 photomultipliers per element , all the other planes have only 1 photomultiplier per element . The signals from the photo-

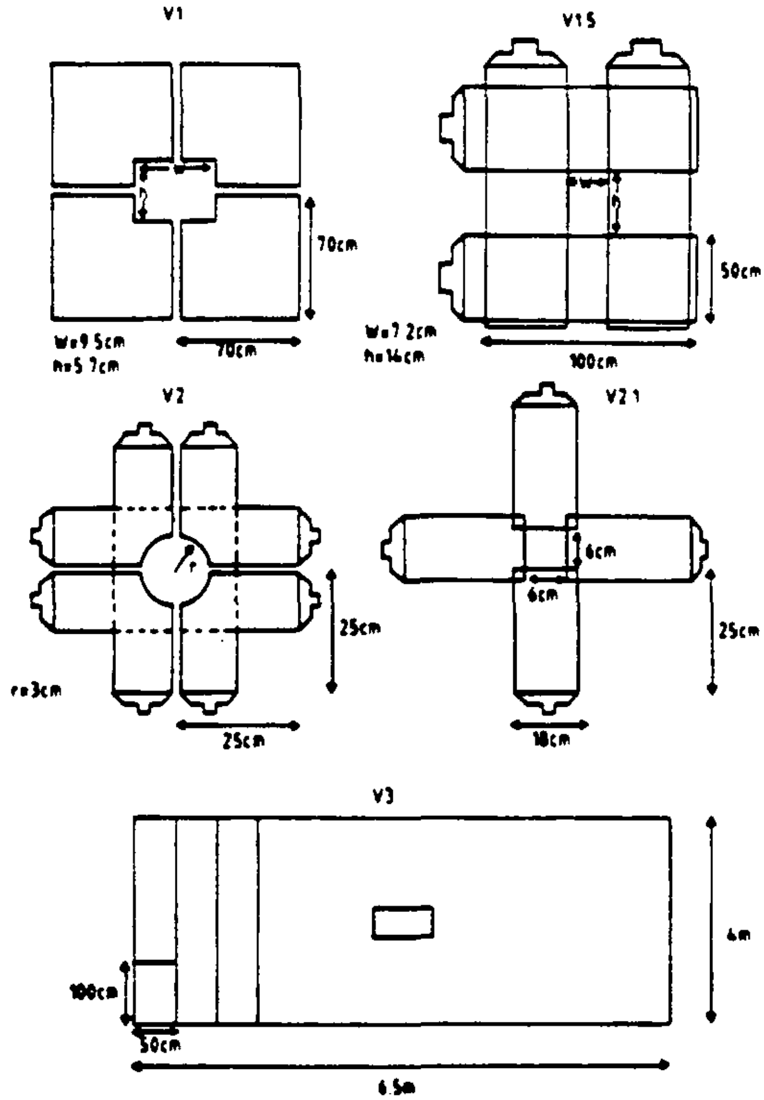

Figure 3.5: The veto counters

multipliers are ORed and used to inhibit triggers (except the normalization trigger T_{10}) . Around 7% of the beam counted by H_5 is thus vetoed, mainly by V3. The background rate from all the veto counters without beam is of the order of 5×10^4 Hz.

3.2.7 The forward spectrometer magnet (FSM)

It is a magnet with a field volume 4.3 m long, 2 m wide and 1 m high. Two water-cooled copper coils are used to produce a field in the z direction. At 90 GeV we had $\int_{-3.3}^{3.3} Bdl$ = 2.328 T×m with a current of 2000 A . It is possible to work with a maximum current of 5000 A. The magnetic field was measured for different values of the current with a set of Hall probes, showing r.m.s. deviations of the measured field from the predicted of the order of 5 gauss. It is possible to reach an accuracy in the measurement of $\int^{l} B dl$ better than 0.2%. During data aquisition the value of the field is continuosly checked by a Hall probe.

3.2.8 Trigger hodoscopes

The forward spectrometer has 8 planes of trigger hodoscopes to sense the position of the scattered μ, 5 are used for the standard trigger T_1 and the other 3 are used for the small angle trigger T_2. Let's consider first the hodoscopes used for T_1. H_1H, H_3H and H_4H are made of horizontal elements which measure the vertical position of the scattered μ. They are located behind the magnet (H_1), behind the absorber (H_3) and at the back of the apparatus. H_1V and H_3V consist of vertical elements and give the horizontal coordinate. An adjustable hole in each hodoscope plane permits to adjust a lower limit of the selected $Q^2 - \nu$ region [Figure 3.6].
The elements width of H_1 and H_3 is determined to adjust the θ cut by 0.5° steps. A 40 cm thick iron wall, with a 30×20 cm^2 beam hole, is placed in front of H_4 to absorb soft electromagnetic showers. The elements of H_3H and H_4H are divided into two parts, with a maximum length of 5 m and an overlap of 14 cm. Each end of the scintillator is connected with a ligth guide to a photomultiplier fully efficient for a minimum ionizing particle crossing the opposite end of the element. Meantimers are used to obtain an output signal which is independent of the particle position along the scintillator to within ± 1 ns. The elements of H_3V are connected to TDCs, and this time is used as the event reference time.

To cover the small Q^2 region, a small angle trigger was introduced (T_2). It's made of three hodoscopes placed in front of the calorimeter (H_1') , between the last drift chambers W_6 and W_7 (H_3') and at the back of H_5 (H_4'). Each hodoscope is split up in two halves, leaving a gap in the beam region, and 50 cm long horizontal strips viewed by one phototube. The size of the gap defines the minimum angle for the detection..

A last hodoscope H_39 is introduced in front of W_{67}. It covers a surface of 1×0.5 m^2 with a 15 cm diameter hole for the beam ; it is used only for the alignement trigger T_6 .

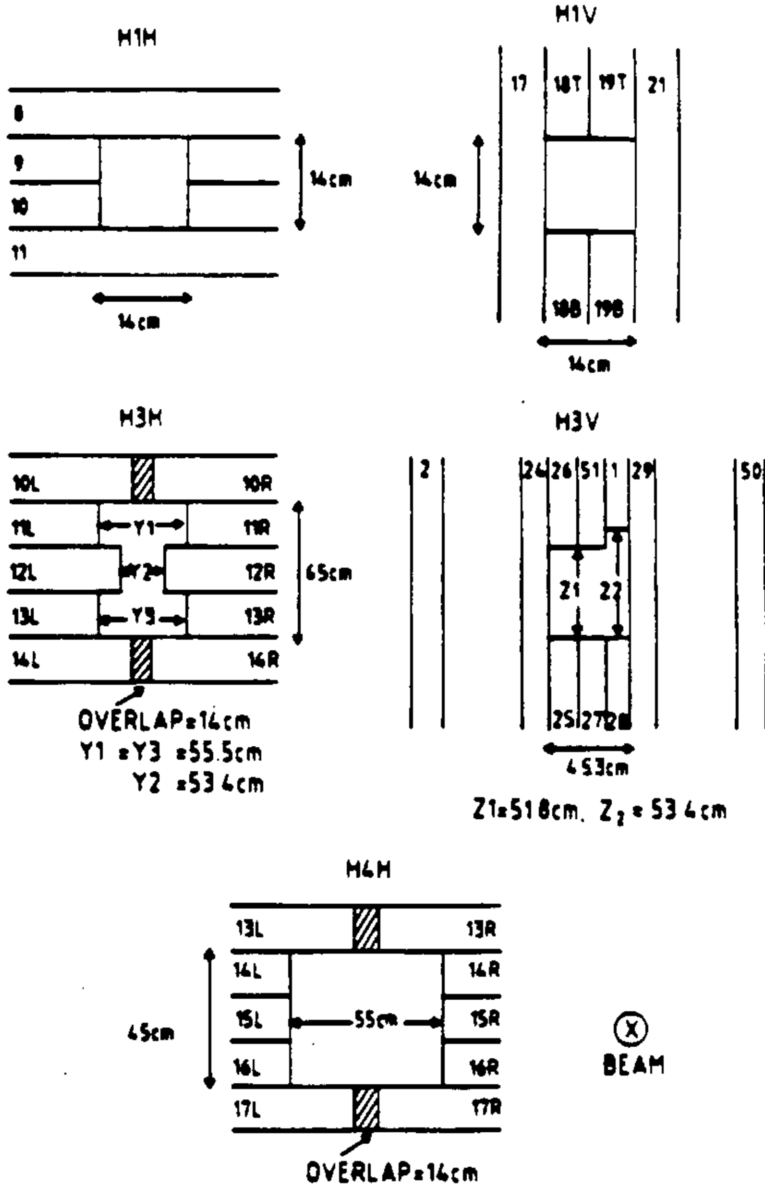

Figure 3.6: Trigger hodoscopes beam holes

3.2.9 The calorimeter H_2

It is placed upstream of the passive absorber. Its purpose is to identify the particles (electrons, muons and hadrons) and to measure their energy . The calorimeter is divided into two halves, right and left to the beam. Each of them consists in three separate modules : an electron module, made of lead plates, and two hadron modules made of iron plates [Figure 3.7].
Between the plates are inserted forks of scintillators; they are blades of scintillators shaped so that all the blades in each fork are viewed by a single photomulti-

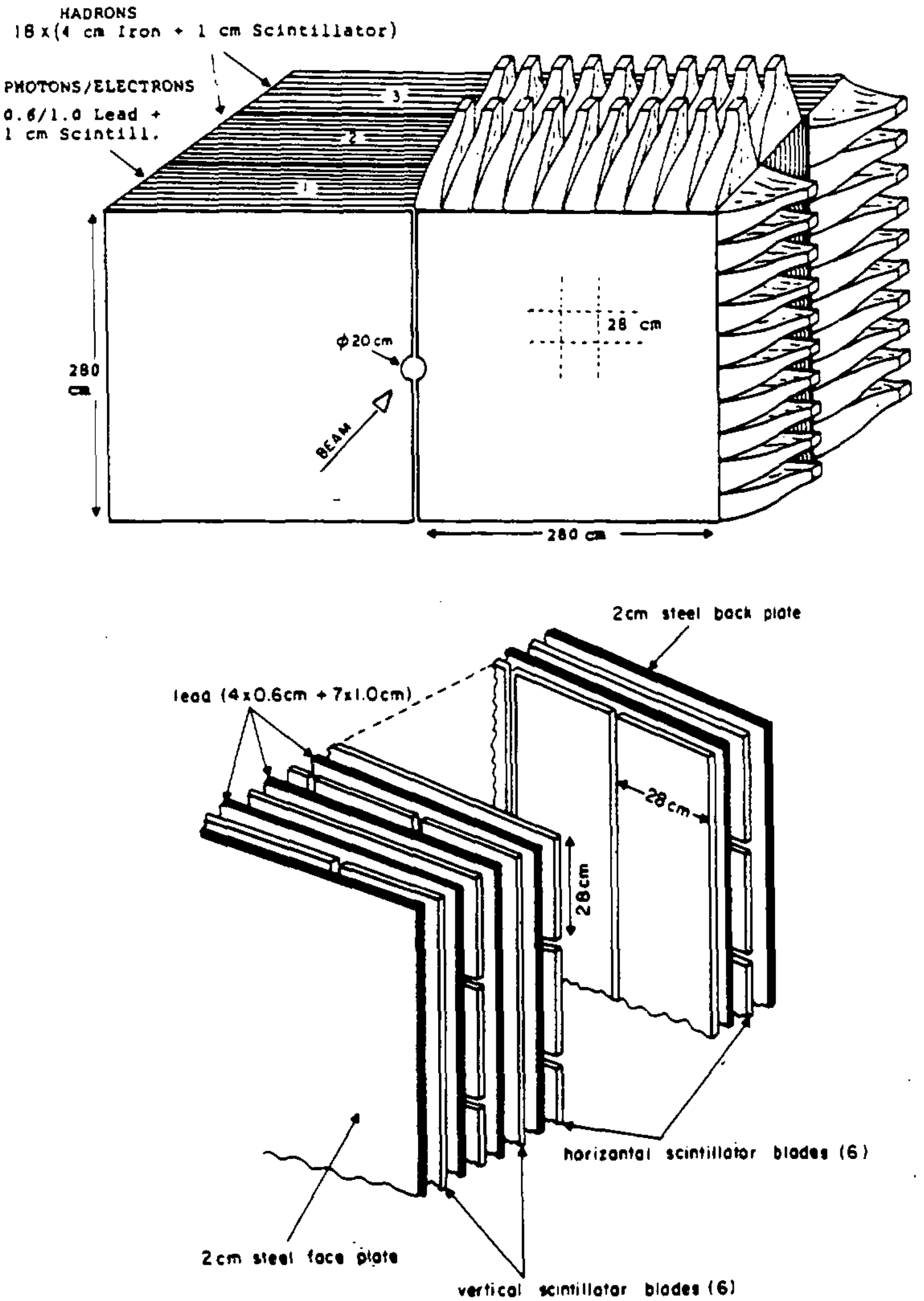

Figure 3.7: The calorimeter H_2

plier. A yellow filter is used to remove the far blue component of the light spectrum which is the most sensitive to the attenuation. In the electron module vertical and horizontal forks are interleaved, and this permits a pattern recognition of the showers. The material in this module amounts to 22 radiation lengths and 0.95 interaction lengths and it is enough to fully contain th electromagnetic showers in our energy range. The two downstream hadron modules contain only one set of vertical scintillators in the forward module and horizontal scintillators in the second. They are made of 4 cm thick iron plates. The total thickness of material in the calorimeter is $\simeq 5.5$ interaction lengths. A 20 cm diameter hole is left for the beam. There are 80 photomultipliers associated with the calorimeter; the signal from each of them is divided and amplified into two sub-channels. The relative gain of these sub-channels is 50 : 1. It is thus possible to detect both minimum ionizing particles with the high gain channels and 250 GeV showers with the low gain channels. The energy resolution, measured with a test beam, is : $\frac{\sigma}{E} = \frac{0.4}{E^{0.5}}$ (energy in GeV) for electrons in the lead module only, $\frac{\sigma}{E} = \frac{1.5}{E^{0.5}}$ for hadrons in the whole calorimeter.

Immediately downstream H_2 there is a 2 m long iron passive absorber, with a 20 cm diameter hole for the beam. Every particle traversing it is identified as a muon.

3.2.10 Proportional and drift chambers

The track of the scattered μ is reconstructed with the information given by the large drift chambers after the magnet (W_{12}) , before (W_{45}) and after the absorber (W_{67}), and with the proportional chambers in the beam region (P_0s) , close to the beam region (P_{45}) , in front (PV_1 PV_2) and inside the magnet (P_{123}).

Proportional chambers can be operated in high beam fluxes, but each wire needs its own readout electronics ; this means that they cannot be used to cover a large surface because they become very expensive . Where the particle flux is low, it suffices to use drift chambers. In this way it is possible to reduce the number of sense wires.

Very important is the choice of the gas to fill the chambers ; this is a mixture of a noble , a polyatomic and an electronegative gas , sometimes with the addition of propylic alcohol or methylal. The noble gas , argon, is dictated by its high specific ionization. The polyatomic , isobutane , is the quencher : it absorbs the photons and dissipates the energy in non radiative processes. The electronegative gas , freon , gives the possibility of reaching the highest gain before discharge.The propylic alcohol or the methylal are added as non polymerizing quenchers to suppress the ageing of the wires . The mixture of the different gases, in fixed ratios , continuously flows through the chamber. The flows of gas are controlled by the 'rotameters' which use light sensor to detect the position of 'float' in glass flov' tubes.

3.2.11 P_0s

They are multiplane proportional chambers situated in the high rate beam region to provide good track reconstruction at small angles and good vertex resolution in the target. There are 5 P_0s, 16 cm in diameter each, and they can work in beam intensities up to 10^8 μ/pulse . Each chamber has 8 circular planes of 144 10 μm gold-plated tungsten wires spaced by 1 mm. There are 4 pairs of planes with different orientation y, z, θ^+, θ^- ; a 0.5 mm shift between the two planes of a pair gives an effective wire spacing of 0.5 mm. Each wire plane is enclosed into two graphited mylar cathode planes to which the negative hv potential is applied.

3.2.12 PV_1 and PV_2

They are mounted in front of the magnet and they have a sensitive area of 1.3×0.8 m^2 and 2.8×1 m^2 respectively . Each chamber contains six planes of anode wires, two vertical, two inclined at $\pm45°$ and two at $\pm18°$. The separation between two 20 μm diameter gold-plated tungsten wires is 2 mm ; the central region of the chamber is made insensitive with the insertion of a beam killer.

3.2.13 P_{123}

These three chambers are located inside the magnet . Each chamber has three planes with 2 mm wire spacing .: vertical, horizontal and inclined at 20°. They cover a sensitive area of 1.8×0.8 m^2 . There are four cathode planes per chamber, made of 100μm diameter berylium-copper wires and in the central part of the chamber there is a kapton beam killer .

3.2.14 P_{45}

They consist of two sets of 2 and 3 proportional chambers interspaced between the drift chambers W_{45} for tracking particles near the beam region where W_{45} is relatively inefficient. They are dodecagonal with an inner diameter of 0.9 m. Each of them consists of two anode planes , y and θ , with an angle inclination of $\pm 30°$.

3.2.15 Drift chambers

We use chambers with different cell sizes in order to reach a good compromise between the economy of electronics and the rate of the individual wire. This rate is essentially due to halo muons and knock – on electrons in the time acceptance of the chamber. The basic drift cell has a few centimeters size and it consists of a region of moderate electric field , shaped by potential wires , followed by a proportional counter [Figure 3.8].
All the sense wires are made of gold – plated tungsten with a diameter of 20μm. W_{12} consists of two 8 planes modules with a sensitive area of 1.2×2.2 m^2. W_{45} is in front of the absorber and has four modules, each of 4 planes, with a size of 2.6×5.2 m^2 . W_{67} is after the absorber at the end of the spectrometer and it has a total sensitive area of 10×4.4 m^2. It is divided into three section A, B, C, each composed of four modules. Section A and C have 11 measuring planes, whereas the central section B , where the halo flux is higher, has 16 planes. Because of the beam flux the central region of all the drift chambers is made insensitive . The main parameters of the chambers are sumarized in [Table 3.1].

3.2.16 The target

The target setup is shown in [Figure 3.9].
All the 6 targets of a row are in the beam at the same time , and they are replaced by a parallel row after $\simeq$30 minutes, in order to have the same total acceptance for the different targets in the same position. We will see that it is possible to calculate the ratio of the cross sections of Li, C, Ca considering only the 9 targets in the upstream part , or only the 9 in the downstream , or all the targets together without needing neither the flux nor the acceptance . Because of this nice feature of the complementary setup, it is possible to minimize the systematic error.

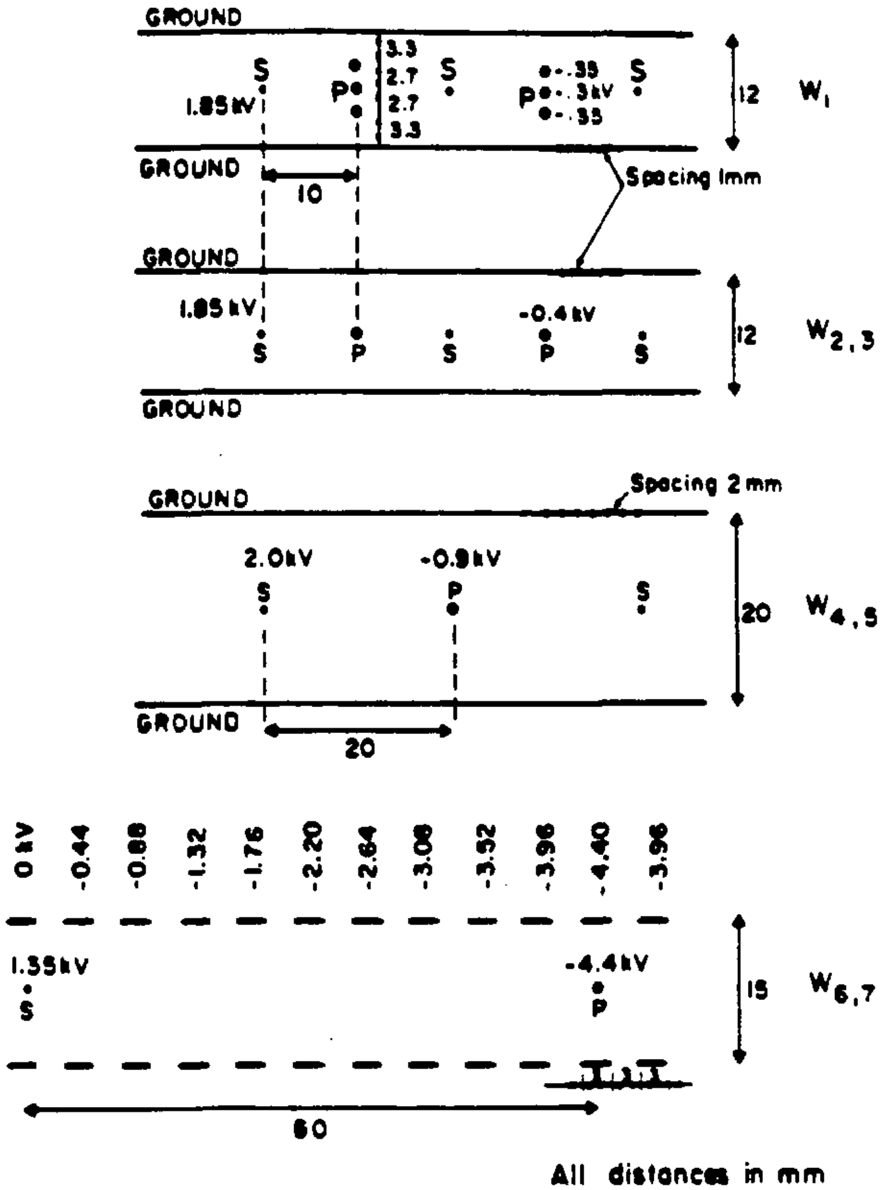

Figure 3.8: The drift cell structure

Each target in the upstream part has a thickness of $\simeq$20 gr$\times$cm^{-2} , the double of the thickness of a target in the downstream part; this because we want to have a part of the setup where the hadron secondary interactions are minimized [Table 3.2]. To have a comparable volume occupied by targets of different materials, the carbon and calcium targets are splitted into smaller units. Each target is surrounded by a capton foil and hanged on a movable frame .

Table 3.1: Main parameters of the chambers

Wire chamber	Sensitive area $x \times y$ (m^2)	Plane structure	Wire or drift space (mm)	Drift velocity (mm/nsec)	Anode–cathode gap (mm)
PV1 PV2	1.3 × 0.8 2.8 × 1.0	$x,\theta^{1+},\theta^{2+},\theta^{2-}\theta^{1-},x$ $x,\theta^{1+},\theta^{2+},\theta^{2-}\theta^{1-},x$ $\theta^{1\pm} = \pm 45°/y$ $\theta^{2\pm} = \pm 18°/y$	4 2	—	
P1 P2 P3	0.8 × 1.8 0.8 × 1.8 0.8 × 1.8	x,y,θ θ,y,x θ,y,x $\theta = 20°/y$	2	—	8
W1 W2	1.2 × 2.2 1.2 × 2.2	$\theta^{-\prime},y',\theta^{+\prime},x',\theta^{-},y,\theta^{+},x$ $x,\theta^{-},y,\theta^{+},\theta^{-\prime},y',\theta^{+\prime},x'$ $\theta^{\pm} = \pm 30°/y$	10	0.053	6
P45	Ø 0.9	$y\theta^{+},y\theta^{-},y\theta^{+},y\theta^{+}$ $\theta = \pm 30°/y$	2	—	8
W4 W5	2.6 × 5.3 2.6 × 5.3	$y,y',x',x,\theta,\theta',y',y$ $x,x',\theta,\theta',y,y',x',x$ $\theta = -30°/y$	20	0.050	10
W6A W6B W6C W7A W7B W7C	3.48 × 2.88 3.48 × 2.88 3.48 × 2.88 4.32 × 3.48 4.32 × 3.48 4.32 × 3.48	x,y,θ,x',y',θ $x,y,\theta,x',y',x,y,\theta$ x,y,θ,x',y',θ x,y,x',y',θ $x,y,\theta,x',y',\theta,x'',y''$ x,y,x',y',θ $\theta = -60°/y$	60	0.051	7.5

Gas mixtures (%)

	Argon	Isobutane	Methane	Ethane	Freon	Methylal
PV1/2	70	24			0.8	4
P1/2/3	71.5	23.8			0.7	4.0
W1/2	81.5	1.5	17			
P45	78	20			2	
W4/5	77	2	21			
W6/7	65			35		

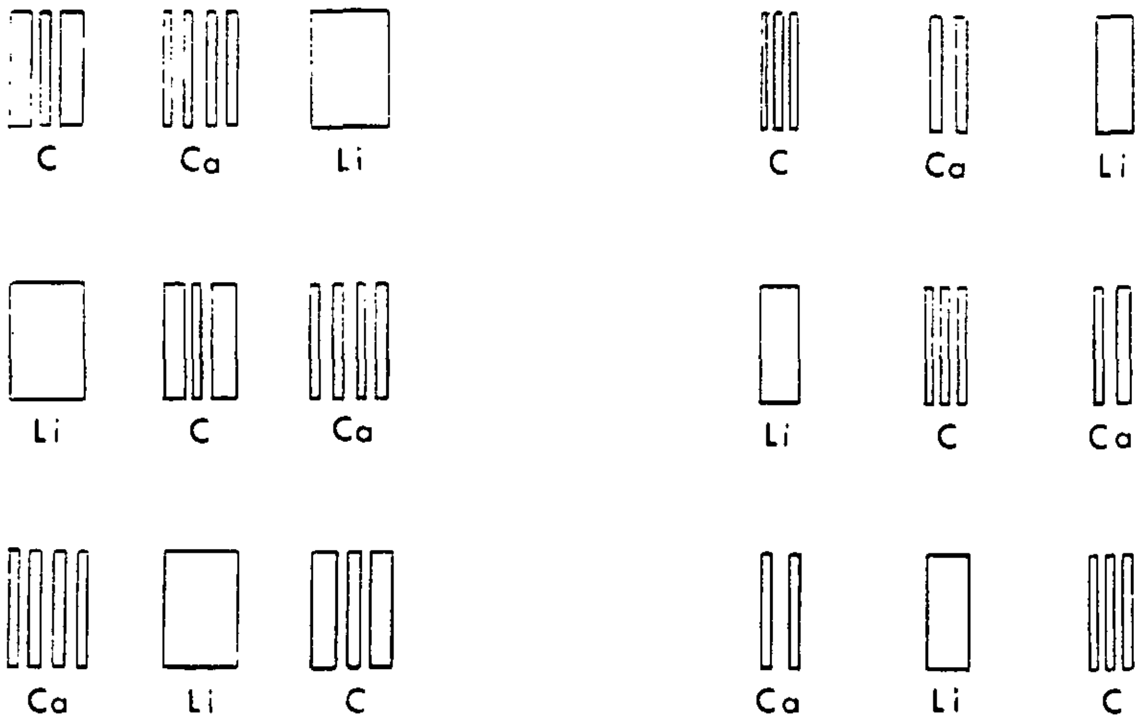

Figure 3.9: The complementary target setup. The beam enters from the left ; the length of the upstream part of the setup is $\simeq$2 m, the same is for the downstrem part whereas the total length is $\simeq$6 m. The chamber P_0B is sitting between the upstream and downstream part .

Table 3.2: The thickness of the targets (in gr×cm^{-2})

Li	C	Ca
18.541	18.659	20.688
9.266	11.210	10.373
18.509	18.633	20.646
9.275	11.220	10.283
18.528	18.663	20.643
9.271	11.176	10.200

Chapter 4

TRIGGERS AND DATA ACQUISITION

4.1 The triggers

The trigger system informs the data acquisition computer that an event has occured which requires data from some or all the detectors to be written on the magnetic tape. To start data acquisition a trigger pulse has to be sent to the trigger system . The trigger pulses are generated by predifined hardware conditions. I will now give some details of the different triggers used in our experiment.

4.1.1 T_1

T_1 is one of the physics triggers of the experiment. The hardware requirements on the scattered μ are imposed with programable coincidence matrices [29]. The matrix patterns are determined by Monte Carlo simulation. The pulses from the hodoscopes H_1, H_3 and H_4 are fed through the chain of coincidence matrices shown in [Figure 4.1], each of which checks the correlation of the hit elements against the programmed pattern of allowed coincidences. If any of them is fulfilled, both the pulses of the corresponding elements and a global coincidence signal can be passed further down the chain.
A scattered μ must fulfill the following conditions : target pointing in both coordinates , scattering angle larger than a preselected value , no hits outside the beam hole in the veto wall , special angle cut for the high ν region . The definition of the trigger is the following :

$$T_1 = \Sigma\overline{V}\times(H_3H\times H_1H\times H_4H)\times(H_1V\times H_3V)\times(H_1V\times H_3H)\times(H_3V\times H_3H)$$

In terms of matrices it may be written as :

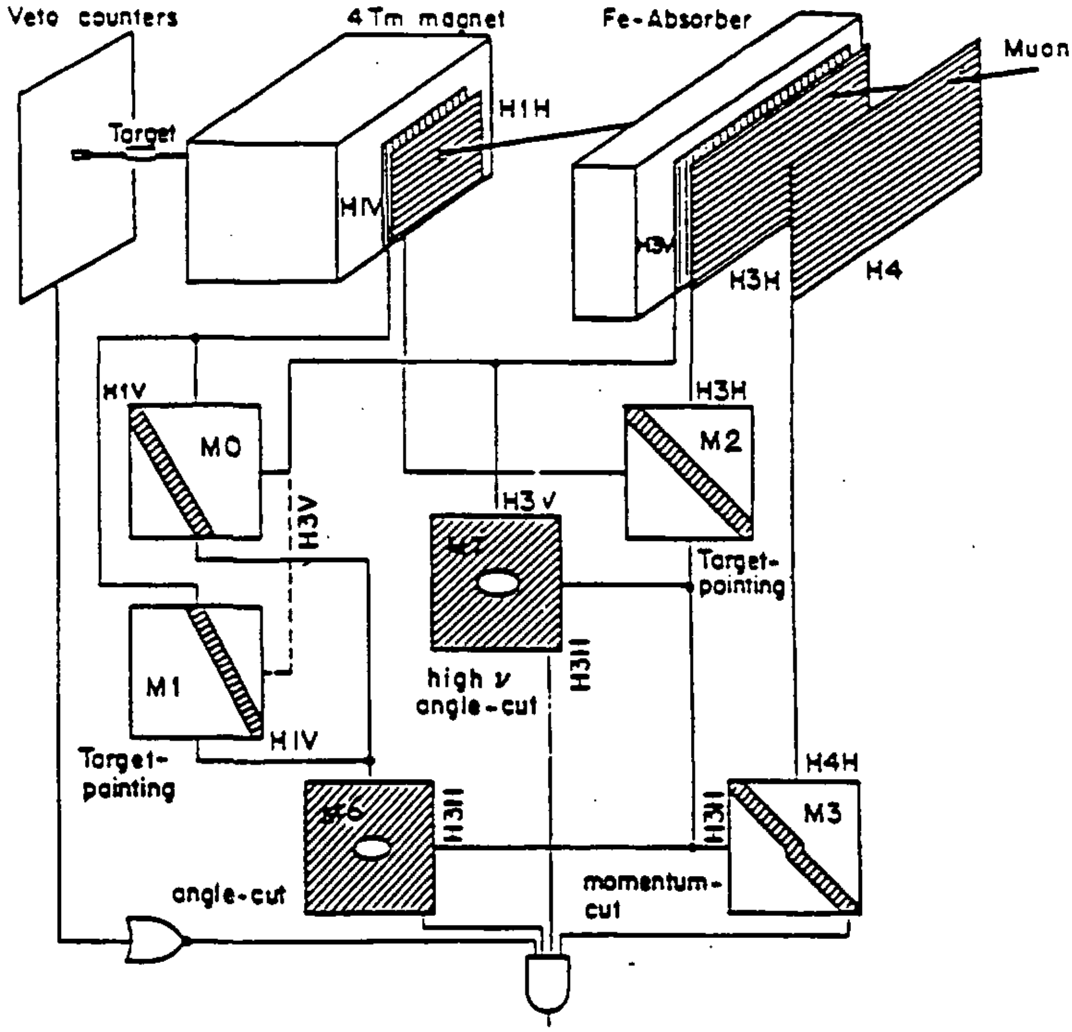

Figure 4.1: T$_1$ logic

$$T_1 = \Sigma\overline{V}\times(M_2\times M_3)\times(M_0\times M_1)\times M_6\times M_7$$

The conditions $(M_2\times M_3)$ and $(M_0\times M_1)$ select muons pointing to the target in the vertical and in the horizontal plane respectively. The matrix M_6 defines a minimum angle cut, whereas M_7 provides an additional angle cut. Its purpose is to avoid high ν events where the muon passes through the hole of H_1 and where the trigger is satisfied in H_1 by other particles produced in the same interaction. These bad triggers are rejected in M_7 by excluding part of the region in H_3 through which these muons pass . The plane H_3V is used to give the time of the trigger . With a beam intensity of $\simeq 10^7$ μ/s at the energy of 90 GeV we had $\simeq$ 50 T_1/s.

4.1.2 T$_2$

T_2 was introduced to cover the small Q^2 region not seen by T_1. In our data the mean Q^2 of the accepted T_2 events is 0.75 and 1.1 $(GeV/c^2)^2$ for the upstream and downstream part of the setup respectively, whereas , for T_1, it is

3.4 and 4.5 $(GeV/c^2)^2$. Because of the short length of the hodoscopes strips, T_2 doesn't see the high ν events, so the small x region covered by T_1 and T_2 is almost the same. T_2 looks only at the angle in the vertical projection, where there is no distorsion produced by the magnetic field. It has the disadvantage of having no kinematical region with 100% acceptance.

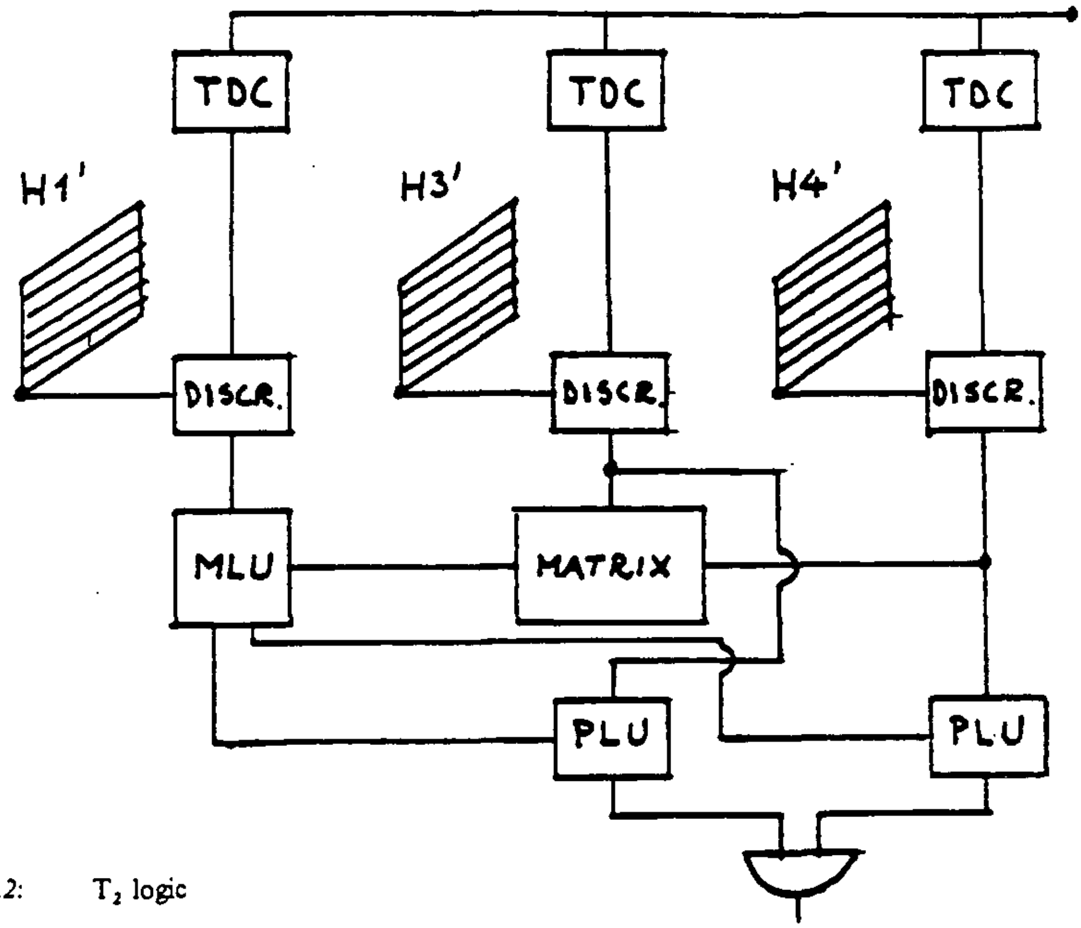

Figure 4.2: T_2 logic

The definition of T_2 [Figure 4.2] is :

$$T_2 = \Sigma \bar{V} \times H_1' \times (H_3' \times H_4')$$

where the second and third conditions give the angle cut and the target pointing. A programable logic unit (PLU) and a memory lookup table (MLU) are equivalent to a matrix. H_3' gives the time to the trigger. T_2 data are usually compared with the T_1 data taken with lower energy, which have almost the same Q^2 distribution. With a 90 GeV beam T_2 doesn't have any lower energy T_1 to be compared with, and it covers a very low Q^2 region, therefore it was strongly prescaled to a rate of $\simeq$ 10 triggers/s.

4.1.3 T_5 : the beam trigger

It is defined as :

$$T_5 = H5A \times H5B$$

and it monitors on-line the beam hodoscopes and the P_0 chambers. During the data analysis it is used to align the beam hodoscopes and the P_0 relative to each other.

4.1.4 T_6 : the alignment trigger

It is a special trigger enabled only during dedicated alignment runs, and it is defined as :

$$T_6 = \Sigma V2 \times H_3 9 \times H_1 Hcentre$$

where H_1Hcentre means the central strips of H_1H. It uses a deflected muon beam which passes through the P_0 chambers and the edges of the big chambers. T_6 is used to align the beam chambers relative to the larger chambers.

4.1.5 T_7: the near halo trigger

It is defined as :

$$T_7 = H_3 H \times H_4 Hcentre \times H_3 Vcentre \times \Sigma V3centre$$

and it is used to monitor and align the chambers P_{123} and P_{45} in the region close to the beam.

4.1.6 T_8 : the far halo trigger

Its definition is

$$T_8 = \overline{T_7} \times H_3 H \times H_4 H \times \Sigma H_3 Vcentre$$

It is used to monitor and align, together with T_7, the large chambers (W_{12}, W_{45}, W_{67}).

4.1.7 T_9

It is produced by a 10 MHz clock and used for background studies. When there is no beam monitoring tasks run on T_9.

4.1.8 T_{11} : the halo trigger

T_{11} is used to monitor the drift chambers and to calculate the trigger hodoscopes efficiency. It is defined as :

$$T_{11} = (H_3H \times H_4H) \times \Sigma V3$$

4.1.9 The normalization triggers T_{34} and T_{10}

Triggers 3 and 4 provide a measurement of the beam flux with an accuracy of 1% within $1-2$ hours [30]. The incident muons are counted using the 16 central strips of the 20 strips in the subplanes BHA $-$ Z (T_3) and BHB $-$ Y (T_4). The maximum number of muons per strip per second is a few 10^6. Trigger 3 and 4 work in the same way, providing two independent measurements of the incident flux. It is possible to use one of the two for the normalization and to correct it for the counts missed but seen in the other trigger, i. e., the inefficiency of the hodoscopes plane can be corrected for. The signal from the discriminator of the beam hodoscope strip of the subplane is brought in anticoincidence with the halo veto, the computer and BMS busy levels, in the so called beam defining coincidence . The output of each of the coincidences goes to a scaler, B(i), to a beam defining TDC, and, prescaled, ORed with the other 15 channels, to the further prescaled sample trigger logic (T_3 or T_4). The prescaling before the OR is necessary to reduce the possibility of two coincident inputs to well under 1%. The output of each prescaler before the OR enters a pattern unit which allows the identification of the strip flashed for each trigger. The sum of the 16 scalers B(i) gives the first order incident beam, to which no dead time correction has to be applied because the beam is counted only when the data acquisition computer can accept triggers. To obtain the reconstructable beam we multiply the sum of the scalers counts by the probability of a count to correspond to an useful beam muon. This probability is determined by the beam sample trigger, which must give a sample representative in space and time of the counts of the scaler B(i), that is all strips should have the same prescaling factor and should be affected by the same dead time and no time bias should be introduced over the normalization period or over the beam spill profile. The same beam reconstruction logic applies to the sample trigger as well as to all the physics triggers. The reconstructed track is accepted only if its time and position are in agreement with the beam defining TDC and the pattern unit information.

Trigger 10 is another normalization trigger which allows a measurement of the flux with a statistical accuracy of 1% over about 2 weeks of data taking. The principle is the following : the muons of the beam are always recorded by the TDCs connected to the beam hodoscopes ; if we start these TDCs randomly we then obtain a collection of windows in the beam. The start of the beam hodoscopes TDCs ,called the T_{10} trigger, is given by the decay of an 8 Bq activity α source of Am^{241} (half life 432.2 y) sandwiched by two plastic scintillators viewed by one photomultiplier each. The source is located far away from the beam line in order to avoid any correlation between T_{10} and the beam. The width of the windows is 60 ns. Inside each of these windows we select during the analysis a smaller window of 20 ns centered on the physics trigger beam time : this because we want to have the same TDC dead time for T_{10} as for physics triggers. Everything inside the window is recorded because it is not possible to apply any hardware veto : there is no time relation between T_{10} and beam tracks,i. e., the time distribution of the tracks in the window is flat. All the veto levels within the window are recorded and the veto is applied during the software analysis. We reconstruct the T_{10} tracks applying the same cuts as for the physics triggers and we obtain the reconstructable beam flux from the following expression :

$$\Xi = \frac{\Xi_{10}}{\Delta w \times v}$$

where Ξ_{10} is the sum of the reconstructed beam tracks inside the window, Δw is its width and ν is the decay rate of the source. Ξ is the effective beam flux in the period during which we have collected the beam in Ξ_{10}. The 320 TDC's channels are continuously calibrated : there are two 200 ms regions, before and after the muon spill, during which data acquisition is active and the only trigger which is enabled is T_{10}. In this time the TDCs are started by T_{10} and stopped not by a muon but by a 10 Mhz clock. The fraction of stops which fall in a range of the TDC scale gives the fraction of 100 ns represented by this range. The rate of the source, ν , is obtained from a scaler gated by spill, this means that the dead time produced by the other triggers and by T_{10} itself is automatically taken into account in the expression which gives the reconstructable flux. The reason why this trigger was introduced at the beginning of the EMC experiment [31] was to foresee beam intensity so high ($10^8 - 10^9\ \mu/s$) that no beam condition could be set in the physics triggers.

All triggers are prescaled, except T_1 and T_{10} (prescaling T_{10} would destroy its randomness). This way the data acquisition computer is not blinded by the triggers and the dead time is reasonable (30%).

4.2 The data acquisition

The readout and the monitoring of the apparatus are performed by a system of four PDP 11/70 computers, labelled DAC, U0, U1, U2, interconnected using a small PDP 11/10 computer (MPX) which acts as a multiplexer and an interface to the Cern network. The data transfer from the readout electronics of each detector to the data acquisition computer (DAC) takes place using the Camac Romulus system [32]. A Romulus branch consists of a special branch driver (ROBD) and a set of special crate controllers (ROCC). Data are read in this way : a read signal is received by a branch driver and passed through each crate controller. Any controller with valid data inhibits the propagation of the read signal and transfers its data to the branch driver as a block terminated with a marker (the equipment block number) and a word count. It then passes the read signal down the chain. At the end the read signal is returned to the branch driver. The NMC readout tree has an up and a down branch.

During the spill DAC has accces to the complete Romulus tree, it acquires data and then writes the information to a magnetic tape. There is a readout limit of 4000 sixteen bits words/event because of the 16 kbyte event decoding buffer of the DAC, and up to 16 different triggers can be recorded and written to tape. Each trigger has its own selection of equipment to be read and the trigger rate is $\sim$ 100 triggers/s, which correspond to $\sim$ 0.6 Mbyte/s. Outside spill DAC distributes samples of complete events to the monitoring tasks which are running on the other three computers, except the tasks which check the structure of the event and sample every end of burst record which are running on DAC itself. Outside spill U0 has acces to the down branch and U1 and U2 to the up one in order to perform hardware checks via their local Camac. Each detector is controlled by at least one on-line monitoring task, which reports any hardware fault to the shift crew.

Chapter 5

THE SOFTWARE PRODUCTION CHAIN

Before being ready for the physics analysis, the data have to pass through a software chain whose outputs are the fully reconstructed events with all the necessary information and the normalization beam flux. Before starting the process one has to know the position and the calibration parameters of each detector in order to convert the electronic signal of the raw data into space and time coordinates. The geometric informations, obtained from different triggers, the straight beam trigger (T_5), the deflected beam trigger (T_6), the near (T_7) and far halo triggers (T_8), allow the alignement of the chambers and the hodoscopes. The position of each module is obtained with an accuracy of $\pm$ 1 mm in x and $\pm$ 0.1 mm in y and z . The time of the track is given by the mean time of the hits in H_3V (H_3' for T_2) and it is used to correlate hits and to determine the position of the track in the drift chambers. With the H_3V reference time the calibration constants of BMS and BHOD time (T_0) are established. All these parameters, together with drift velocities, non−linearities in the drift chambers, wires spacing and trigger matrices setting, are written in the alignement file created for each period of data. A final optimization is made using a sample of reconstructed tracks to tune the alignement parameters in an iterative process until the residuals, that is the distance between the recorded hit and the reconstructed track, are centered on zero for all the detectors. The modifications introduced at this level are usually smaller than 0.1 mm and in the final alignement file the position of each detector plane is determined with an accuracy of about one tenth of the resolution of the plane.

When the alignement file is produced one may start the reconstruction of the events with the filtering of the raw data tapes. The successive steps of the chain [Figure 5.1] are : a pattern recognition program to find tracks (Phoenix), a geometrical reconstruction program to fit the tracks and the vertex (Geometry), two programs (Snomux and Snomin) which process those detectors not considered so far and which compactify the information on the micro DST (data summary tapes) used for the physics analysis.

5.1 Phoenix

The first task of Phoenix is to find the beam tracks which may have produced the interaction. It searches for tracks in the beam momentum station and in the beam hodoscopes and it correlates them using their mean TDC time. All the beam tracks must be seen in the beam hodoscopes. About 90% of the events have at least one correlated track in the BMS and in the BHOD, those events where a track cannot be found are rejected.

Then Phoenix has to look for the scattered muon and, if it exists, to reconstruct it. The reconstruction starts in the drift chambers W_{67} behind the absorber. Lines which are found in both the central and the side chambers of W_{67} are merged into a single line. If no candidate track is found in W_{67} the event is discarded. Else the hits in the trigger hodoscopes, together with the target position , are used to obtain a first approximation of the muon track. From W_{67} the track is extrapolated back through the absorber to look for associated lines in W_{45} or P_{45}. If a track is found consistent with the extrapolation from W_{67}, the track is refitted and projected to $W_{12}-P_0E$, where the process is repeated. At this point we have candidate tracks downstream the FSM, and hits must be found upstream and inside the magnet. The amount of bending in the $x-z$ plane is negligible , so the $W_{12}-W_{45}-W_{67}$ lines are first extrapolated in the z projection as straight lines to P_{123}. If consistent hits are found, the knowledge of the FSM field is used to search for hits in the y coordinate. Once the hits have been found the track is refitted and projected upstream to search for hits in the chambers PV_1, PV_2, P_0C and P_0B. Lines are then refitted using the hits in these chambers . At any stage in the reconstruction the tracks which cannot be associated with a minimum number of hits in one of the chamber are rejected, unless they could have passed through a dead region of the chamber. Once the reconstruction of the scattered muon is completed, the same procedure is applied starting from W_{45} to find and to reconstruct the hadrons. Both the raw data and the reconstructed events are written to tapes.

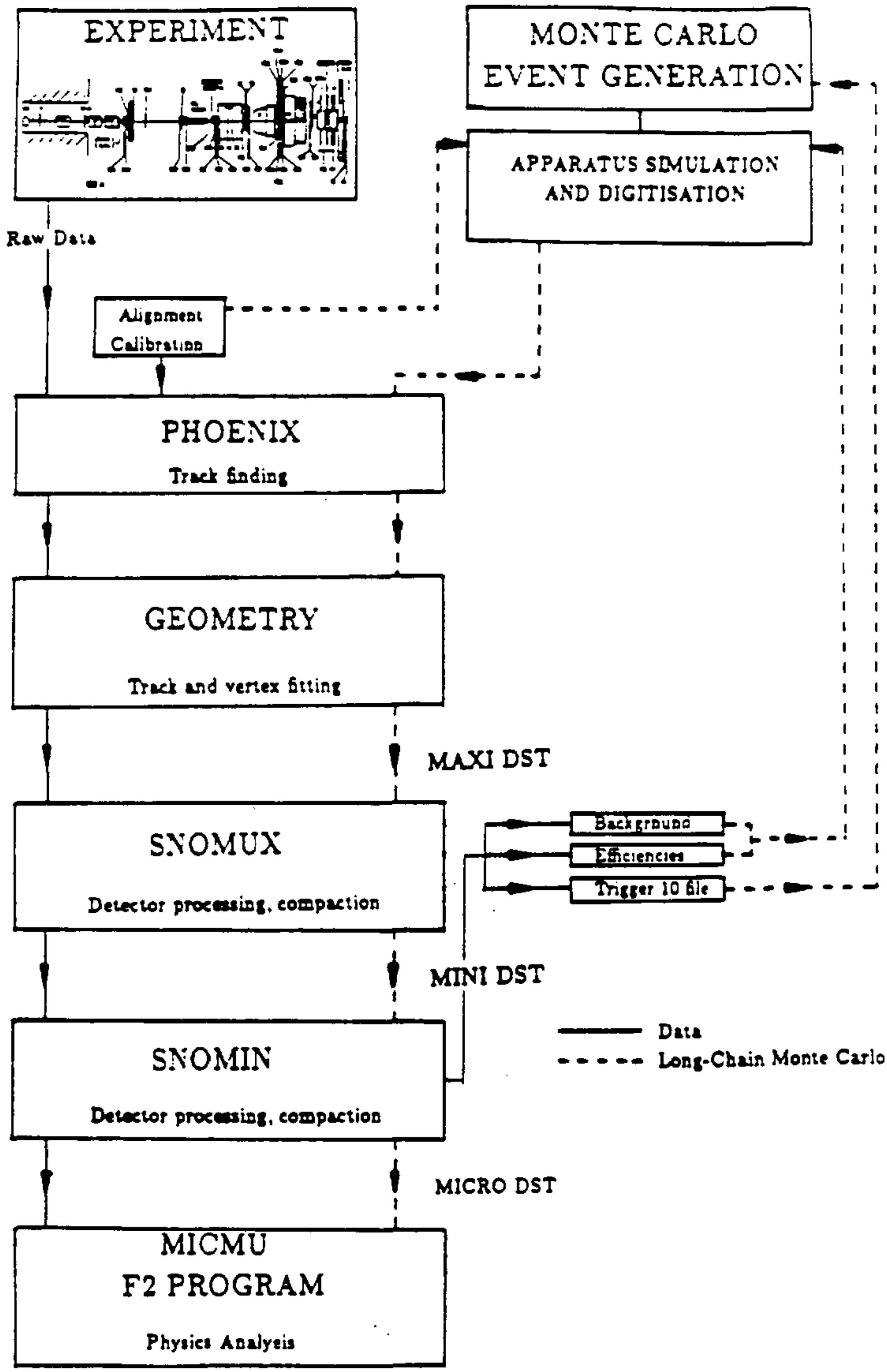

Figure 5.1: The NMC software production chain

5.2 Geometry

It fits the tracks found by Phoenix and associates them with vertices. It starts with the reconstruction of the beam muon track in the beam hodoscopes. Pairs of tracks too close in time or space are rejected to avoid confusion with knock−on electrons or because they would be ambiguous in the vertex identification. If there is more than one beam track left, the best one is selected, finding the track which gives the best χ^2 with the fastest scattered muon satisfying the trigger. Then the program fits in each detector the set of hits associated to each track by Phoenix and then it fits forward tracks from P_0B to W_{45} removing the bad hits on the track and giving the value of the momentum. Lines in W_{67} are fitted and muons defined by linking the $W_{67}-W_{45}$ lines, taking into account the multiple scattering in the absorber. The mean probability of the track fit χ^2 for the fully reconstructed μ is about 0.41. The trigger hodoscope elements traversed by the fastest muon are checked against the trigger matrices to remove fake trigger events.

The last step is the vertex fitting. Vertices are defined to be the position of closest approach for a set of tracks. The primary vertex is found from the intersection of the beam track and the fastest outgoing muon. If different tracks are coming out from the same vertex, they are added iteratively. If a satisfactory χ^2 probability is obtained then the track is associated and the position of the vertex is modified accordingly. This process stops when a stable vertex position is found and each remaining unassociated track fails the χ^2 test. Secondary vertices are then searched analysing any compatible pair of tracks. Different type of vertices are possible and they are classified in the following way

1. type 1 : beam and one same sign μ

2. type 2 : beam and more than one same sign μ

3. type 3 : type 1 plus hadrons associated (hadron is everything which is not a μ)

4. type 4 : two oppositely charged hadrons and no incoming track (V_0) , the event must be compatible with : $\gamma \rightarrow e\ e$, $K^0 \rightarrow \pi\ \pi$, $\Delta \rightarrow \pi\ p$ and the neutral particle must point back to the primary vertex

5. type 5 : beam and one oppositely charged μ

6. type 6 : charged hadron decay (V^{+-})

7. type 7 : secondary vertex with incoming track but not V^{+-} decay

8. type 8 : secondary vertex without incoming track but not V^0 decay

The output from geometry, that is fitted tracks and vertices, are written to the Maxi DST together with the raw data and used as input to Snomux.

5.3 Snomux

It is used to read the maxi DST and to process those detectors not involved in the reconstruction of the topology and the kinematic of the event. A scaler processor decodes all the scalers information from the start of burst and end of burst records. It writes a special files which contains the T_{10} rate/spill; this information is used to reject those bursts where T_{10} cannot be used because of problems in the electronics. A similar file is written for T_{34}. The output of Snomux is in the form of a condensed mini DST which no longer contains the raw data and the Phoenix information.

5.4 Snomin

It is used to read and to process the mini DST. It contains the H_2 processor which calculates for each track the amount of energy seen in electromagnetic and hadron modules of the calorimeter, performs pattern recognition and tries to cluster the hits in H_2 in order to estimate the energy of neutral showers. It includes the efficiency package to calculate the single wire and global efficiency for all planes of each detector, which will be used as input to the Monte Carlo. It writes in the background file all the hits not used in the reconstruction of the events. It tunes the veto TDC constants used to reconstruct the transitions of the veto level which has to be applied to T_{10} tracks and, as a check, also to the physics triggers. Reconstructed T_{10} tracks are written to a file used to produce the beam in the

Monte Carlo. It analyses the T_{34} beam tracks and attaches the proper weight to them. The definitive phase space cuts on the beam are set up in Snomin, and they are of course the same for the physics and the normalization triggers. All the necessary information of each event are finally written to the micro DST together with the reconstructed beam tracks and the corresponding factors for the normalization.

The number of triggers for the 90 GeV Ca/C/Li data after the different steps of the software chain are reported in [Table 5.1].

Table 5.1: Surviving T_1, T_2 and T_{10} in the 90 GeV Ca/C/Li data

Filter	**Phoenix**	**Geometry**	**Mini**
6691515	4521571	4483857	3483351
1317822	850209	842331	601308
808219	320703	319024	318182

5.5 The Monte Carlo

A complete simulation of the apparatus can be made for each period of data taking to investigate the modifications induced by the detector on the ' true ' physics. The input to the Monte Carlo is given by the same alignement file used for the reconstruction of the events, the T_{10} file with the beam tracks, the efficiency file and the background file. The values of Q^2 and ν are generated under a $1/Q^2$ distribution and a flat distribution in ν . To each generated events is given a weight which depends on the assumed F_2. After their generation the Monte Carlo events may pass through the reconstruction chain (long chain) or simply be read by Snomux and smeared under the experimental resolution obtained from the data (short chain). However, as explained in the target description, because of the complementary target setup we don't need to know the acceptance of the detector to measure the EMC effect, that is why the Monte Carlo is not used in this analysis.

Chapter 6

DATA ANALYSIS

The data analysed in this thesis were taken during two weeks in November 86 with a 90 GeV negative muon beam and targets made of Calcium, Carbon and Lithium. In that period the detector was working smoothly, as can be checked with the ratio between the physics trigger and the normalization trigger T_{10} as function of time: this ratio would show large non statistical fluctuations if there would have been hardware failures in the detector affecting the reconstruction of the scattered muon. The bad T_{10} bursts have already been removed before writing the micro DST and the beam reconstructed in T_{10} experienced the same requirements as the beam which produced physics triggers. On the basis of this analysis I rejected only two runs, for which serious hardware failures were reported about the matrices and the chamber P_{45}. The total final sample consists of 180 runs. In this chapter I will discuss the way to extract deep inelastic events from the data and how to obtain the cross sections ratios and their errors.

6.1 The radiative corrections

The process we are interested in is the one photon exchange, whereas the measured cross section includes the contribution of many other diagrams [Figure 6.1].

This contribution must be evaluated and removed from the total cross section. It is mainly coming from vertex corrections produced by the emission and reabsorption of virtual particles and from the radiative tail. We define as belonging to the radiative tail those events in which a real high energy photon has been radiated by the muon. Three different types of processes enter the radiative tail : deep inelastic, coherent elastic and quasi elastic. In the deep inelastic tail the nucleon is

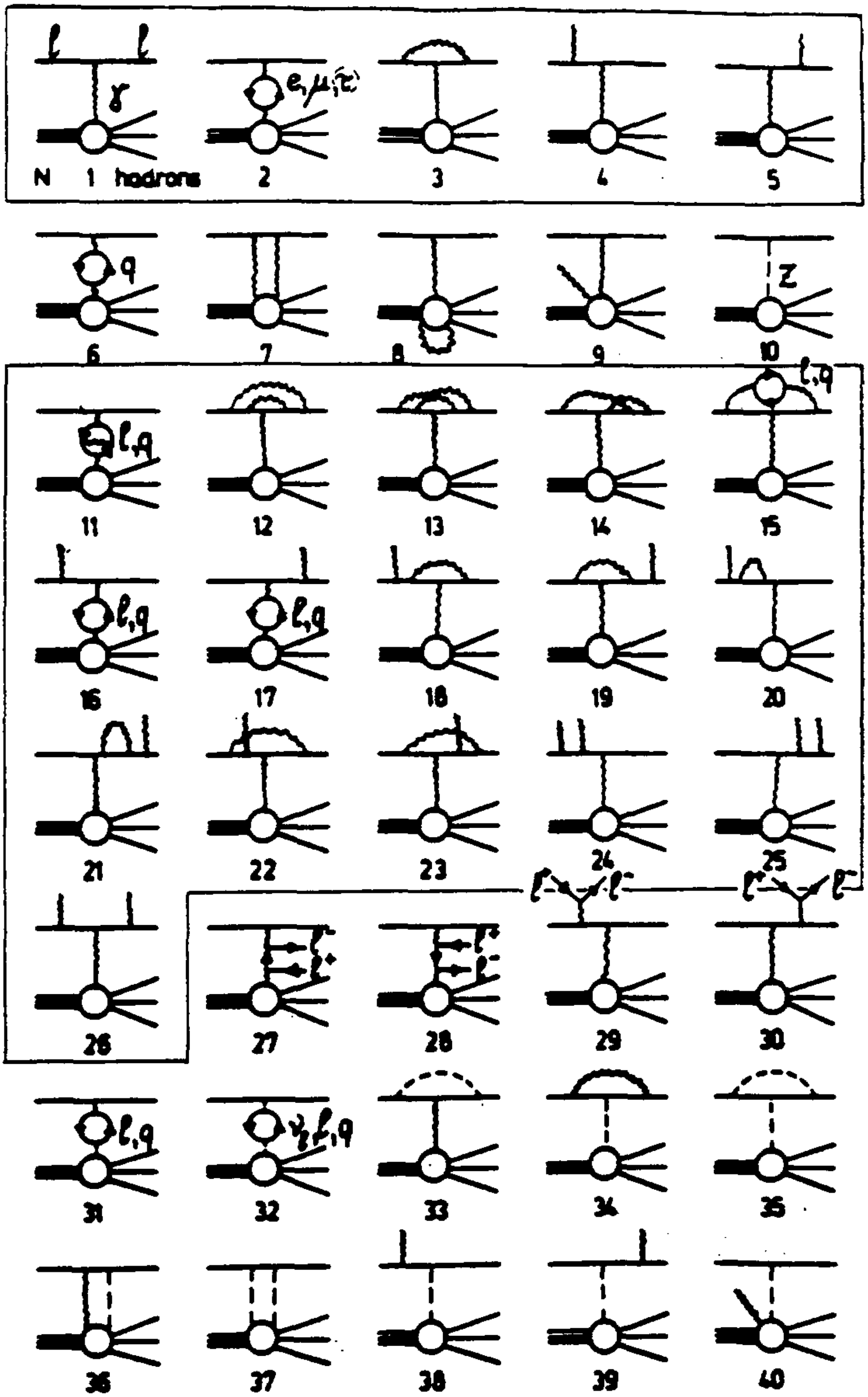

Figure 6.1: diagrams which contribute to the measured cross section. The diagrams implemented in the NMC program are enclosed by a full line

broken but only a fraction of the energy lost by the muon, which is what we measure, is transferred to the struck quark; in this case we have to move the events to a smaller ν bin. In the coherent elastic and quasi elastic tail the measured energy loss is almost entirely taken by the real radiated photon and we have elastic scattering on the whole nucleus (coherent elastic) or on a nucleon (quasi elastic). These events are not deep inelastic, the nucleon is not broken and they must be removed from the sample. The coherent tail is the contribution which is most dependent on the target material because its cross section is proportional to Z^2. I apply the radiative corrections using the standard EMC program: to each event is given a weight η which is its probability of being a deep inelastic scattering : $\eta = \frac{\sigma_{1\gamma}}{\sigma_{rad}}$ where $\sigma_{1\gamma}$ and σ_{rad} are the calculated values of the deep inelastic and of the total cross section respectively. The single photon emission formula of Mo and Tsai [33] is used, the effect of multi photon emission and of radiation from the recoiling target are neglected. The validity of this approach was confirmed by the EMC [34], which measured the energy and the angular distribution of hard radiated photons with a fine grained lead glass calorimeter. The reliability of the program was checked [35] comparing the results of the EMC and NA4 programs; both methods agree within about 1%, except in the high x, high y region where the difference of $\sim$ 3%, is due to the weak electromagnetic interference neglected in the EMC program. The program has to be fed, for each target material, with the nuclear form factor, to calculate the coherent elastic tail, and with the structure function, to calculate the inelastic tail and $\sigma_{1\gamma}$. Nuclear form factors are taken from the experiments which measure the nuclear charge distribution in elastic electron scattering [36], [37], [38]. Since we don't have yet any absolute F_2 published by our collaboration, I take $F_2^{D_2}$ and the ratio $\frac{F_2^C}{F_2^{D_2}}$ from a fit to the world data [39] and I build F_2 in the following way :

$$F_2^{Li} = \left(\frac{F_2^{Li}}{F_2^C}\right) \cdot \left(\frac{F_2^C}{F_2^{D_2}}\right) \cdot F_2^{D_2}$$

$$F_2^C = \left(\frac{F_2^C}{F_2^{D_2}}\right) \cdot F_2^{D_2}$$

$$F_2^{Ca} = \left(\frac{F_2^{Ca}}{F_2^{C}}\right) \cdot \left(\frac{F_2^{C}}{F_2^{D_2}}\right) \cdot F_2^{D_2}$$

The corrected ratios $\left(\frac{F_2^{Li}}{F_2^{C}}\right)$ and $\left(\frac{F_2^{Ca}}{F_2^{C}}\right)$ are the quantities to be estimated. Starting with guess values for these ratios, the program of radiative corrections is run iteratively untill the corrected ratios are stable to within 0.1%. The convergence is reached after two iterations only. I will discuss the size of the radiative corrections and the related errors in a further paragraph.

6.2 The geometrical method

The target setup consists of 3 rows of 6 targets each. A row stays in the beam for ~ half an hour and then it is replaced by a parallel one. This way it is possible to obtain the cross sections ratio from the complete setup, or only from the upstream part, i.e., the first 3 columns, or from the downstream part, i.e. the remaining three columns, without using the acceptance and the beam flux. In each (x, Q^2) bin the number of events coming from the target of material 'a', i.e., Calcium, Carbon or Lithium, in the position i (i = 1,..6) is :

$$N_i^a(x,Q^2) \propto \frac{\partial^2 \sigma^a(x,Q^2)}{\partial x \partial Q^2} A_i(x,Q^2) \Phi_i \zeta_i^a \Delta x \Delta Q^2$$

where $\frac{\partial^2 \sigma^a(x,Q^2)}{\partial x \partial Q^2}$ is the cross section of the material ' a ', which we assume to be constant over the bin, $A_i^a(x,Q^2)$ is the acceptance, ζ_i^a is the thickness of the target and Φ_i is the beam flux through it. Now we make the following assumptions:

1. all the 6 targets which are in the same row are hit by the same number of muons; this is true because the beam defined by the veto walls is completely contained in each target and it was checked looking at the vertex distribution of the events and at the effect of a software radial cut.

2. all the 3 targets which are in the same column have the same acceptance. It is worth while to make two comments on this point : the acceptance

may depend on the time, therefore it might be different for different targets just because they are in the same position at different times. What we really need is that the acceptance integrated over the period in which the data were taken is the same for the three targets, and this was obtained by frequently changing the row of targets in the beam and confirmed in the analysis by the absence of significant differences between the cross sections ratios given by subsamples of the data. The second comment is that Calcium, Carbon and Lithium have different radiation length, the multiple scattering is different, therefore the vertex reconstruction probability might not be the same. The comparison of the ratios obtained from the downstream and the upstream target setup, where the effect should be enhanced by the larger thickness and the smaller scattering angle, indicates that the hypothesis is justified and proves that the segmented complementary target averages out the multiple scattering effects.

With the discussed assumptions and using the complete setup we find that the cross sections ratio r and its statistical error between two materials 'a' and 'b' are

$$r(x,Q^2)=\left[\frac{\prod_{i=1}^{6} N_i^a(x,Q^2)\chi_i^b}{\prod_{i=1}^{6} N_i^b(x,Q^2)\chi_i^a}\right]^{\frac{1}{6}}$$

$$\sigma_r=\frac{r}{6}\sqrt{\sum_{i=1}^{6}\frac{1}{N_i^a}+\frac{1}{N_i^b}}$$

With the upstream or downnstream targets only we have :

$$r_{par}(x,Q^2)=\left[\frac{\prod_{i=1}^{3} N_i^a(x,Q^2)\chi_i^b}{\prod_{i=1}^{3} N_i^b(x,Q^2)\chi_i^a}\right]^{\frac{1}{3}}$$

$$\sigma_{r_{par}} = \frac{r_{par}}{3} \sqrt{ \sum_{i=1}^{3} \frac{1}{N_i^a} + \frac{1}{N_i^b} }$$

This way we have the ratio in each (x , Q^2) bin. To obtain it only as function of x we simply take the weighted average over the different Q^2 bins which are in the same x bin. We then plot the ratio in the mean center of the bin. If we collect all the events from each target which enter the same x bin, regardless of their Q^2, and then we make the ratio, the result doesn't change significatively. This already shows that the Q^2 dependence of the cross sections cannot be very different for the various materials we have.

The estimator of the ratio r is not linear in the measured statistical variables, therefore the observed value estimates the quantity r only up to a bias b. Its statistical relevance was investigated with a Monte Carlo [40]. It has been shown that the bias is negligible compared to the statistical error for populations with at least 50 events, as it is the case here. The experimental smearing of x may finally be responsible for a bias on the ratios, but, below $x=0.4$, the resolution on x is so small compared to the bin width that this effect is negligible.

6.3 The target thickness

The target thicknesses are given in Table 3.2. For the Carbon targets these values are directly used to calculate r, whereas for the Calcium and Lithium targets the contributions due to the capton foils at the edges and due to the oxidation have to be corrected for. For Calcium there is a further contribution due to the glue with which the faces were coated. Each capton foil has a thickness of 0.0186 gr/cm^2 and the increase due to the glue is of the order of 0.2%. The problem of oxidation is more delicate. Each target was weighed before and after the data taking; the interval between the two measurements was 50 days for Calcium and 60 days for Lithium. The oxidation was uniform on the whole surface of the Lithium targets. For the Calcium targets, whose lateral surface had already been oxidized before, it took place only on the two faces. The material added on the lateral surface is irrelevant, because the beam passes through the target and doesn't see it. I assumed a linear dependence on time of the oxidation and for each target I added a thickness increase which corresponds to the thickness of the oxide in the day which is in the middle of the data taking. The value of the thickness increase due to the oxidation and the final thickness I used for each Calcium and Lithium target are given in Table 6.1.

Table 6.1: the thickness increase and the used thickness (in gr/cm^2)

Ca $\Delta\zeta$	Ca ζ	Li $\Delta\zeta$	Li ζ
0.096	20.854	0.076	18.692
0.079	10.503	0.024	9.327
0.093	20.825	0.067	18.651
0.068	10.412	0.085	9.398
0.094	20.826	0.042	18.643
0.074	10.339	0.016	9.324

6.4 The cuts on the data

I will analyze the T_1 events, among which I take only those which satisfy the following requirements :

1. the scattering angle θ has to be greater than 14 mrad if the vertex is in the upstream targets and 17 mrad if the vertex is in the downstream targets. I take these values looking at the θ distribution of the events, from which I removed the steeply falling tail at low θ; I want thus to avoid the edges of the spectrum where the acceptance is very low, rapidly changing and probably strongly time dependent.

2. the momentum of the scattered muon is larger than 20 GeV/c, to remove muons coming from mesons decay, and ν is greater than 10 GeV, to avoid large smearing effect in the high x region.

3. the radiative corrections must be smaller than 30% for any target material. The error on the correction is roughly proportional to the size of the correction and we want to keep it reasonably small. This cut affects only the x region below 0.04. The reliability of the results after the 30% cut can be checked in the following way: we take, for instance, the events from Calcium and Lithium and we plot the ratio of their y distribution in each x bin. Without corrections there is a large enhancement in the high y region due to the radiative events, which are more in Calcium than in Lithium. We expect to remove this bump with the radiative corrections and to end up with a flat ratio, at least if we can exclude large differences in the Q^2 dependence of the cross sections. This is the case in the region where the corrections are smaller than 30%. The mean value of the radiative corrections as function of x for the accepted events is shown in Figure 6.2.

4. I take the point which is in the middle between two targets as the separation point and I apply a vertex cut to remove the events produced in the beam hodoscope in front of the targets and in the chamber P_0B located between the upstream and the downstream targets. The vertex resolution is excellent and the target identification very good.

The number of events surviving each cut is given in Table 6.2.

Table 6.2: the number of events after the cuts

Cut	**# events**
no cut	2938230
θ	2409262
P muon	2354600
ν	1722211
30% *r. c.*	1285256
vertex	1251846

The accepted sample consists of 441523 events from Calcium, 418860 from Carbon and 391463 from Lithium. These numbers reflect the different thickness and the different contribution of radiative events. The mean values of Q^2 and ν of the events after the cuts in the different bins are given in Table 6.3.

Table 6.3: the mean Q^2 (GeV/c^2)^2 and ν (GeV)

x	Q^2	ν
0.0125 – 0.02	1.40	38.33
0.02 – 0.04	2.02	35.94
0.04 – 0.06	2.72	29.58
0.06 – 0.10	3.38	23.33
0.10 – 0.15	4.60	20.17
0.15 – 0.20	6.12	18.98
0.20 – 0.30	8.15	18.13
0.30 – 0.40	11.05	17.28
0.40 – 0.60	14.35	16.50

6.5 The systematic errors

Two kinds of error are mainly affecting our data : a normalization error due to the target thickness and the uncertainty coming from the radiative corrections. The measured values of the target densities and their quoted errors are the following : $1.5197 \pm 0.0030 gr/cm^3$ for Calcium, $1.873 \pm 0.008 gr/cm^3$ for Carbon, and $0.461 \pm 0.002 gr/cm^3$ for Lithium. For the Calcium and Lithium targets I put an error on the thickness increase due to oxidation equal to half its value : this is meant to take into account the uncertainty about the time evolution of the effect and about its non uniformity over the surface. I add the errors for different target materials in quadrature and this leads to a final error on the normalization of about $\pm$ 0.4%.

I have estimated the error on the radiative corrections due to the uncertainties on the nuclear form factors, the input $F_2^{D_2}$, the ratio $\frac{F_2^C}{F_2^{D_2}}$, the suppression factor and the ratio between the longitudinal and transversal cross sections of the virtual photon.

1. the coefficients which parametrize the nuclear form factors were moved within the quoted errors and for each material I obtained a change in the ratio r of at most ~ 0.1% For Calcium and Carbon I also used the parametrization given by the so called Sum of Gaussian Method [41] and I obtained consistent results.

2. the input F_2 was moved by $\pm$ 5% with an effect on r of ~ 0.4%, 0.2% and 0.1% in the first three bins respectively. I studied the influence of a different parametrization given by a fit to a fraction only of the world data [39] and I saw shifts of at most ~ 1.7%, 0.64% and 0.14% in the first three points.

3. the ratio $\frac{F_2^C}{F_2^{D_2}}$ was replaced by the ratio $\frac{F_2^N}{F_2^{D_2}}$ [42] with a less steep increase in the large x region. The effect was at most ~ 0.1%.

4. the influence of $R = \frac{\sigma_l}{\sigma_t}$ was investigated looking at the different ratios obtained with $R = 0$ and $R = R_{QCD}$, with the parameters given by a fit to

the SLAC results [43]. The effect is of ~ 0.4%, 0.2% and 0.1% in the first three bins respectively.

5. a shift in r of ~ 0.2% and ~ 0.1% in the first two bins was seen to be produced by a 30% change of the Fermi momentum of the nucleon.

I always took the change produced on the ratio r as the estimation of the error and I added all these errors in quadrature. It is evident that the largest error is coming from the uncertainties on $F_2^{D_2}$. The effect is amplified in the elements with high atomic number: the large contribution due to the coherent tail, which doesn't depend on $F_2^{D_2}$, prevents a cancellation of $F_2^{D_2}$ in the ratio $\frac{\sigma_{1\gamma}}{\sigma_{rad}}$.

The effect due to a measurement of the transferred energy wrong by ± 1% was investigated and found to be at most ~ 0.8% in the high x bins. . The influence of a change of the cuts is never significant except for the cut wich remove the region where the radiative corrections are greater than 30%. A different cut, 40%, produces shifts in the ratio of the order of the quoted systematic error: this shows that the radiative corrections we are using are not perfect and can no longer be trusted when they exceed 30%.

6.6 The results

The cross sections ratios Ca/Li, C/Li and Ca/C are shown in Figure 6.3, Figure 6.4 and Figure 6.5 whereas their values with the statistic and systematic errors are written in Table 6.4, Table 6.5 and Table 6.6. If $R=\frac{\sigma_l}{\sigma_t}$ doesn't depend on the atomic number A, then the ratio of the cross sections is equivalent to the ratio of the structure functions F_2.
The comparisons between the ratios r_{par} obtained from the upstream and the downstream part of the target setup are shown in Figure 6.6, Figure 6.7, Figure 6.8. No inconsistence is evident and this confirms that the assumptions of the method used to extract the cross sections ratios are reasonably correct. To my mind the following conclusions can be drawn from the results :

Table 6.4: the ratio Ca/Li

x	r	st. err.	syst. err.	tot. err.
0.018	0.9088	0.0182	0.0202	0.0271
0.030	0.9585	0.0061	0.0094	0.0112
0.050	0.9870	0.0066	0.0047	0.0081
0.078	1.0128	0.0056	0.0042	0.0070
0.122	1.0209	0.0064	0.0042	0.0077
0.172	1.0200	0.0091	0.0042	0.0100
0.240	1.0242	0.0100	0.0042	0.0109
0.341	0.9880	0.0173	0.0078	0.0189
0.466	0.9601	0.0253	0.0076	0.0264

Table 6.5: the ratio C/Li

x	r	st. err.	syst. err.	tot. err.
0.018	0.9923	0.0192	0.0079	0.0157
0.030	0.9875	0.0062	0.0051	0.0080
0.050	1.0117	0.0067	0.0043	0.0079
0.078	1.0169	0.0056	0.0042	0.0070
0.122	1.0160	0.0064	0.0042	0.0076
0.172	1.0160	0.0090	0.0042	0.0100
0.240	1.0307	0.0101	0.0043	0.0109
0.341	1.0113	0.0176	0.0042	0.0181
0.465	0.9959	0.0261	0.0048	0.0265

Table 6.6: the ratio Ca/C

x	r	st. err.	syst. err.	tot. err.
0.018	0.9159	0.0176	0.0169	0.0244
0.030	0.9708	0.0060	0.0075	0.0096
0.050	0.9750	0.0063	0.0042	0.0075
0.078	0.9961	0.0053	0.0041	0.0067
0.122	1.0048	0.0061	0.0041	0.0074
0.172	1.0031	0.0086	0.0041	0.0096
0.240	0.9919	0.0094	0.0041	0.0122
0.341	0.9734	0.0165	0.0051	0.0173
0.466	0.9614	0.0247	0.0085	0.0261

1. there is a clear shadowing in Ca/Li and Ca/C and an indication of shadowing in C/Li. If we compare Ca/Li and C/Li we see that the point where shadowing starts increases with the atomic number.

2. antishadowing is clearly seen in Ca/Li and C/Li. There is however only little evidence of antishadowing in Ca/C.

3. in the high x region, which is not the region we want to investigate with these data, the shape of the EMC effect is visible in Ca/Li and Ca/C.

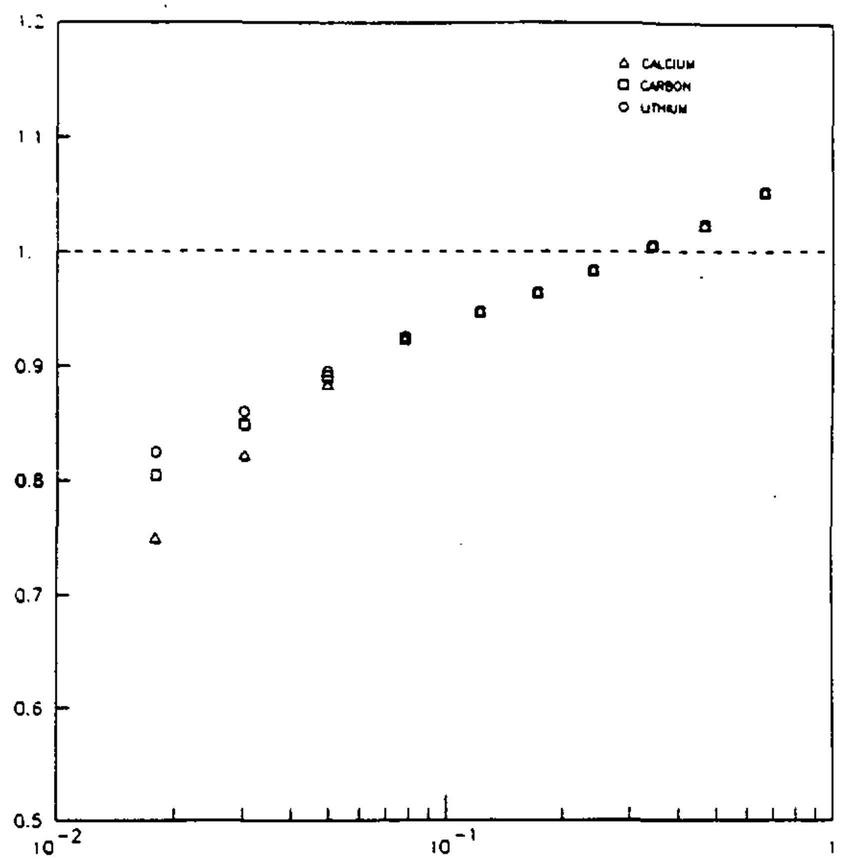

Figure 6.2: size of the radiative corrections on T_1

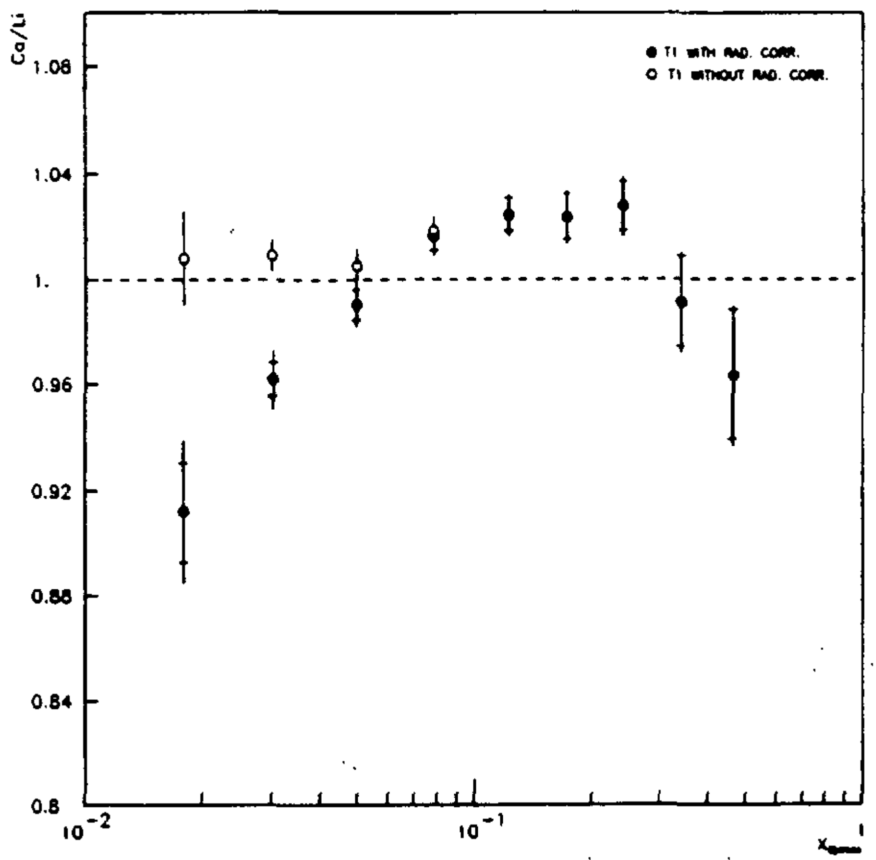

Figure 6.3: The ratio Ca/Li, the errors shown on the corrected ratio are the total errors, obtained by adding the statistical and systematic errors in quadrature. The extent of the statistical errors is shown by the inner bars.

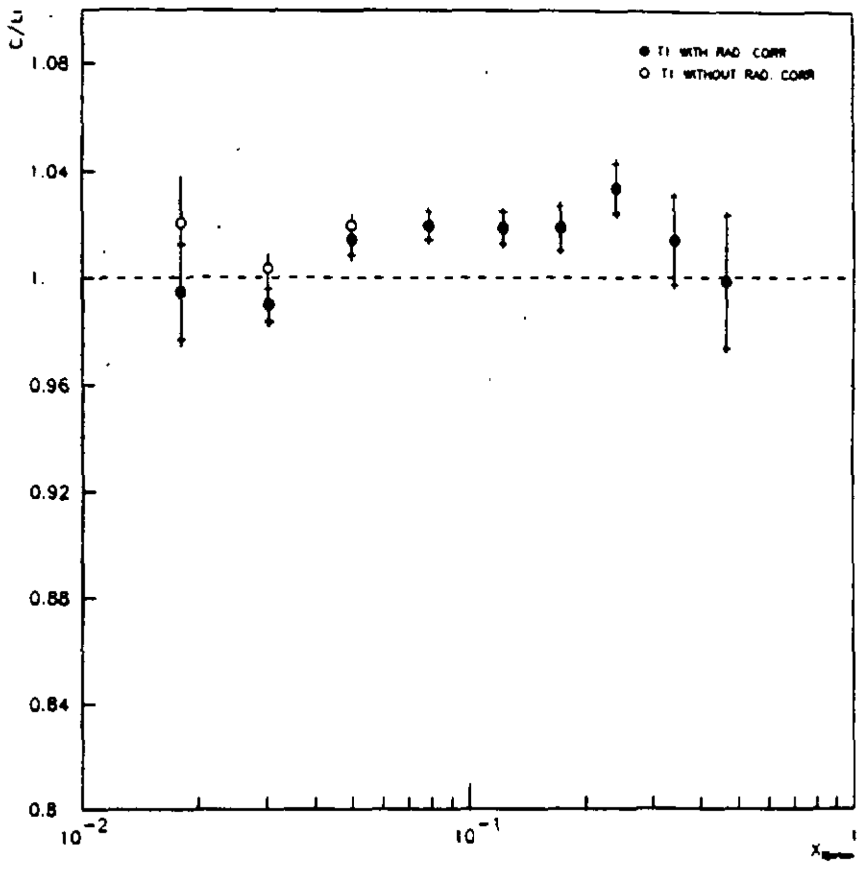

Figure 6.4: The ratio C/Li

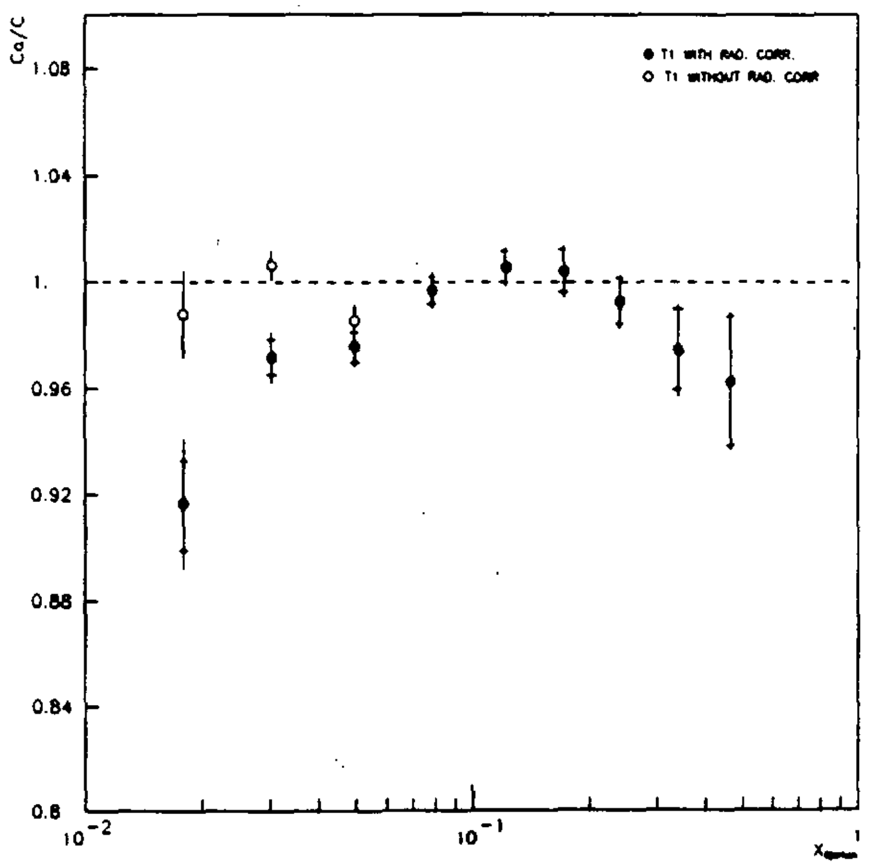

Figure 6.5: The ratio Ca/C

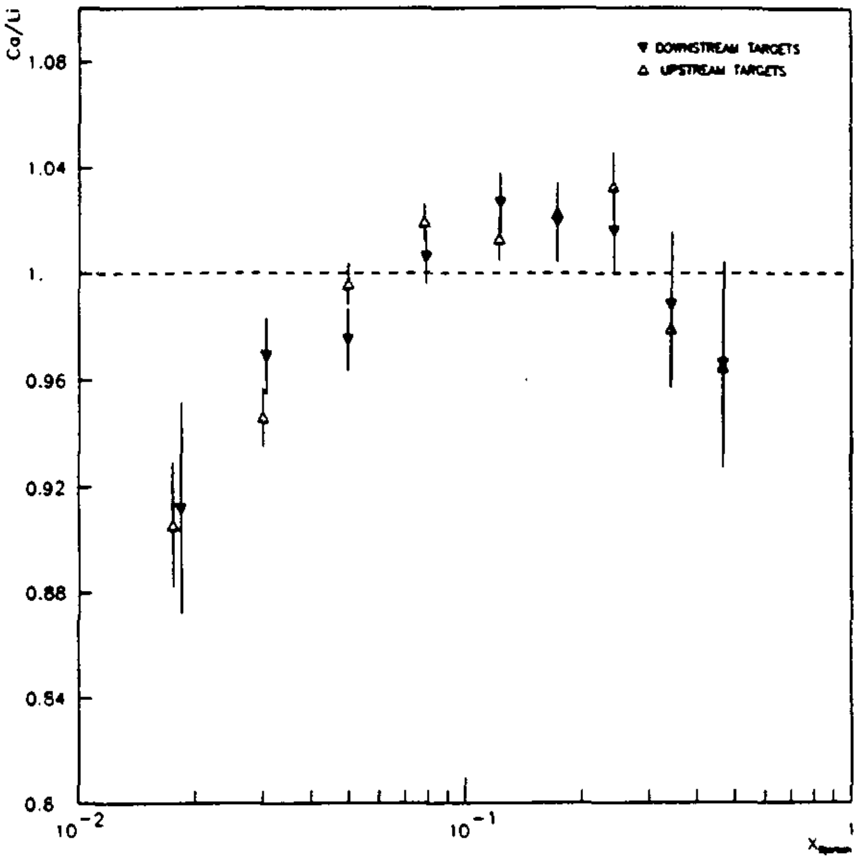

Figure 6.6: The ratio Ca/Li from the upstream and the downstream targets

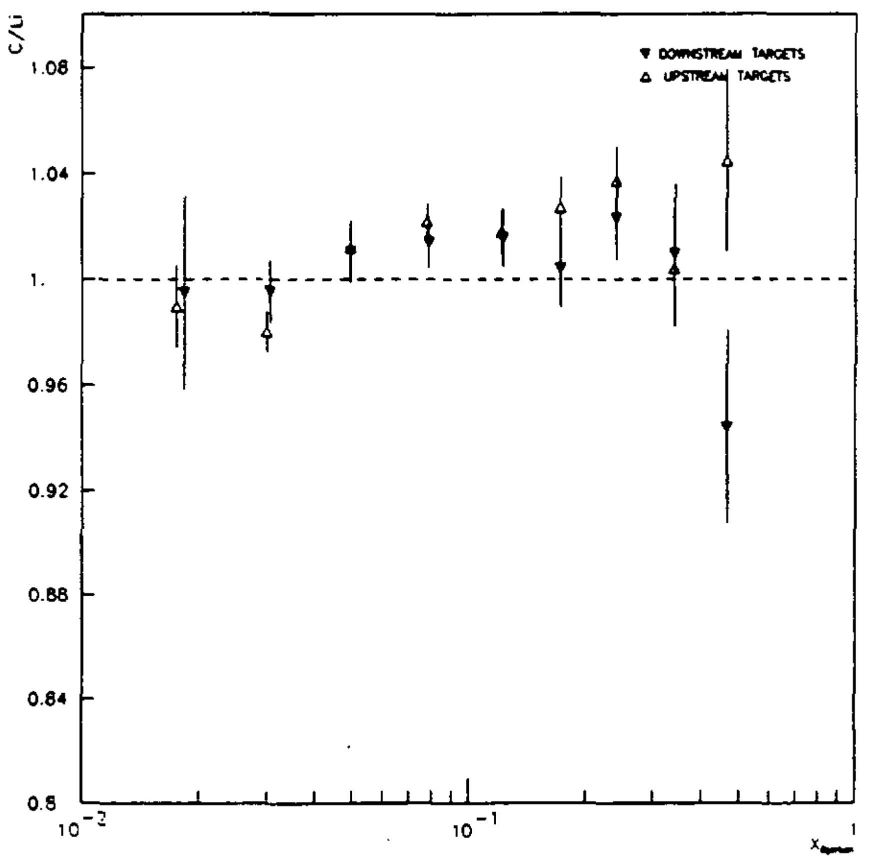

Figure 6.7: The ratio C/Li from the upstream and the downstream targets

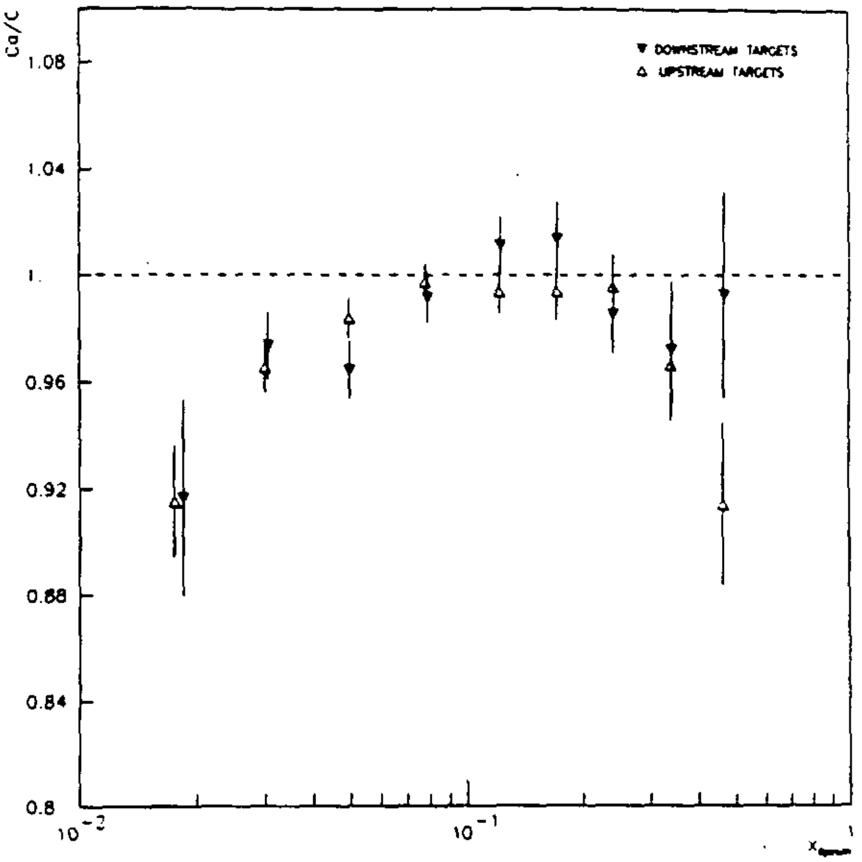

Figure 6.8: The ratio Ca/C from the upstream and the downstream targets

6.7 The Q^2 dependence of r

Our experimental Q^2 variation of r is statistically compatible with a constant $\frac{dr}{dlnQ^2}$ slope for every x bin. The slope as function of x is plotted in Figure 6.9, Figure 6.10 and Figure 6.11 for the three ratios. The radiative correction effects are negligible and the quoted errors are statistical only. Since QCD predicts an absolute value of the slope of at most 0.01, it is clear that, because of the small Q^2 range, we may see some effect only if it is largely outside the predictions. Each $\frac{dr}{dlnQ^2}$ is fitted by a straight line $a+bx$ and the values of the parameters are given in Table 6.7.

Clearly with only these low energy data nothing can be said about a Q^2 dependence of r in disagreement with QCD. However the different pictures are rather puzzling, and the 200 GeV/c data, taken with the same target setup but with a larger Q^2 range, might clarify the situation.

Table 6.7: the parameters of the fit to $dr/d\ln Q^2$

r	a	δa	b	δb
Ca/Li	0.0311	0.0152	0.0015	0.1233
C/Li	0.0327	0.0287	−0.4145	0.4492
Ca/C	0.0126	0.0171	0.1373	0.1045

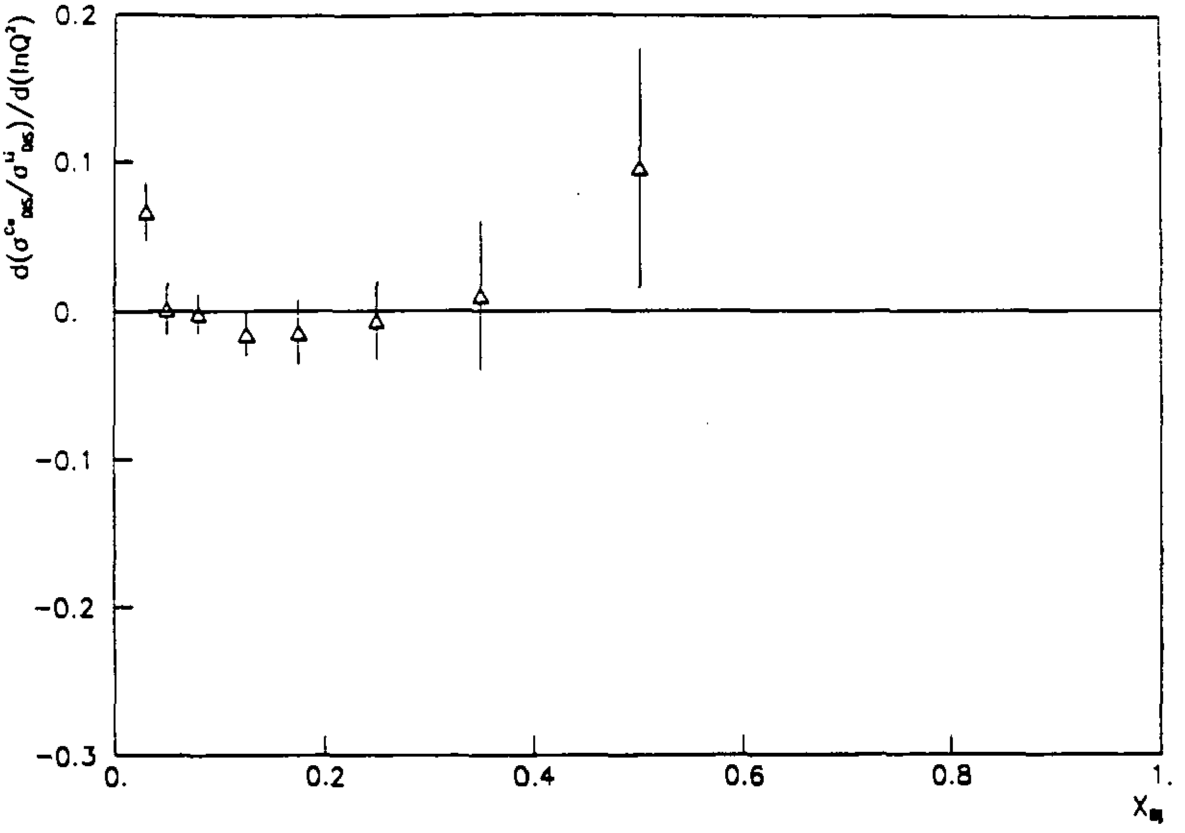

Figure 6.9: $dr/d\ln Q^2$ as function of x for Ca/Li

6.8 T_2 analysis

The events taken by T_2 have low angle and low ν and they cover almost the same small x region as T_1. As already mentioned, with a 90 GeV beam T_2 was strongly prescaled, it is nevertheless possible to use it in the first x bins, where the statistics of T_1 and T_2 are comparable. I analyse the same runs as for T_1, reject-

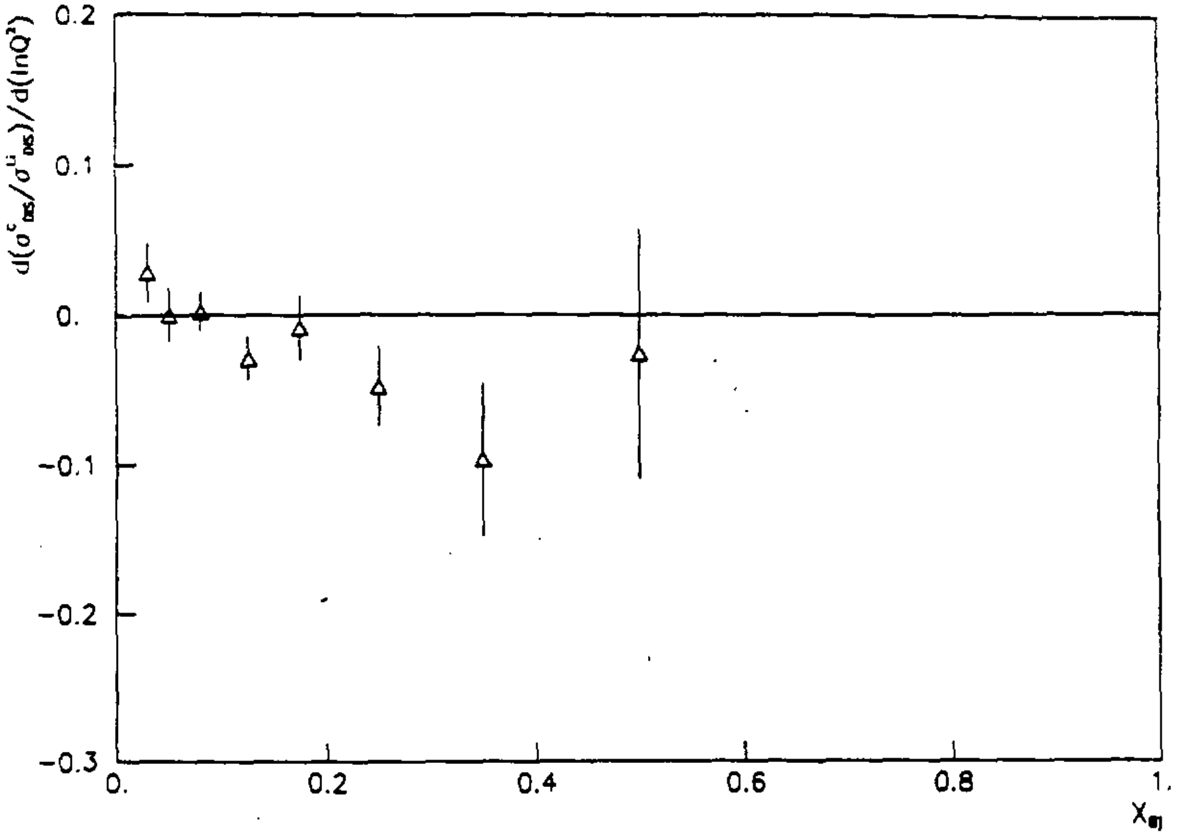

Figure 6.10: dr/dlnQ² as function of x for C/Li

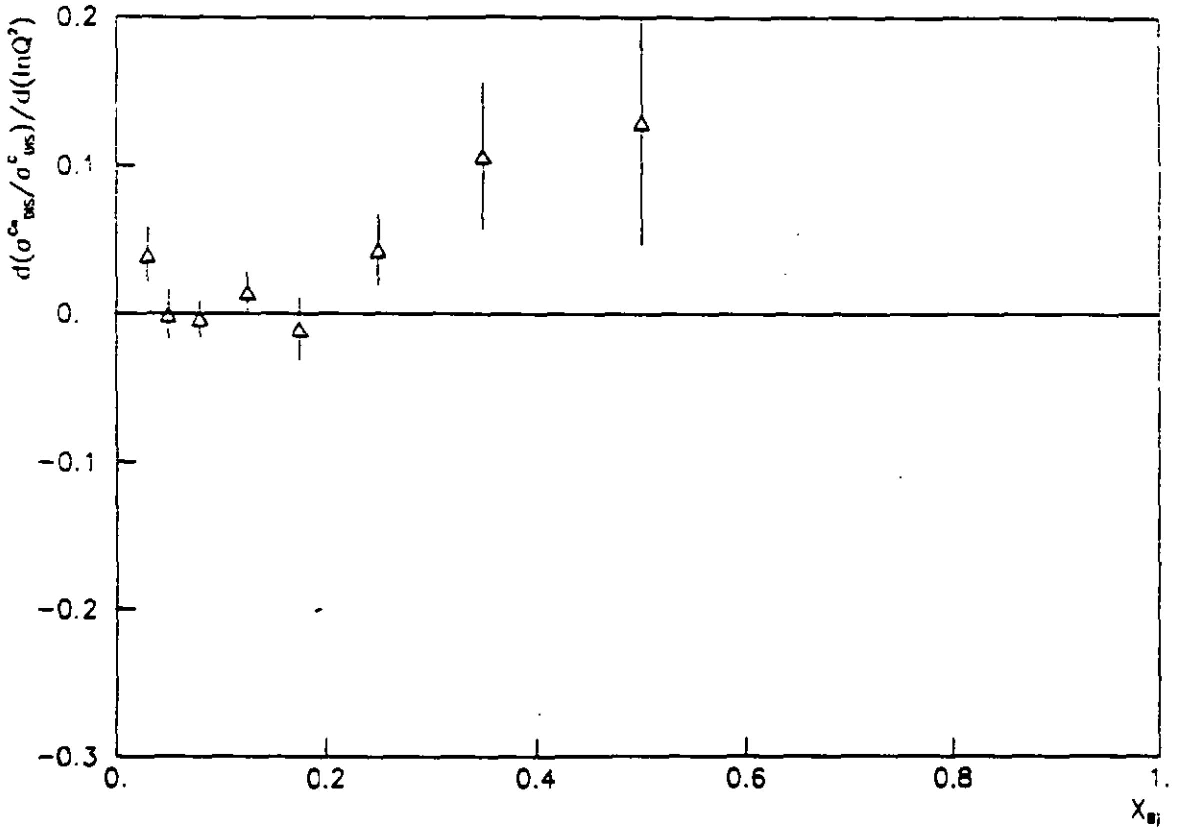

Figure 6.11: dr/dlnQ² as function of x for Ca/C

ing those events which satisfy both T_1 and T_2. Only the cut on the angle of the scattered muon is different: it is 8 mrad and 10 mrad for events coming from the upstream and the downstream part of the setup respectively; the aim is to remove the region where the acceptance is steeply changing. The number of events surviving the different cuts is given in Table 6.8 and the mean value of Q^2 and ν in each x bin is listed in Table 6.9. In the final sample 26552 events are coming from Calcium, 26025 from Carbon and 24753 from Lithium.

Table 6.8: the number of events after the cuts

Cut	**# events**
no cut	467364
θ	337466
P muon	287251
ν	79626
30% r. c.	79058
vertex	77330

Table 6.9: the mean Q^2 (GeV/c^2)^2 and ν (GeV)

x	Q^2	ν
0.0125 – 0.02	0.55	21.66
0.02 – 0.04	0.66	15.36
0.04 – 0.06	1.14	12.51

The same normalization error is affecting T_2 as T_1, whereas on the radiative corrections I put an error proportional to their size, as found in the T_1 analysis. The different ratios are given in Figure 6.12, Figure 6.13 and Figure 6.14. The mean size of the radiative corrections in each bin, plotted in Figure 6.15, shows that radiative corrections are smaller in T_2 than in T_1 because ν is lower in T_2. Also for T_2, it has been checked that the upstream and downstream ratios are consistent. In the ratios of cross sections we clearly see shadowing in Ca/Li and Ca/C and the agreement with T_1 is good. As it can be seen in Table 6.9, the mean Q^2 of the two triggers is different in each x bin: this is not affecting the result. We can therefore merge the T_1 and T_2 events with a sizable reduction of the statistical error in the first point. The obtained ratios are shown in Figure 6.16, Figure 6.17 and Figure 6.18. Each ratio has been fitted with the function $y(x) = a + bx + ce^{(dx)}$ and the values of the parameter are written in Table 6.10.

Table 6.10: the parameters of the fit to the ratios

r	a	b	c	d
Ca/Li	1.0610	−0.19690	−0.20368	−22.970
C/Li	1.0261	−0.03401	−0.08583	−31.879
Ca/C	1.0364	−0.17429	−0.13000	−19.936

6.9 The A dependence of r

The A dependence of the EMC effect has been studied in the large x region by the experiment E139 at SLAC and by the EMC in the low x region. They found that a two parameters fit of the form $\frac{\sigma_A}{\sigma_D} = cA^{\alpha}$ gives a good description of the data. The x dependence of α is plotted in Figure 6.19. In this parametrization the ratio between two elements of atomic number A and A′ is : $\frac{\sigma_A}{\sigma_{A'}}(x) = \left(\frac{A}{A'}\right)^{\alpha(x)}$.

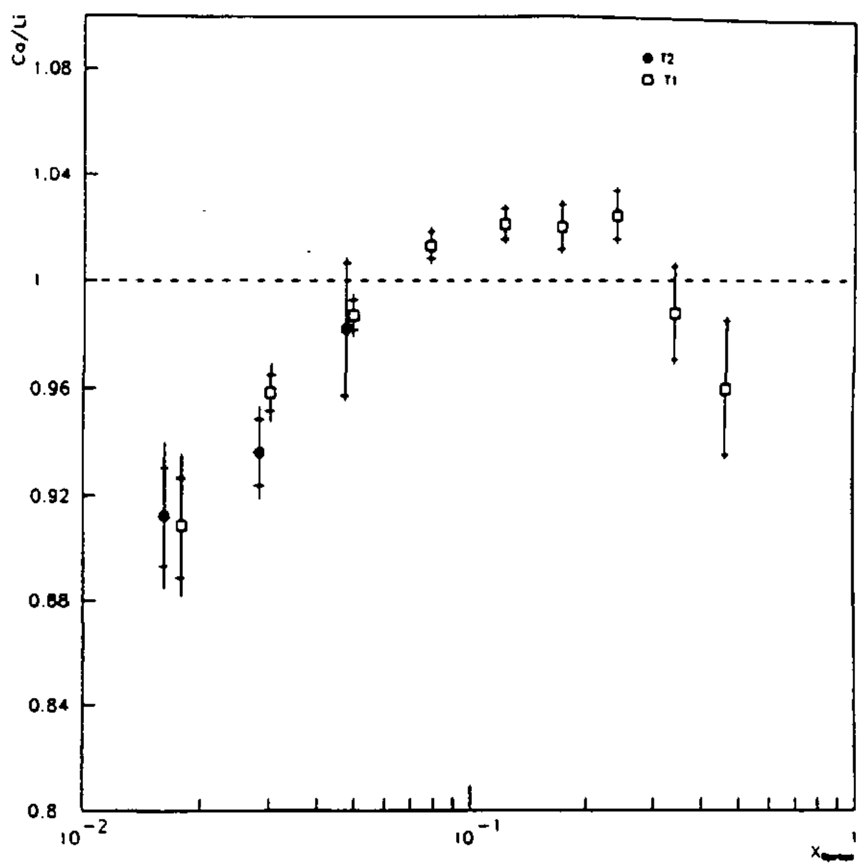

Figure 6.12: the ratio Ca/Li

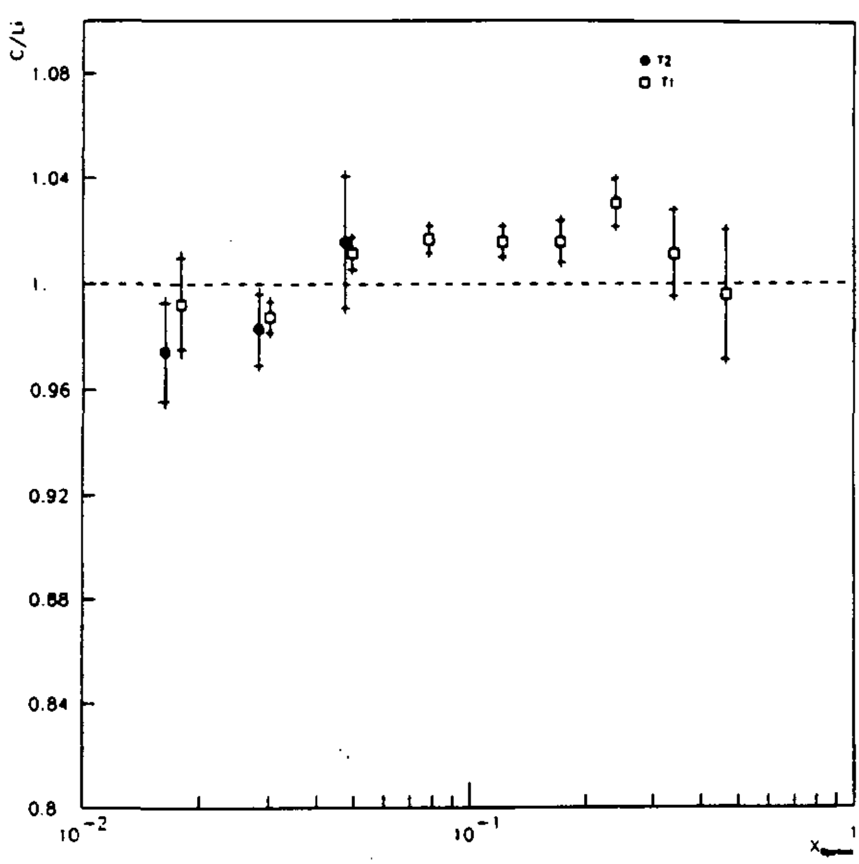

Figure 6.13: the ratio C/Li

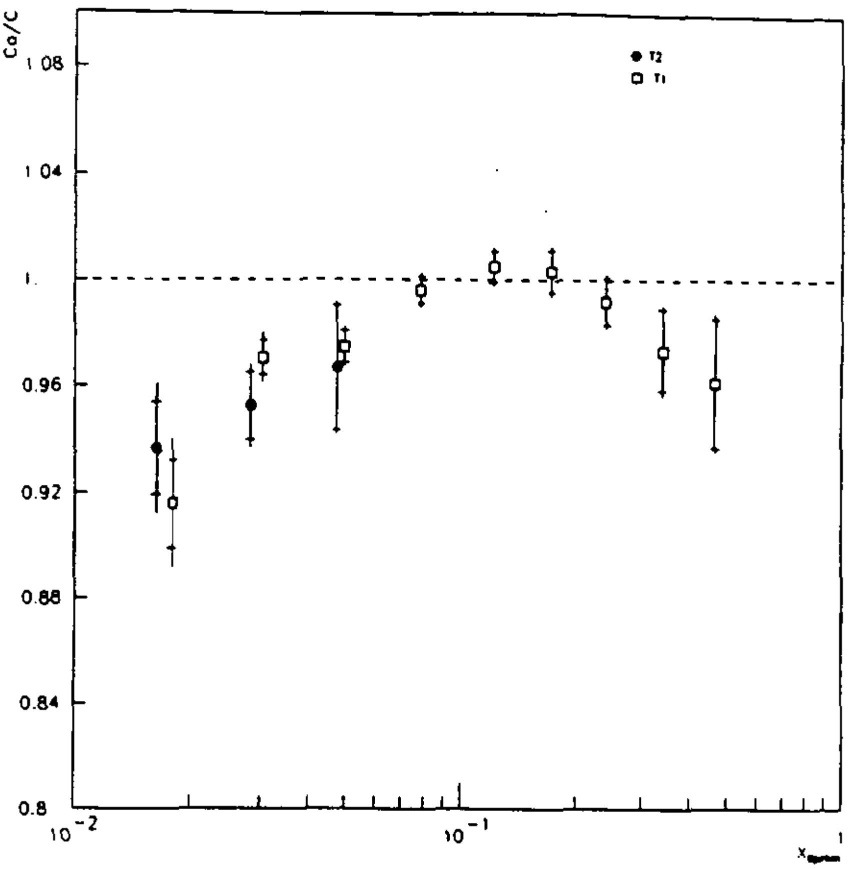

Figure 6.14: the ratio Ca/C

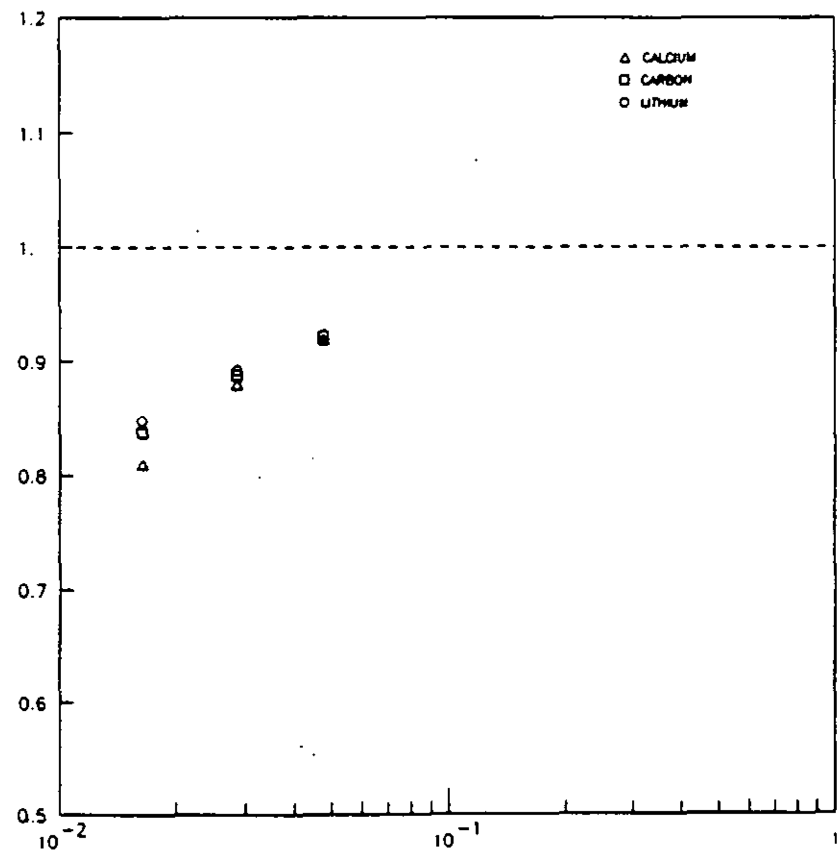

Figure 6.15: size of the radiative corrections on T_2

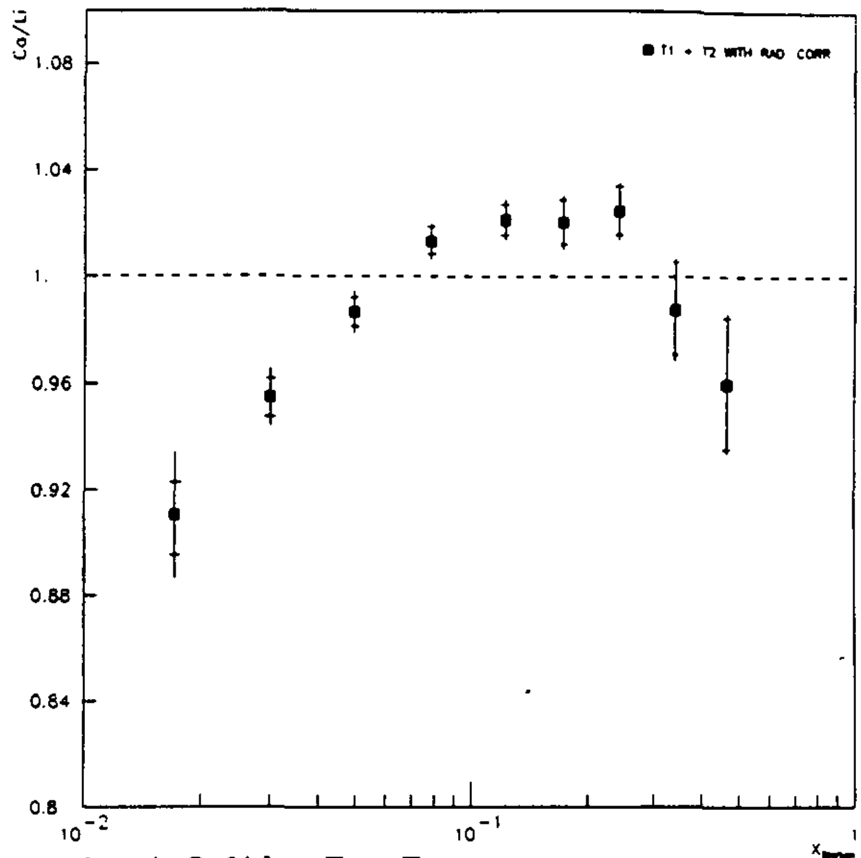

Figure 6.16: the ratio Ca/Li from T_1 + T_2

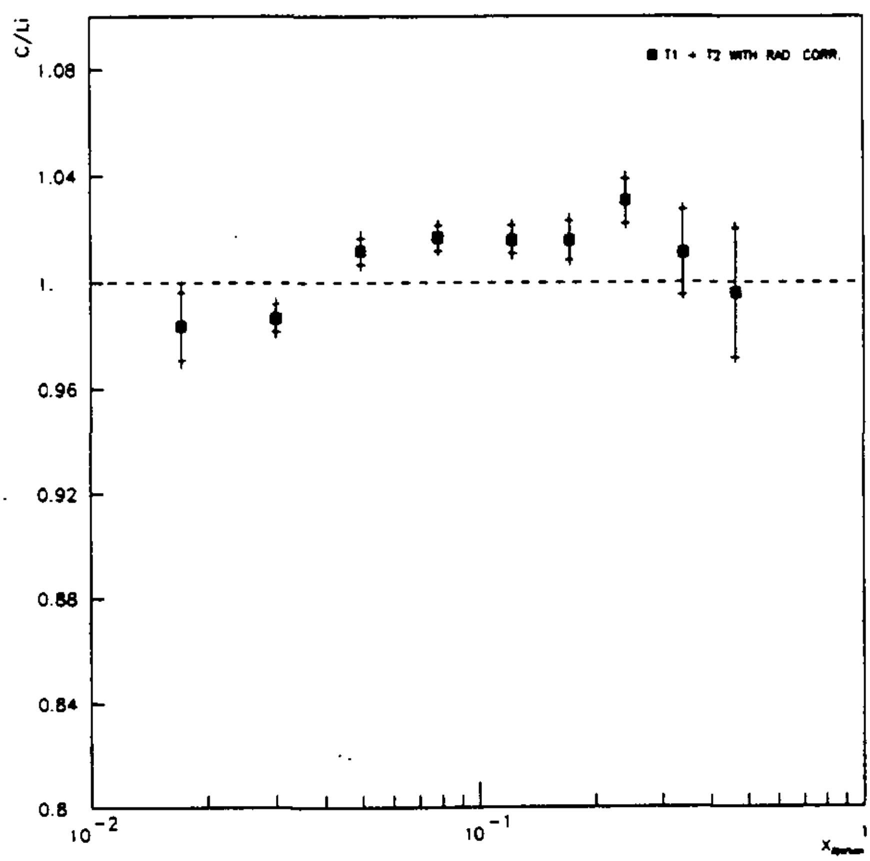

Figure 6.17: the ratio C/Li from T_1 + T_2

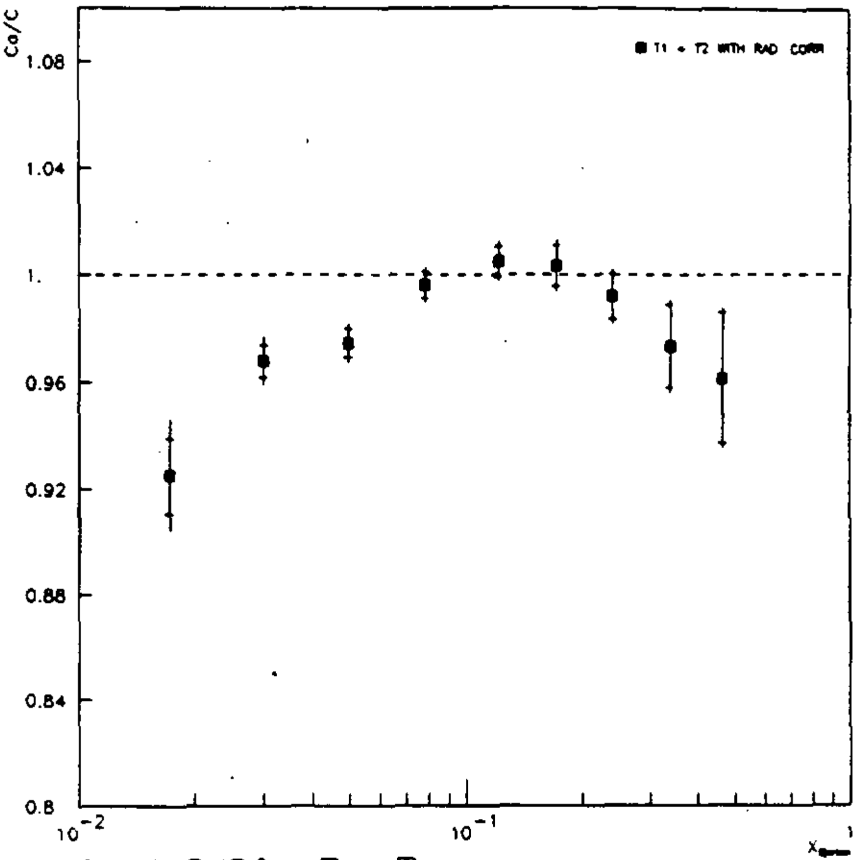

Figure 6.18: the ratio Ca/C from $T_1 + T_2$

From each measured ratio $\frac{\sigma_A}{\sigma_{A'}}(x)$ we can therefore extract the x dependence of α. This is shown in Figure 6.20 for the ratios Ca/Li and Ca/C. We see that the EMC result is confirmed with much smaller errors. We can also see the tendency of the α extracted from the ratio Ca/C to lie below the α given by Ca/Li. This might indicate that Lithium is a special nucleus and/or that the used parametrization is not suitable in the low x region; for instance it doesn't describe the increase with the mass number of the x point which separate the shadowing and antishadowing region.

6.10 The momentum sum rule

The integral $\int F_2^A(x)dx$ gives the fraction of the nucleon momentum, weighted by the squared charges, carried by quarks and antiquarks in the nucleus A. To see if this fraction depends on the mass number we calculate

$$I_B^A = \int \left(r_B^A(x) - 1 \right) F_2^B(x) dx$$

where $r_B^A(x)$ is the measured cross sections ratio, which we assume to be equal to the structure functions ratio. If I_B^A is different from zero then the quarks and antiquarks in the nucleus A carry more (or less) of the nucleon momentum than in the nucleus B. We need some assumptions to calculate I_B^A . We don't know F_2^B , however, since r_B^A is close to 1, the relative error on $r_B^A - 1$ becomes very large even if the relative error on r_B^A is small. We are thus allowed to use $F_2^{D_2}$ instead of F_2^B . We don't measure the ratio in the whole x region but, because of the shape of $F_2^{D_2}$, we can integrate from 0.02 to 0.7 losing less than 5% of its total integral. I take the $F_2^{D_2}(x,Q^2)$ given by a fit to the world data [39] and I parametrize Q^2 as a function of x, using the measured mean value of Q^2 in the different x bins. To minimize the uncertainties due to $F_2^{D_2}$ I calculate

$$H_B^A = \frac{\int_{0.02}^{0.7} \left(r_B^A(x) - 1 \right) F_2^{D_2}(x) dx}{\int_{0.02}^{0.7} F_2^{D_2}(x) dx}$$

I checked that a different $F_2^{D_2}$ doesn't change H_B^A in a significant way and the quoted systematic error is produced by a shift of r_B^A within its systematic error. The obtained values with the systematic and statistical errors are : $-0.35 \pm 1\% \pm 0.6\%$, $+1.43\% \pm 1\% \pm 0.6\%$ and $-1.98\% \pm 1\% \pm 0.6\%$ for Ca/Li, C/Li and Ca/C respectively : each of them is compatible with zero. We can therefore say that we don't see any significant difference in the nucleon momentum fraction carried by quarks and antiquarks in the nuclei of Calcium, Carbon and Lithium.

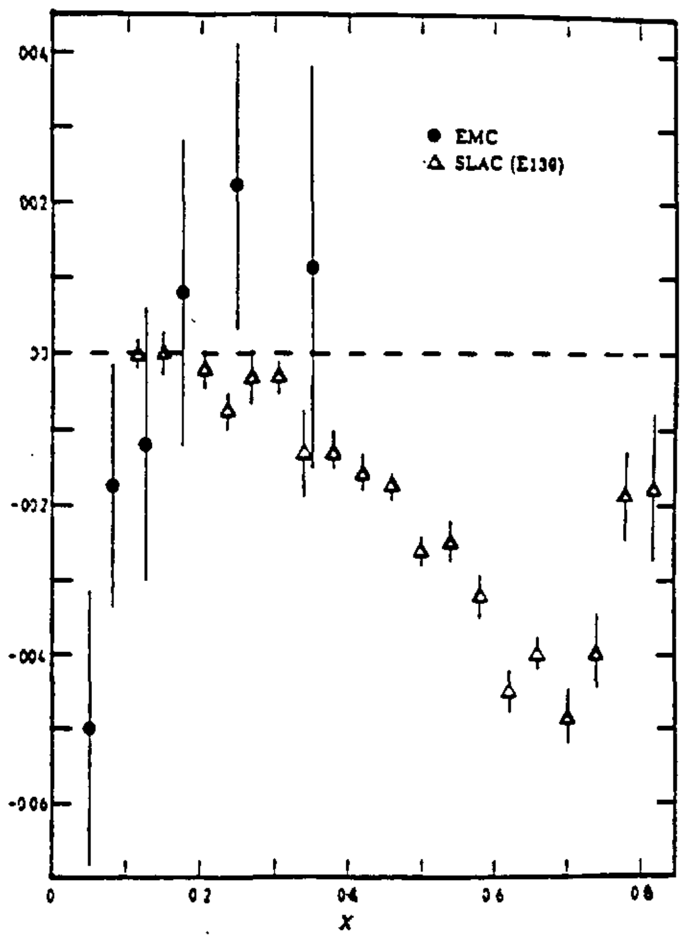

Figure 6.19: the parameter α

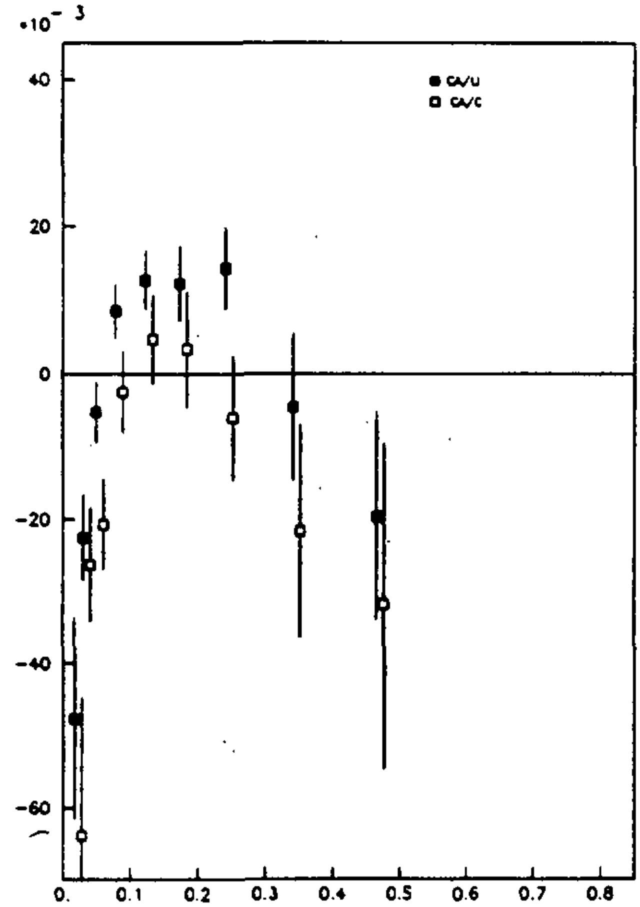

Figure 6.20: the parameter α from the data

Chapter 7

THE HADRON CUT AND THE LOW X REGION

7.1 The hadron cut

In the previous chapter it was explained how to extract the deep inelastic cross section from the collected sample of events : to each of them a weight is given which is its probability of being a true deep inelastic event. It is possible however to check this procedure rejecting the coherent and quasi elastic radiative events. This leads to a subsample made of true deep inelastic events plus the deep inelastic tail : this way we remove those events which are mostly dependent on the target material. The signature of coherent and quasi elastic events is the absence of hadrons : the recoiling nucleus or nucleon either remain inside the target or they are swept out by the magnet and not reconstructed. To be efficiently exploited, this signature needs a good discrimination between hadrons and electrons. Then we have to study the possible bias introduced by rejecting the events without hadrons.

7.2 Electron hadron discrimination

In the third chapter the calorimeter H_2 of the NMC spectrometer was described. The energy assigned to each track passing through it is : $E = aE_e + bE_h$ where E_e and E_h are the energy measured in the electron and in the hadron modules, a and b are two calibration constants determined from test beam studies. They don't depend on the particle momentum and their value is 0.17 for a and 0.68 for b. To separate electrons from hadrons we define the variable $EMAGF = \frac{E_e}{E}$ which is the fraction of energy deposited in the electron module.

For electrons, which shower completely in the electron module, it should be close to 1. Its distribution, for events with the vertex in Calcium, is given in Figure 7.1: the electron peak is clearly emerging.

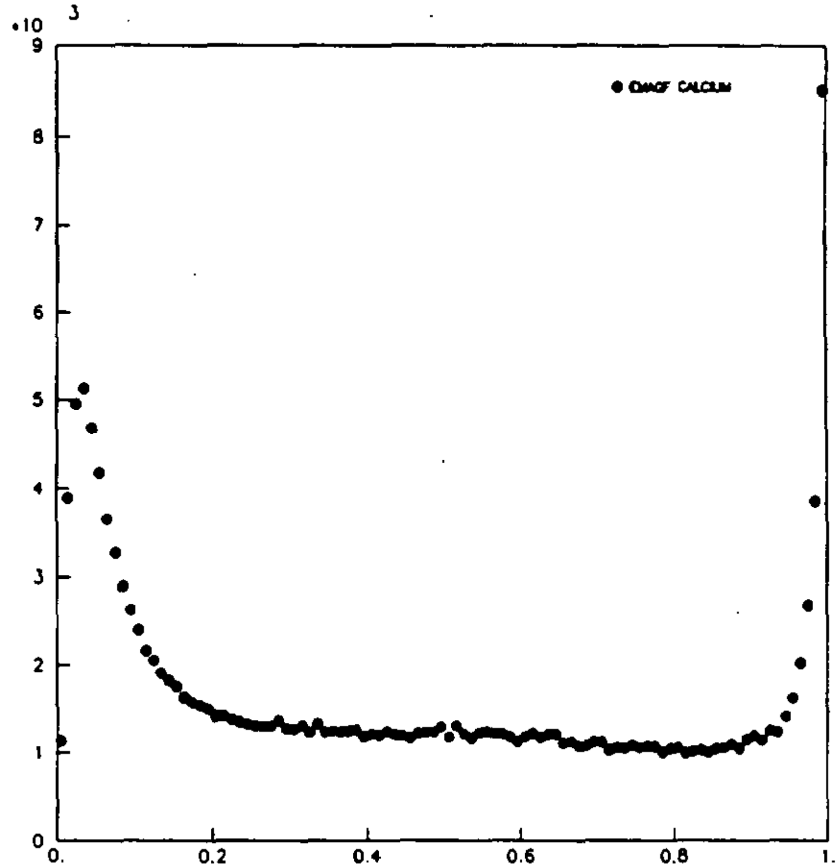

Figure 7.1: emagf distribution

On a track passing through H_2 we impose two restrictions: it must pass outside a cylinder of 30 cm radius around the hole of the calorimeter, to guarantee that its energy deposition is fully contained, and it must have a momentum greater than 5 GeV/c, to be sure of rejecting the quasi elastic events. We then define as an electron a track with EMAGF > 0.80 and as a hadron a track with EMAGF < 0.80. The reliability of this selection was studied in [44]. A clean sample of electron was extracted from the data. The idea is to select the e^+e^- pairs produced by a bremsstrahlung γ; they are selected as pairs of tracks of opposite sign, with a low invariant mass and a high fractional energy ζ, defined as the ratio of the total energy of the pair over the transferred energy ν. For bremsstrahlung pairs it should be close to 1. The EMAGF discrimination criterion was thus found to be 100%. We are therefore sure of rejecting all the events with electrons only, that is the elastic and quasi elastic tail. We also remove part of the events with hadrons, as it can be seen from Figure 7.1. However, this fraction doesn't depend on the target material and it is not affecting the cross sections ratio.

7.3 Possible bias

A bias might be introduced by the hadron cut if the hadron production and propagation depend on the material in which the interaction takes place and if a different fraction of events belonging to the deep inelastic tail is removed for different targets. It is clear that a good selection criterion should not privilege any particular target material.

A parameter, z, is introduced to study the hadron production: it is the ratio of the energy of the hadron over the energy of the struck quark. The distribution of the hadrons as a function of z is the fragmentation function. For our purpose the important variable is the formation length, i.e., the distance between the interaction point of the virtual photon and the place where the "dressing" of the quark starts with the creation of hadrons. If the formation length, which is proportional to ν, is greater than the nuclear radius, hadronization takes place outside the nucleus and production doesn't depend on the particular kind of nucleus. This has been shown to be the case in the high ν region by the EMC and this is also what we see in our data, which have a mean ν of 52 GeV. As a matter of fact the ratio between the fragmentation functions of the different materials are compatible with 1 within about 3%. A material dependence would show up in an enhancement of the fragmentation function at low z in high A materials, in which, because of a larger radius, hadrons might interact in the nuclear medium.

Once produced the hadron propagates through the targets, which have different interaction length. However, in our setup, the targets are segmented and spaced. The hadron doesn't pass only through the target in which it is produced but also through a few of the others which are behind it, averaging out the interaction length. In order to render the loss of one hadron less severe, I select high multiplicities, rejecting those events with an invariant hadronic mass $W < 8$ GeV/c^2 (the hadron multiplicity is proportional to logW): this also removes low ν events.

Our selection criterion also rejects events from the deep inelastic tail, in a way which shouldn't depend on the target material. The z of these events is on the average lower than the z of true deep inelastic events, because their measured ν is larger than the true one. A target dependent rejection would produce different fragmentation functions for the different materials, and we have seen that this is not the case.

Coherent interactions on the proton with the production of a vector meson, mainly a ρ^0 , may survive the hadron cut. A clear peak at the ρ^0 mass is seen in the invariant mass spectra of oppositely charged pairs of pions with total energy larger than 0.92ν [Figure 7.2].

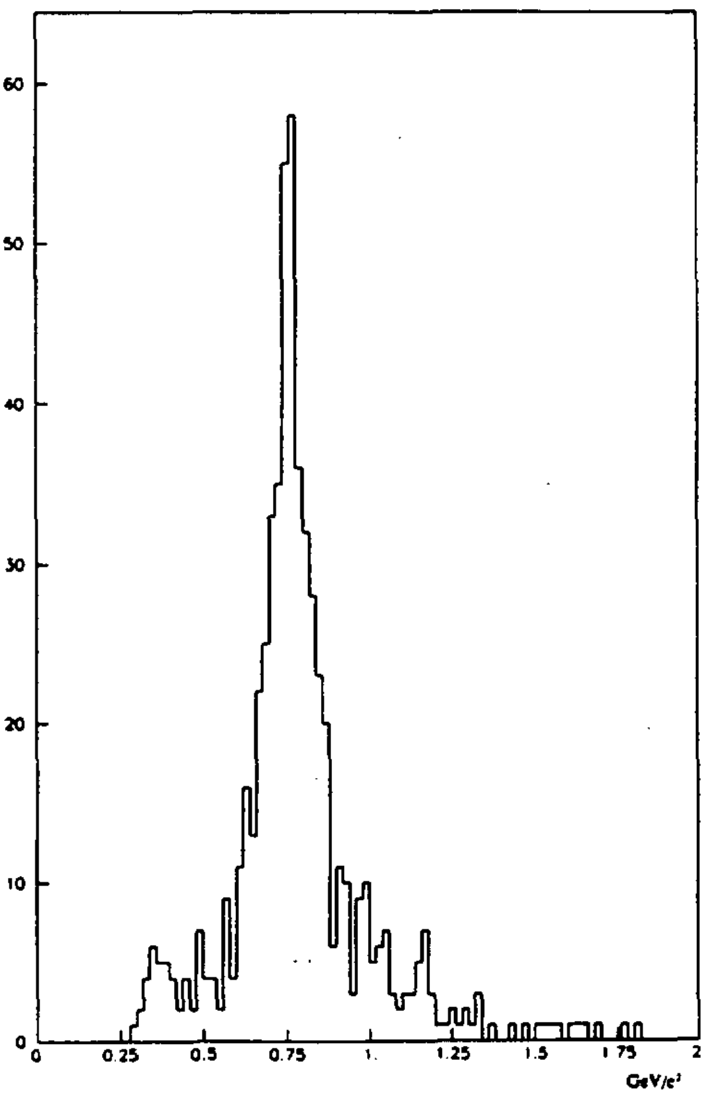

Figure 7.2: the invariant mass distribution of the pions pairs from Lithium.

The ρ^0 entering the histogram are produced both in deep inelastic and coherent interactions. If we use the results of [45] and [46] we conclude that the coherent events are at most a few per cent of the events selected with the hadron cut : since they do not depend on the target material their effect on the cross sections ratio is negligible.

The best way to check our assumptions is to look at the hadron multiplicity as a function of x for different targets. Any difference among the distributions would indicate an effect due to target dependence. In Figure 7.3 we see that the agreement among the distributions is good and there is no evidence of an effect larger than ~ 1.5%.

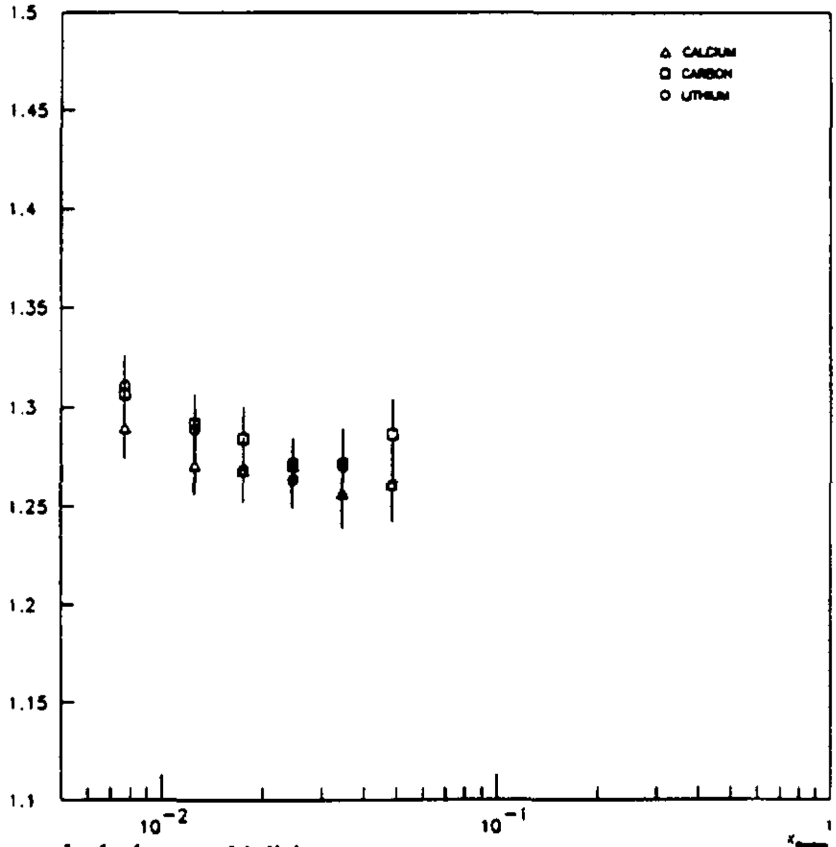

Figure 7.3: the hadron multiplicity

The bins which cover the x region between 0.005 and 0.06, and which are the most affected by radiative corrections, are what we can study. At higher x the statistic is very poor and the target dependence may become stronger because the high x region corresponds to both a shorter formation length and a shorter interaction length which prevents the averaging over the downstream targets.

To summarize there is no evidence, within the quoted uncertainties, that the sample selected with the hadron cut is biased, therefore the method can be used in the low x region to check the results obtained with the standard method of radiative corrections.

7.4 Events selection and results

I select T_1 events with a vertex type 3, i.e., with the beam muon, with the scattered muon and with at least one charged track reconstructed from the interaction vertex. To the scattered muon I apply the same cuts as in the T_1 analysis. Furthermore I also require that the invariant hadronic mass W is larger than 8 GeV/c^2 and that there is at least one hadron passing through the active part of the calorimeter with momentum larger than 5 GeV/c. The number of events after the cuts and the mean Q^2 and ν in the different x bins are given in Table 7.1 and Table 7.2.

Table 7.1: the number of events after the cuts

Cut	# events
T_1 + vertex type 3	742820
scattered muon ok	351181
at least 1 track in active H_2	325483
at least 1 hadron > 5 GeV/c	237469

The selected sample is made of deep inelastic events plus events from the deep inelastic tail. However the hadron cut might select true deep inelastic and deep inelastic tail events with different efficiencies. For example our selection may remove a larger fraction of deep inelastic tail than deep inelastic events if the photon accompanying the hadron in the radiative process harms the identification

Table 7.2: the mean Q^2 (GeV/c^2)^2 and ν (GeV)

x	Q^2	ν
0.005 – 0.010	0.69	59.19
0.010 – 0.015	1.36	53.69
0.015 – 0.020	1.66	50.67
0.020 – 0.030	2.23	48.81
0.030 – 0.040	3.10	47.80
0.040 – 0.060	4.38	47.98

of the hadron. If we apply the radiative corrections, whose effect on the cross section ratios is in any case small (at most 1.6% in the first bin), we may overcorrect, i.e., we correct for events which have been already removed from the sample. This is accounted for by plotting a value of the ratio which is in the middle between the corrected and the uncorrected one, and putting an error on it equal to half the correction. I estimate the error due to a possible small target dependence to be around 1.5% on the first five points and 2% on the last. The normalization error due to the target thickness is the same as on T_1. The effect due to the uncertainties on the $F_2^{D_2}$ used to calculate the radiative corrections and due to a measurement of ν wrong by $\pm$ 1% were checked to be negligible. The differences between the ratios from the upstream and the downstream targets are within the error. The final results are shown in Figure 7.4, Figure 7.5 and Figure 7.6; in the overlapping region they agree with the ones given by the standard procedure of the radiative corrections. We clearly see shadowing in Ca/Li and Ca/C, a little evidence of shadowing in C/Li and, within our errors, in the low x region we do not have any significant change of the slope of the ratios, which might have indicated the saturation of shadowing.

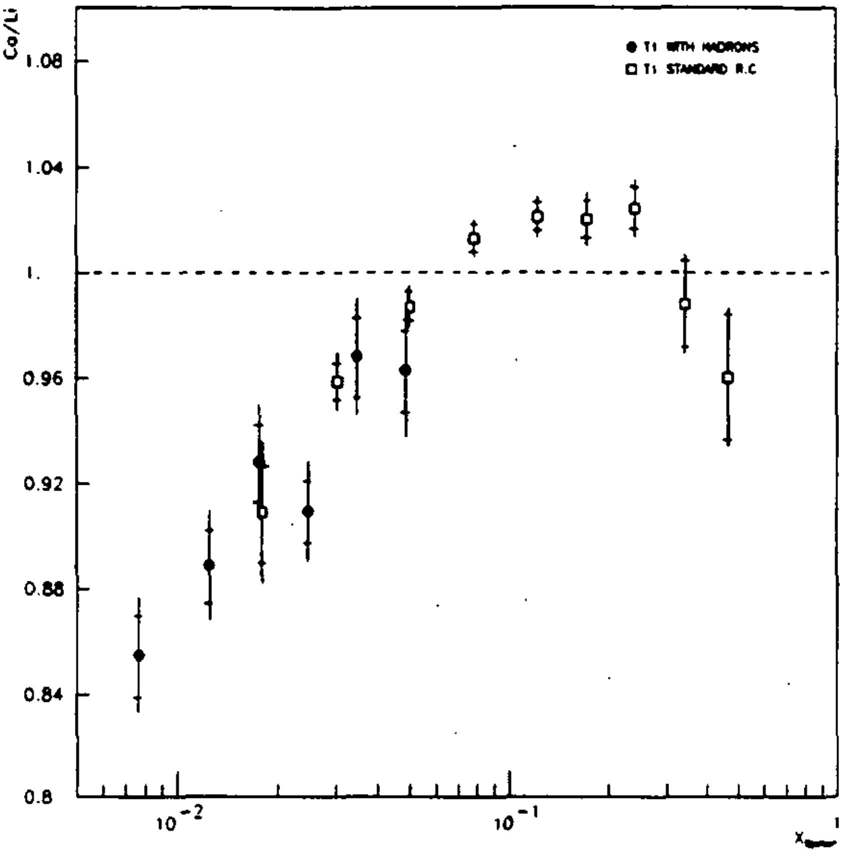

Figure 7.3: the ratio Ca/Li, the errors shown are the total errors, obtained by adding the statistical and systematic errors in quadrature. The extent of the statistical errors is shown by the inner bars.

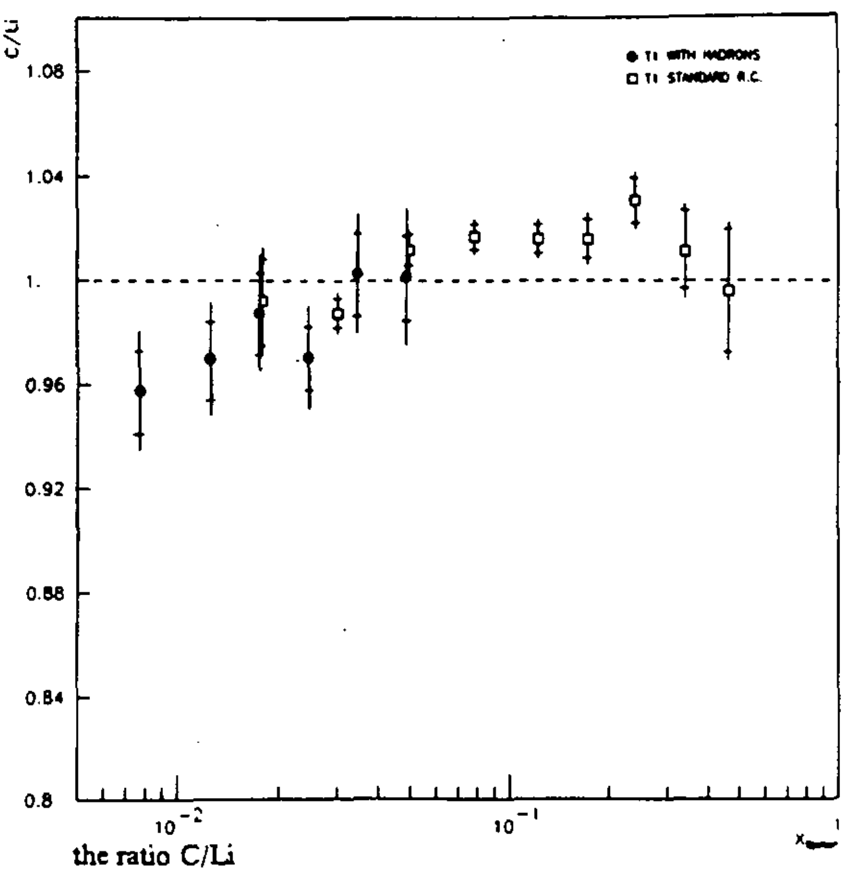

Figure 7.4: the ratio C/Li

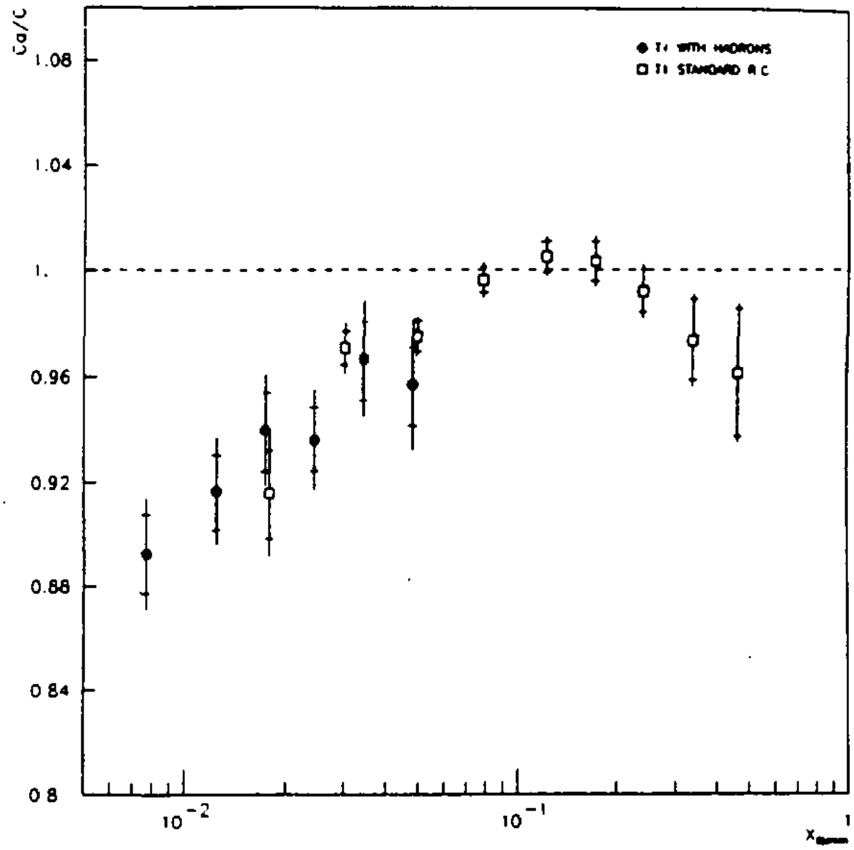

Figure 7.5: the ratio Ca/C

CONCLUSIONS

The data taken with a 90 GeV muon beam are analyzed. A special target set-up was used in order to minimize the systematic error. The assumption made to extract the cross sections ratio are checked and found to be reasonable. A particular care is given to the low x region, investigated with two different triggers. An alternative method to remove the contribution of radiative events leads to results which are in agreement with the ones given by the standard procedure. I will now underline the main features of the cross sections ratios.

- Shadowing region: the comparison between Ca/Li and C/Li shows that shadowing is strongly A dependent. The increase with the mass number of the intersection point at low x, which was hinted at in the EMC data [20], is clearly seen in C/Li and Ca/Li.
- Antishadowing region: we have antishadowing in Ca/Li and C/Li, whereas there is only a little indication of it in Ca/C. In Figure 1 the SLAC result on Ca/C [47] and ours are compared: there is agreement, however the size of the errors is too different to draw any definitive conclusion. It might be interesting to see what antishadowing looks like in Fe/N ([48] and [42]) and in Cu/C [20] [Figure 2]. Unfortunately large errors forbid any conclusion about a possible saturation of antishadowing with increasing mass number.
- Large x region: we see the shape of the EMC effect in Ca/Li and C/Li.
- Q^2 dependence of the cross sections ratio: we exclude a very large effect in disagreement with perturbative QCD, however the claimed discrepancy [49] is outside our resolution.
- A dependence: we confirm and we improve the EMC result on the x dependence of the parameter α in the low x region, with the indication that the standard parametrization $\frac{\sigma^A}{\sigma^{D_2}}(x)=cA^{\alpha(x)}$ might not be suitable in this region.
- Momentum sum rule: we don't see any significant difference in the sharing of the nucleon momentum between quarks and gluons in the nuclei of Calcium,

Carbon and Lithium. Other experiments don't have any conclusive result on a possible decrease of the nucleon momentum fraction carried by quarks in heavy nuclei compared to deuterium, and analysis made with nuclei different from Deuterium are in agreement with our conclusions [48].

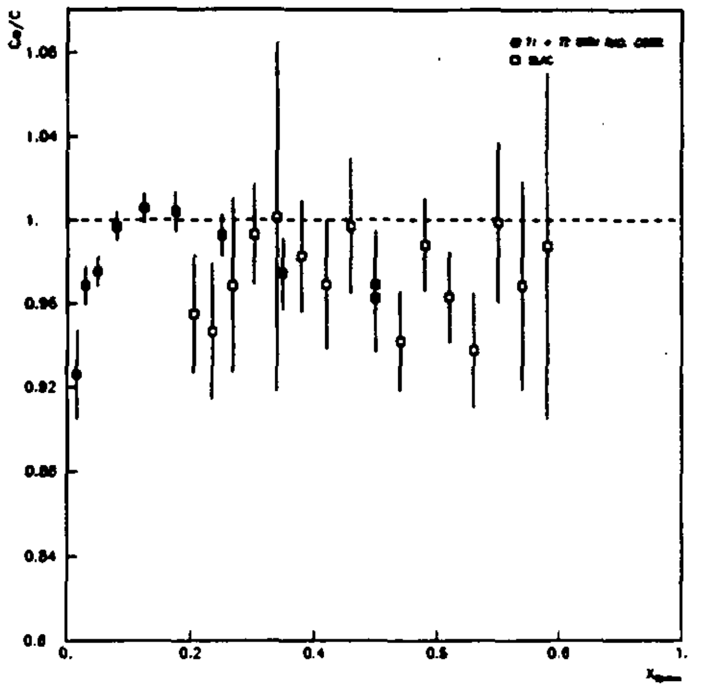

Figure 1: the ratio Ca/C

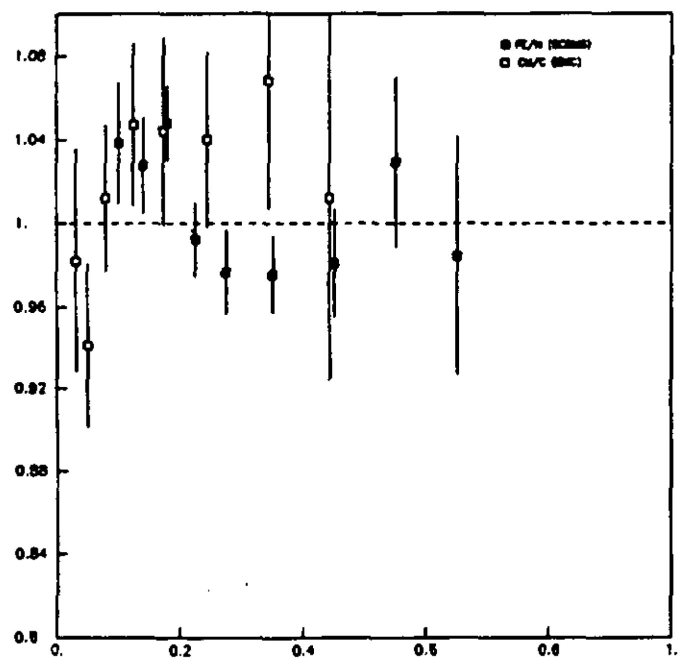

Figure 2: the ratios Fe/N and Cu/C

APPENDIX

List of people participating in 1986

THE NEW MUON COLLABORATION (NMC)

Bielefeld University[1], Freiburg University[2], Max-Planck Institute Heidelberg[3], Heidelberg University[4], Indiana University[5], University of Mainz[6], Mons University[7], Neuchâtel University[8], NIKHEF- K[9], Oxford University[10], University of California Santa Cruz[11], SIN/PSI[12], Torino University and INFN Torino[13], Uppsala University[14], Institute for Nuclear Studies Warsaw[15], Warsaw University[16], Wuppertal University[17]

D. Allasia[13], P. Amaudruz[12], M. Arneodo[13], A. Arvidson[14], B. Badelek[16], G. Baum[1], J. Beaufays[9], I.G. Bird[3], M. Botje[12], W. Burger[12], C. Broggini[8], W. Brückner[3], A. Brüll[2], J. Ciborowski[9], R. Crittenden[5], R.v.Dantzig[9], H. Döbbeling[3], J. Domingo[12], J. Drinkard[11], A. Dzierba[5], H. Engelien[2], M.I. Ferrero[13], L. Fluri[8], P. Grafstrom[14a)], D. Greiner[2], P. Gretillat[8], W. Gunther[2], E. Hagberg[14], D.v.Harrach[3], M.v.d.Heijden[9], C. Heusch[11], Q. Ingram[12], K. Janson[14], M.d.Jong[9], E.M. Kabuss[3], R. Kaiser[2], T. Ketel[9], F. Klein[6], B. Korzen[17], U. Krüner[17], S. Kullander[14], U. Landgraf[2], F. Lettenström[14], T. Lindqvist[14], G. Mallot[6], G.v.Middelkoop[9], Y. Mizuno[3], J. Nassalski[15], D. Nowotny[3], N. Pavel[17], H. Peschel[17], C. Peroni[13], U. Pietrzyk[17b)], B. Povh[3,4], R. Rieger[6], K. Rith[3], K. Röhrich[3], E. Rondio[16], L. Ropelewski[16], A. Sandacz[15], R. Schumacher[12c)], E. Schwarz[8], U. Sennhauser[12], F. Sever[1], T.A. Shibata[6], M. Siebler[1], A. Simon[3], A. Staiano[13], G. Taylor[10d)], M. Treichel[3e)], J.L. Vuilleumier[8], T. Walcher[6], W. Wallucks[2], K. Welch[5], R. Windmolders[7]

Bibliography

1. E. Leader and P. Predazzi, An introduction to Gauge Theories and the 'New Physics', Cambrige University Press (1985).
2. G. Altarelli and G. Parisi, Nucl. Phys., **B126** (1977) 298.
3. D. Allasia et al., CERN SPSC/85 – 18 (1985).
4. A. Bodek et al., Phys. Rev., **D20** (1979) 1471.
5. J.J. Aubert et al., Nucl. Phys., **B259** (1985) 189.
6. R. Voss, Proc. Int. Symp. on Lepton and Photon Interactions at High Energies, Hamburg, ed. W. Bartel and R. Ruckl (1987).
7. R. P. Mount, International Conference on High Energy Physics, Munich (1988).
8. J.J. Aubert et al., Nucl. Phys., **B293** (1987) 740.
9. A. Bodek et al., Phys. Rev., **D20** (1979) 1471.
10. A.C. Benvenuti et al., to be published.
11. S. Ekelin and S. Frederiksson, Phys. Lett., **B162** (1985) 373.
12. A.D. Martin et al., Phys. Lett., **B207** (1988) 205.
13. J.J. Aubert et al., Phys. Lett., **123B** (1983) 275.
14. R.L. Jaffe, Lectures presented at the 1985 Los Alamos School on Quark Nuclear Physics (1985).
15. R.G. Arnold et al., Phys. Rev. Lett., **52** (1984) 722.
16. S.J. Brodsky et al., Phys. Rev., **D6** (1972) 177.
17. M. Arneodo et al., CERN. EP/88 – 56.
18. N.N Nicolaev and V.I. Zakharow, Phys. Lett., **55B** (1975) 397.
19. E.L. Berger and J. Qiu, Phys. Lett., **206B** (1988) 141.
20. J. Ashman et al., Phys. Lett., **202B** (1988) 603.
21. S.V. Akulinichev al., Phys. Lett., **158B** (1985) 485.
22. C.H. Llewellyn Smith, Phys. Lett., **128B** (1983) 107.
23. H.J. Pirner and J.P. Vary, Phys. Rev. Lett., **46** (1981) 599.

24. F.E. Close et al., Phys. Lett., **168B** (1986) 400.
25. O. Nachtmann and H.J. Pirner, Z. Phys., **C21** (1983) 277.
26. T. Sloan et al., Phys. Reports, **162** (1988) 47.
27. R. Clifft Doble, CERN SPSC/74 – 12 (1974).
28. J.J. O.C.Allkofer et al., NIM **179** (1981) 445.
29. W. Flauger, CERN EP/79 – 25 (1979).
30. Q. Ingram, NMC 10/86 (1986).
31. R.P. Mount, NIM **187** (1981) 401.
32. P.J. Pointing, CERN EP/80 – 01 (1980).
33. L.W Mo and Tsai, Rev. Mod.Phys., **41** (1969) 205.
34. J.J. Aubert et al., Z. Phys. **C22** (1984) 341.
35. T. Sloan, NEC 4/87 (1987).
36. B.B.P. Sinha et al., Phys. Rev., **C7** (1973) 1930.
37. J. Baley et al., Nucl. Phys. **B151** (1979) 367.
38. G.C. Li et al., Nucl. Phys. **A162** (1971) 583.
39. Y. Mizuno, NMC analysis meeting 8/11/1988.
40. L. Fluri, private communication.
41. I. Sick, Nucl. Phys. **A218** (1974) 509.
42. G. Bari et al., Phys. Lett., **B163** (1985) 282.
43. J. Dasu et al., Phys. Rev. Lett., **61** (1988) 1061.
44. E. Rondio, NMC main meeting 30/5/1988.
45. J.J. Aubert et al., Phys. Lett.,**B161** (1985) 203.
46. J. Ashman et al., Z. Phys. **C39** (1988) 169.
47. R. Arnold et al., Slac pub. 3257 (1983).
48. A.C. Benvenuti et al., Phys. Lett., **B189** (1987) 483.
49. L. Ropelewski, The 19th Symposium on Multiparticle Production, Arles (1988)
50. H. Cheung, Ph.D. Thesis, Oxford University (1987)